CENTIMETER-DEEP TISSUE FLUORESCENCE MICROSCOPIC IMAGING

by

BINGBING CHENG

Presented to the Faculty of the Graduate School of

The University of Texas at Arlington in Partial Fulfillment

of the Requirements

for the Degree of

DOCTOR OF PHILOSOPHY

THE UNIVERSITY OF TEXAS AT ARLINGTON

August 2016

Acknowledgements

I owe a great deal of thanks to my supervisor, Dr. Baohong Yuan, for his mentorship, encouragement, and support. His energy and enthusiasm inspired me to keep moving forward, and I thank him for letting me take the time to develop a broad range of experience. I'm fortunate to work with him in the creation of a new imaging field. Thank you for letting me take part in the ultrasound-switchable fluorescence imaging study; seeing the potential of this technology to open the door for future studies of centimeter-deep tissue fluorescence microscopic imaging makes all of the work worthwhile. Thank you for helping me become a better researcher and person.

My heartfelt thanks go to Dr. Hanli Liu, Dr. Kytai Truong Nguyen, Dr. Georgios Alexandrakis, and Dr. Yi Hong, not only for their insightful criticisms and suggestions as my dissertation committee member, but also for their continuous guidance throughout my doctoral career. Individually, I would like to give my deepest respect to Dr. Liu, for teaching me knowledge of medical imaging and guiding me to pass the milestone examinations during the graduate studies; to Dr. Nguyen, for sharing essential lab equipment and chemicals towards the successful completion of USF contrast agent development; to Dr. Alexandrakis, from whom I have learned a lot about microscopy and optics; and to Dr. Hong, for his collaboration in biochemical experiment designs and encouragement by sharing his doctoral experience.

I am grateful to my colleagues and good friends, Dr. Mingyuan Wei and Dr. Yanbo Pei. Dr. Wei is the first person I met when I came to US and the person who helped me a lot in both living life and scientific research in the first year. I started my biochemical studies with him and learned many skills and knowledge from him. Dr. Pei, as an expert in optics, gave me enormous help in developing imaging systems. In addition, it is happy to work with him. After intense experiments in the middle of the night, walking towards home together and discussing about science, economy, history, and philosophy is quite a release to me. Those time is enjoyable and unforgettable. I am also thankful to our collaborators Dr. Francis D'Souza and Mr. Venugopal Bandi in the University of North Texas for providing environment-sensitive fluorophores.

I also would like to thank my colleagues and friends, Dr. Yuan Liu, Mr. Jayanth Kandukuri, Ms. Bahar Saremi, Dr. Hua Cao, Mr. Harish Pitta, Ms. Aneetta Kuriakose, Dr. Hong Weng, Dr. Jun Zhou, Ms. Yihui Huang, Dr. Nan Zhang, Dr. Shuling Wang, Ms. Jianwei Cao, Mr. Jinglei Wu, Mr. Shuai Yu, Mr. Tingfeng Yao, and Mr. Zhen Wang, for their professional contributions, discussions, companions, and support during the past four years.

I wouldn't be here without my family, and I am sincerely thankful to my beloved parents, Mrs. Lihua Sun and Mr. Xiuyan Cheng. Mom and Dad, thank you for your generous support in my education and for all the things you gave up in order to make me feel free to chase my dream. Your love is the source of endless strength for me.

Lastly, Chenchen, who spent her best time with me throughout the college and my PhD has suffered more than anyone. Thank you for tolerating me always working late till midnight. Everytime when I lost hope and wanted to give up, you are person who always encourage me and have faith in me. You helped me a lot in everything, especially in *in vivo* studies of my final stage of PhD. That was the toughest time in my PhD since I have no experience working with animals. But you made me go through that successfully. I will always be grateful for the sacrifices you've made to help me reach my goals. You were my closest classmate, friend, and I feel so lucky to have you finally be my wife right before the end of my student career. I look forward to the next stage of our life.

June 24th, 2016

Abstract

CENTIMETER-DEEP TISSUE FLUORESCENCE MICROSCOPIC IMAGING

Bingbing Cheng, PhD

The University of Texas at Arlington, 2016

Supervising Professor: Baohong Yuan

Fluorescence microscopic imaging in centimeter-deep tissue has been highly sought-after for many years because much interesting *in vivo* micro-information—such as microcirculation, tumor angiogenesis, and cancer metastasis—may deeply locate in tissue. However, it is very challenging because of strong tissue light scattering. This includes: how to confine the fluorescence emission into a small volume to achieve high spatial resolution; how to increase fluorescence emission efficiency to compensate the signal attenuation caused by small emission volume and tissue scattering/absorption; and how to reduce background fluorescence noise and exclusively differentiate signal photons from background photons to increase signal-to-noise ratio (SNR) and sensitivity.

Ultrasonic scattering is two to three orders of magnitude less than light scattering in opaque biological tissue. Therefore, light focusing has been replaced by ultrasonic focusing to achieve high spatial resolution in deep tissue. In addition, high intensity focused ultrasound (HIFU) can noninvasively heat a small region deep within the body (hundreds of microns in lateral). If one can develop a contrast agent whose fluorescence emission is sensitive to this HIFU-induced temperature change and a sensitive imaging system which can detect the ultrasound-controlled photons that have been scattered many times, centimeter-deep tissue fluorescence microscopic imaging can be achievable. This study is focused on developing a fundamentally different imaging technology: ultrasound-switchable fluorescence (USF), including the contrast agent development and the imaging system development. Basically, the USF contrast agent developed in this work is thermosensitive and its fluorescence emission has a switch-like relationship with temperature. Its fluorescence emission can be switched on or off by a focused ultrasound beam generated from a HIFU transducer within its focal volume. Then the diffused USF photons propagate out and are detected by a sensitive USF imaging system.

First, the excellent USF imaging contrast agents were developed by using the environment-sensitive fluorophores and thermosensitive polymers. We started investigating environment-sensitive fluorophores from visible

light range up to near infrared (NIR) range since only NIR light can penetrate centimeter-deep in opaque biological tissues. Two basic thermosensitive polymers and their co-polymers were used, including: poly (N-isopropylacrylamide) (PNIPAM) and pluronic. Both linear polymer and nanoparticle based USF contrast agents were explored. Second, a sensitive frequency domain (FD) USF imaging system and an effective signal identification algorithm were developed. The lock-in amplifier adopted in the FD-USF imaging system and the correlation algorithm significantly improved the SNR and detection sensitivity. Third, the feasibility of USF imaging in centimeter-deep tissue with high resolution was demonstrated in both tissue-mimicking phantoms and *ex vivo* biological tissues. Multi-color high-resolution USF imaging in centimeter-deep tissue with high SNR and picomole sensitivity were also achieved. Fourth, the feasibility of *in vivo* USF imaging was demonstrated in living mice by using different types of USF contrast agents via both intravenous and local injections.

In summary, the results provided in this work demonstrated for the first time the feasibility of centimeter-deep tissue fluorescence microscopic imaging with high SNR and picomole sensitivity via USF in tissue-mimicking phantoms, porcine muscle tissues, *ex vivo* mouse organs (liver and spleen), and *in vivo* mice. Multiplex USF imaging was also achieved, which is useful to simultaneously image multiple targets and observe their interactions. This work opens the door for future studies of center-deep tissue fluorescence microscopic imaging.

Table of Contents

List of Illustrations

List of Tables

Chapter 1

Introduction and Background

1.1 Cancer Diagnosis

1.1.1 Cancer

Cancer is one of the leading cause of death worldwide and was estimated to affect 1,685,210 new patients leading to 595,690 deaths in 2016 in the United States [1].

Cancer is a group of diseases that is caused by abnormal cell growth with potential to proliferate without stopping and to invade surrounding tissues. Normally, human cells grow and proliferate when the body needs. When cells become old or damaged, they will die and new cells take their place. However, when cell acquires a mutation that allows it to retain immortality and invade surrounding healthy cells, it becomes a tumor cell. Tumors can be divided into two groups, benign and malignant tumors. Benign tumors do not spread into nearby tissues. When removed, they usually don't grow back. In contrast, cancerous tumors are malignant, which can invade into surrounding tissues. In addition, as these tumors grow, some cancer cells can break off and travel to distant places to form new tumors. From benign tumor towards malignancy, tumor cells develop self-sufficiency in growth signals by activating oncogenes to cause pathological mitosis. They become insensitive to anti-growth signals by inactivating tumor suppressor genes and lose the ability to go through programmed cell death by suppressing apoptosis genes and pathways. Lastly, they develop unlimited proliferation potential by activating telomerases so that they can be immortal after many generations, overcome limitations on tumor growth by recruiting new blood vessels through sustained angiogenesis, and eventually gain mobility and the ability to invade surrounding tissues enabling further growth and metastasis to other parts of the body [2]. According to the database from National Cancer Institute, the five-year relative survival rate of breast cancer is 100% at stages 0 and I, which drops significantly to 22% at stage IV. Thus cancer diagnosis in early stage is critical to increase the survival rate of patients.

1.1.2 Cancer Diagnostic Methods

Most cancers are initially recognized either because of the appearance of signs or symptoms of disease or through medical tests. When abnormal tissue or cancer is found early, it may be easier to treat or cure. Medical tests can help diagnose cancer at early stage, before symptoms appear. Currently, there are four common diagnostic methods, including: biopsy, blood or urine test, genetic tests and medical imaging [3]. Among them, biopsy is a medical test commonly performed by pathologist involving extraction of sample cells or tissues for examination to

determine the presence or extent of a disease. It is an efficient way to determine whether the tumor is benign or malignant and can help differentiate between different types of cancer. However, excisional biopsies are invasive and cannot be used repeatedly. In addition, it is ineffective in understanding the dynamics of tumor progression and metastasis [4]. In the recent decades, biomedical imaging is playing a more important role in cancer prediction, detection and staging [3]. It has many advantages including real-time monitoring, noninvasive detection, and wide ranges of temporal and spatial resolution for biological and pathological processes. For instance, temporal resolution can go from milliseconds for protein binding and chemical reactions to years for diseases like cancer. Spatial resolution can go from nanometers (molecular level) to centimeters (organism level) [3]. The current role of imaging in cancer management is shown in Figure 1-1. Current biomedical imaging modalities includes X-ray based computed tomography (CT), magnetic resonance imaging (MRI), ultrasound (US), positron emission tomography (PET), and optical imaging. The comparison between these imaging modalities is shown in Table 1-1.

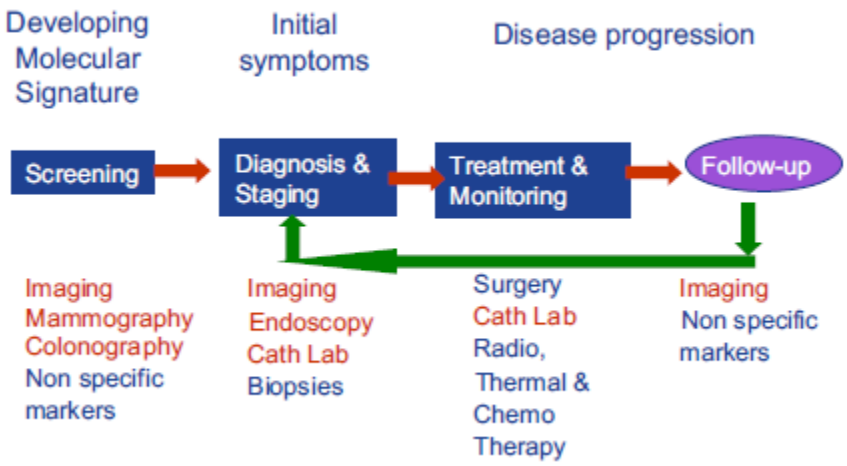

Figure 1-1 Current role of imaging in cancer management [3].

1.2 Introduction to Common Non-optical Imaging Techniques

1.2.1 X-ray based Computed Tomography

CT is the most widely used cross-sectional imaging method used in biomedical studies and it was developed in the 1970s. The use of CT has increased rapidly in all over of the world [5]–[7]. Basically, CT uses x-rays and an electronic detector array to record a series of projections which indicate the attenuation of x-ray in the pathway and create an image of a slice of tissue. The x-ray source rotates around the object within the scanner so that multiple x-

ray projections pass through the object. Then the structure of the object can be reconstructed by using a reconstruction algorithm. The principle is shown in Figure 1-2.

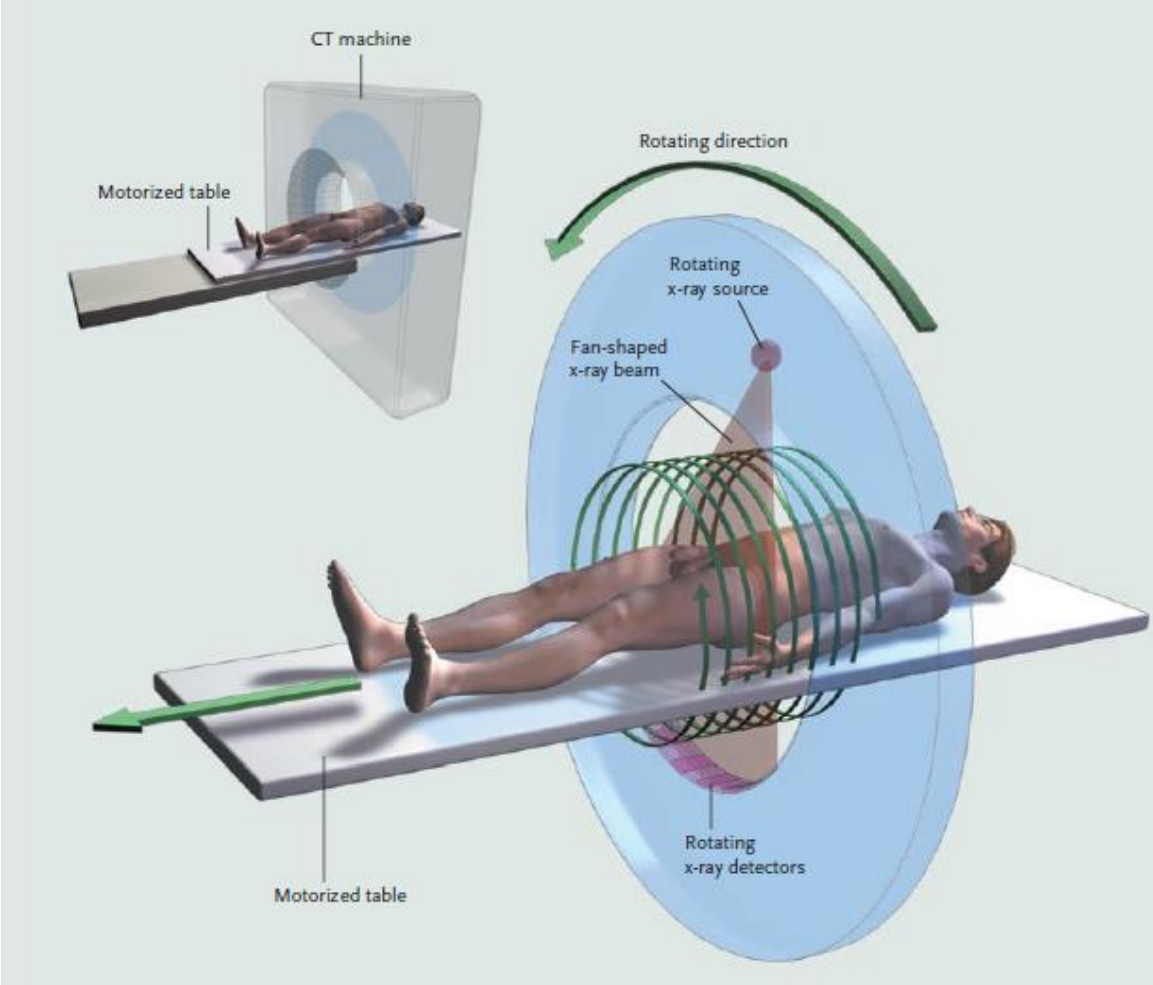

Figure 1-2 The basics of CT. A motorized table moves the patient through the CT imaging system. At the same time, a source of x-rays rotates within the circular opening, and a set of x-ray detectors rotates in synchrony on the far side of the patient. The x-ray source produces a narrow, fan-shaped beam, with widths ranging from 1 to 20 mm. In axial CT, which is commonly used for head scans, the table is stationary during a rotation, after which it is moved along for the next slice. In helical CT, which is commonly used for body scans, the table moves continuously as the x-ray source and detectors rotate, producing a spiral or helical scan. The illustration shows a single row of detectors, but current machines typically have multiple rows of detectors operating side by side, so that many slices (currently up to 64) can be imaged simultaneously, reducing the overall scanning time. All the data are processed by computer to produce a series of image slices representing a three-dimensional view of the target organ or body region [6].

X-rays are attenuated when they pass through the patient. The amount of attenuation depends on the type of tissue. Normally tissue with higher density like bone has more absorption of x-rays. The contrast in CT images depends on the difference in attenuation between adjacent tissues. The higher the attenuation of x-ray, the brighter the tissue in CT images. Similarly, the lower the attenuation, the darker the tissue in CT images. That is the reason why bone is white and soft tissues are relatively dark in CT imaging. CT is excellent in the evaluation of bone structures. In order to increase the contrast between normal structures and pathologic tissues and to visualize the vascular structures, iodinated contrast media is used. Iodine causes significant x-ray attenuation and therefore appears white in CT scans.

CT is a powerful structural imaging tool. The advantage of CT includes large penetration depth, excellent temporal and spatial resolution. However, its sensitivity is relatively low (~ mM), its cost is relatively high, and it is not capable to do multiplex imaging. In addition, it's not safe to perform longtime screening because of the use of ionizing radiation.

1.2.2 Magnetic Resonance Imaging

MRI uses a combination of static and time-varying magnetic fields to measure tissue structure and function through their effects on the magnetization of water protons in the body [7], [8]. In the presence of a strong external magnetic field, protons, or spins, tend to align with the external magnetic field, B_0. If the magnetization is out of alignment with B_0, it spirals along a helical pathway towards alignment, precessing about the axis of the magnetic field at a frequency determined by its strength:

$$\omega_0 = \gamma B_0 \qquad \text{[Eq. 1-1]}$$

For water protons, the gyromagnetic ratio γ is 42.58 MHz/T, and for commonly used magnetic field strengths B_0 of 1.5 to 7.0 T, the resonance or Larmor frequency ω_0 is in the radiofrequency range (64 to 300 MHz).

Spins can be excited out of thermal equilibrium by the pulsed application of a time-varying magnetic field B_1. B_1 is designed to oscillate in a plane perpendicular to the main field B_0 and contains a narrow range of frequencies centered on ω_0, spiraling the precessing magnetization away from the B_0 axis into what is known as the transverse plane. This precessing magnetization is the source of the NMR signal, producing an oscillating magnetic field that induces a current in a coil placed near the sample. Spins in various tissues relax from excitation back to thermal

equilibrium at different rates through interactions with the local magnetic fields of neighboring protons and other molecules, giving rise to tissue-specific variations in signal strength.

To localize the measured signal and create an image of the magnetization, an additional set of coils is used to create linear spatial variations in B_0. By applying such a gradient in one direction and then restricting the range of frequency components in the B_1 excitation pulse to a subset of the resulting proton resonance frequencies, excitation can be limited to a tissue slice of desired thickness. Within this slice, gradients in resonance frequency applied for a given duration create a spatial frequency. For objects of limited size, we can sample the voltage induced in the receiver coil after applying gradients in two directions for a variety of durations, measuring signal over the entire range of spatial frequencies required to fully describe the object in the spatial frequency domain, referred to as k-space. Then an object domain image of the magnetization can be recovered using an inverse Fourier transform of the acquired k-space data.

Table 1-1 Comparison of imaging modalities

	Ultrasound	CT	MRI	PET	Optical imaging
Spatial resolution	Scalable (0.3-3 mm)	~ 1 mm	40 μm-1 mm	1-5 mm	Scalable (0.3 μm-10 mm)
Imaging depth	Scalable (3-25 cm)	Excellent	Excellent	Excellent	Good
Sensitivity	Relatively poor	Low ~mM	Low μM-mM	High fM-pM	High fM-nM
Safety	Very good	Ionizing radiation	Very good	Ionizing radiation	Very good
Data acquisition	Fast	Fast	Slow	Slow	Fast
Cost	$	$$$$	$$$$$$$$	$$$$$$$$	$
Multiplex imaging	No	No	No	No	Yes

Relaxation is highly tissue dependent. The time constant of an exponential function approximating the rate at which the magnetization returns to alignment with B_0 is called T_1, and the time constant describing the rate at which the transverse magnetization returns to zero is called T_2. Examples of T1-weighted and T2-weighted image are shown in Figure 1-3. The sequencing of radiofrequency excitation pulses, magnetic field gradients, and data acquisition can be used to weight the measured signal by a desired contrast mechanism, allowing many different tissue properties to be spatially mapped, including the density of protons in a sample, their T_1 and T_2 relaxation rates, water diffusion, blood oxygenation, magnetic susceptibility and temperature. Several contrast mechanisms are useful in identifying cancer and defining target boundaries for therapeutic interventions.

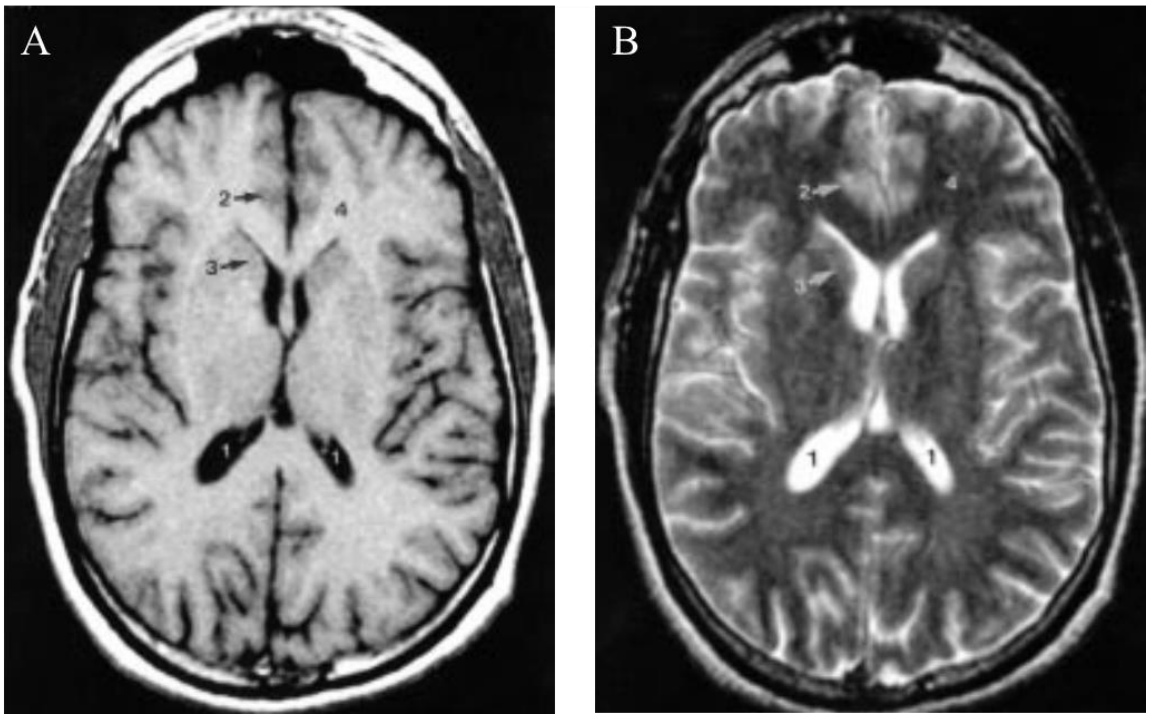

Figure 1-3 (A) T1-weighted axial MR image shows relative signal of cerebrospinal fluid *(1)* that is darkest, followed by gray matter (cortex, *2;* basal ganglia, *3*), and white matter *(4)*. (B) On T2-weighted axial MR image, cerebrospinal fluid (CSF) *(1)* is brightest, followed by gray matter *(2,3)*, then white matter *(4)* [7].

MRI can provide both structural and functional information. Similar to CT, it has large imaging depth and excellent spatial resolution. Because it doesn't use ionizing radiation, MRI is quite safe for patients. However, its temporal resolution is relatively poor (~ mins) and its sensitivity is low (μM-mM). In addition, MRI is quite expensive and not capable to do multiplex imaging.

1.2.3 Ultrasound

Ultrasound imaging is one of the most common diagnostic imaging methods used in tumor detection, such as breast, prostate, liver, pancreatic, uterine, thyroid [3]. Ultrasound is a mechanical wave that propagates within a medium inducing particle vibrations at a frequency above 20 kHz. During the propagation, the energy is attenuated by absorption, scattering, and reflection. Acoustic impedance of a medium (Z) is an important parameter for describing material acoustic properties. For a plane and progressing US wave, it can be calculated by the following equation:

$$z = \rho_0 c \qquad \text{[Eq. 1-2]}$$

ρ_0 is the density of the medium and c is the speed of ultrasound wave in the medium. Normally the speed of sound in water is 1480 m/s. Soft tissues have similar impedance which is close to water except lung and bone has higher acoustic impedance. The most important phenomenon of ultrasound that has been used in medical imaging is the inherent property to get reflected from interfaces between different tissues in the patient, which have different acoustic impedance. As the ultrasound waves penetrate body tissues with different acoustic impedance along the path of transmission, some are reflected back to the transducer (echo signals) and some continue to penetrate deeper. The reflected signals were recorded and processed to generate an image. This imaging method is called pulse-echo approach [9]–[11].

There are several common modes for ultrasound imaging, including A-mode, B-mode, and C-mode [12]. A mode is the simplest type of ultrasound. A-mode presentation of ultrasound images involves observing the amplitude of the echoes emerging from the acoustic mismatch boundaries in a target sample or tissue as a function of time, termed as A-line. Assuming that the speed of sound is known for a given medium, the distance between the boundaries and the ultrasound transducer can be measurable. The main aim of A-mode imaging is to reveal the location of echo-producing structures but only in the direction of the ultrasound beam. A B-mode image is the combination of A-lines at different locations that can be viewed as a two-dimensional cross-section image. The amplitude of each echo is replaced by the corresponding brightness value at the respective co-ordinate location. A C-mode image is formed in a plane orthogonal to a B-mode image. It is acquired at a specific depth from an A-mode line in x-y plane. Figure 1-4 shows the results of an experiment in which a tube filled with water was imaged by ultrasound.

Compared with CT and MRI, ultrasound is portable, free of radiation risk, and relatively inexpensive. As another anatomical imaging method, it has good spatial resolution and imaging depth which is frequency dependent and excellent temporal resolution which can achieve real-time imaging. However, similar to CT and MRI, it is lack of sensitivity and multiplex imaging capability.

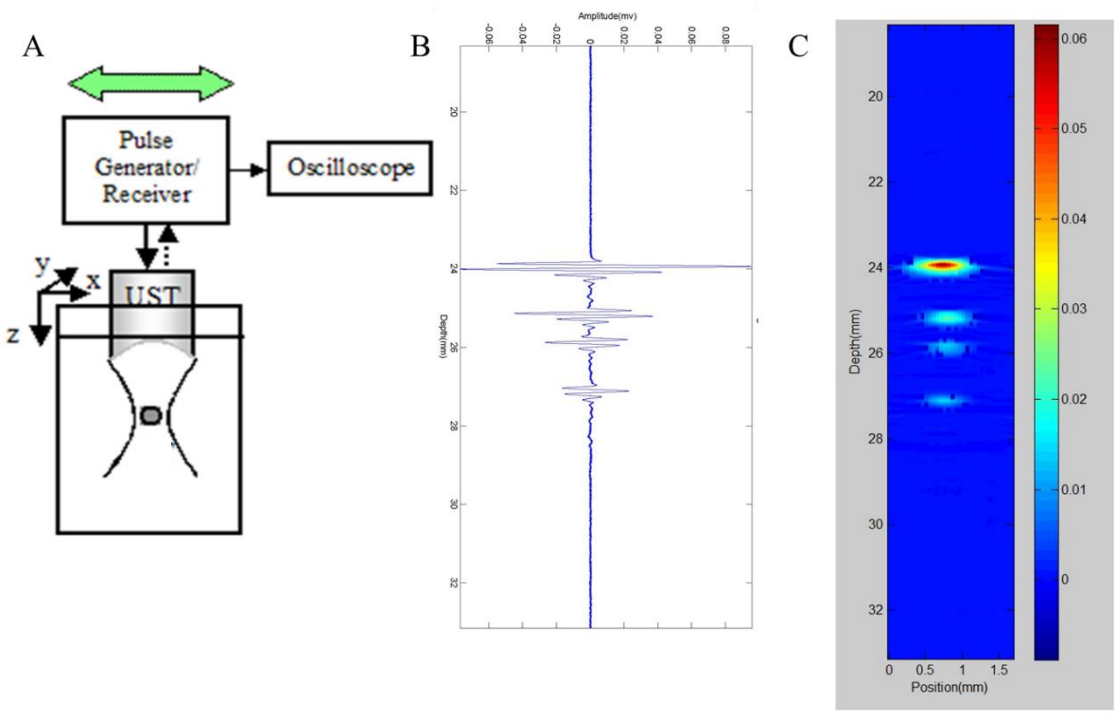

Figure 1-4 The example of A-mode and B-mode ultrasound imaging of a tube filled with water. (A) The experiment setup. (B) A-line showing the four boundaries of the tube. (C) B-mode image showing the four boundaries of the tube. UST: ultrasound transducer.

1.2.4 Positron Emission Tomography

PET is a nuclear medical imaging technique for the quantitative measurement of physiologic parameters in the body. It detects pairs of gamma rays emitted indirectly by a positron-emitting radioactive tracer, which is introduced into the body [13], [14]. PET is heavily used in clinical imaging of tumors and exploration of cancer metastasis. Different radioactive tracers make it capable to image the concentration of different types of molecules. Most commonly used are carbon-11, oxygen-15, nitrogen-13, and fluorine-18 [13].

Imaging of regional tracer concentration is accomplished by the unique properties of positron decay and annihilation. In an unstable nucleus, a proton converts to a neutron under emission of a positron. After the emission

from the parent nucleus, the positron traverses a few millimeters through the tissue until it becomes thermalized by electrostatic interaction between the electrons and the atomic nuclei of the media and combines with a free electron to form a positronium. The positronium decays by annihilation, generating a pair of gamma rays which travel in nearly opposite directions with an energy of 511 keV each. The opposed photons from positron decay can be detected by using pairs of collinearly aligned detectors in coincidence. The principle is shown in Figure 1-5. Normally the detector pairs of a PET system are installed in a ring shape, which allows measurement of radioactivity along lines through the organ of interest at a large number of angles and radial distances. Subsequently, this angular information is used in the reconstruction of tomographic images of regional radioactivity distribution.

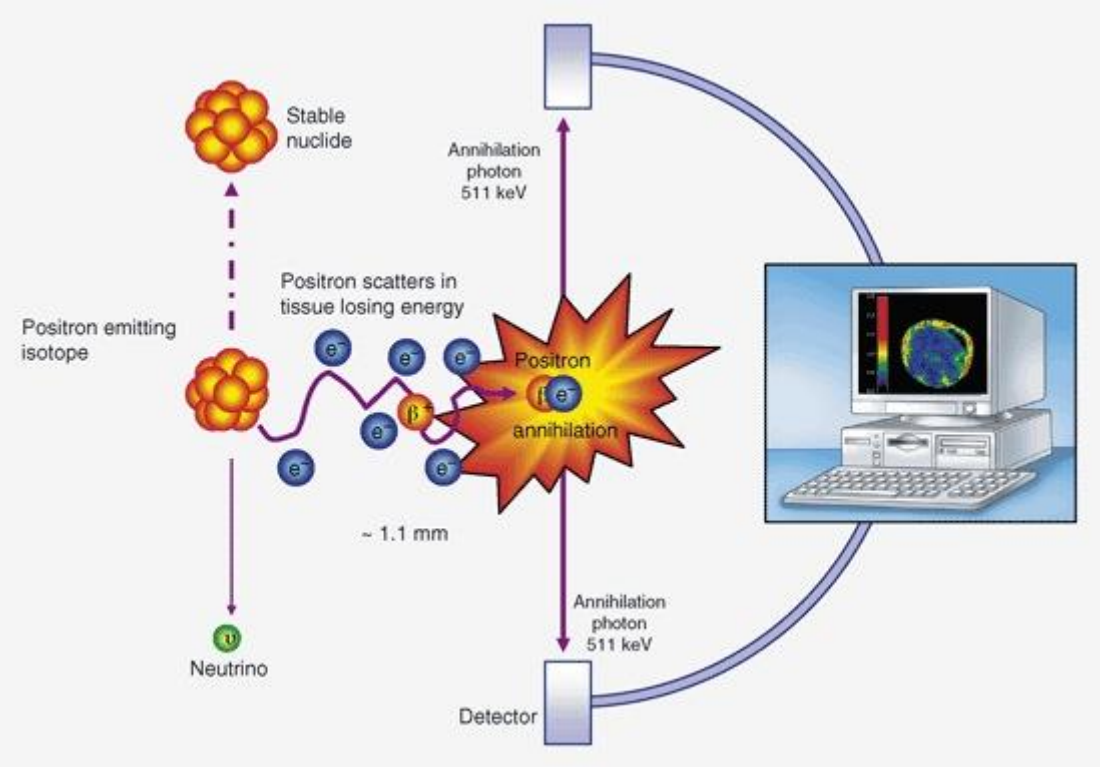

Figure 1-5 Principles of PET [15].

PET is a very powerful functional imaging technique, whose specificity and sensitivity are excellent which make it possible to do molecular imaging. However, it has high risk of safety due to the adoption of radioactive agents. Unlike anatomical imaging methods such as ultrasound and CT, its spatial resolution is relatively poor (1-5 mm) although it has a large imaging depth. Similar to MRI, PET needs a long time for data acquisition and it is very expensive. In addition, PET is not capable to do multiplex imaging.

1.3 Introduction to Pure Optical and Ultrasound-Combined Optical Imaging Techniques

Fluorescence imaging has been developed for many years and gained much attention as a powerful new modality for molecular imaging in biomedical studies [16]–[18]. Basically, it detects the fluorescence emitted from labeled molecules in biological samples. It is relatively cost-efficient, flexible in the selection of imaging probes (such as fluorescent proteins, organic dyes, quantum dots and nanoparticles, metal-ligand complexes and fluorescent beads), and highly sensitive to imaging probes (fM-nM). Similar to US and MRI, it is safe because it utilizes nonionizing radiation [17]–[19]. Most importantly, fluorescence techniques can provide unique sensitive and specific contrast information that are related to local microenvironments, such as tissue pH, temperature, and gas/ion concentrations. This information may indicate tissue function and abnormalities, including: angiogenesis, lymphangiogenesis, hypoxia, tumor metastasis, and can also provide guidance for drug delivery and targeted therapy [20]–[22].

Optical microscopy which focuses light into a tiny spot in tissue, such as conventional wide-field microscopy and confocal or multiphoton microscopy, is excellent in spatial resolution (<1 μm) and can provide subcellular images [23], [24]. However, its imaging depth is significantly limited in opaque biological tissues (<1 mm) due to strong light scattering [24]. The principle of optical microscopy is shown in Figure 1-6. Besides cellular or subcellular information at very superficial tissue, deep tissue information is also very attractive but is extremely difficult to detect using current microscopic imaging techniques [23]. Therefore, deep-tissue (>>1 mm) high-resolution imaging is desirable for both tissue biology studies and preclinical/clinical applications [17], [23]–[25]. To image deep tissue, instead of focusing light, fluorescence diffuse optical tomography (FDOT) takes the advantage of the diffused photons which have been scattered many times before being detected (see Figure 1-7). Normally, those diffused photons can penetrate centimeter-deep tissue with far red or near-infrared (NIR) wavelength, but suffers from poor spatial resolution (millimeters) [19], [26]–[28]. As a result, micro-information is lost. Therefore, fluorescence microscopic imaging in deep tissue (> 1 cm) is highly desired.

Optical and ultrasonic techniques are commonly used for noninvasive tissue imaging [26], [29], [30]. They share many features, such as cost efficiency, safety, and flexibility in the selection of the well-developed and inexpensive imaging contrast agents [31]. They are also complementary. For example, imaging deep tissue (30–50 mm) optical techniques have very low spatial resolution (3–5 mm) due to strong light scattering [31]; however, ultrasound is much less scattered by tissue (two to three orders of magnitude) and has relatively higher spatial resolution (below a few hundred micrometers) [29], [30], [32]. Microbubbles are commonly used as ultrasound

contrast agents and usually restricted inside a tissue vascular system because of their micrometer size [29]. However, optical contrast agents can simultaneously image both vascular and extravascular molecular targets *via* spectroscopic techniques, because of their relatively small size (<< 1 micron) [17], [23], [25], [28], [30]–[32]. Therefore, ultrasound and optical hybrid imaging techniques, such as photoacoustic imaging and ultrasound-medicated optical imaging, have been intensively developed during the past years [29], [30], [33], [34]. These hybrid techniques take advantage of both techniques and achieve unique features that are unable to be achieved by individual ones [30], [34].

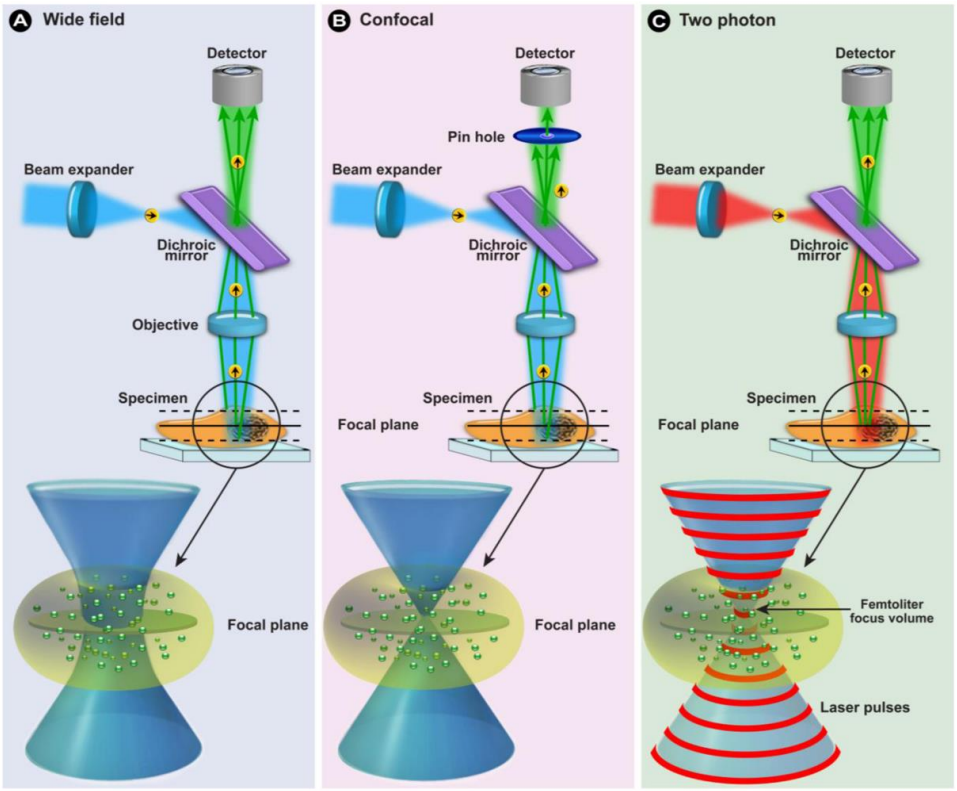

Figure 1-6 In confocal microscopy (B) the concept of illuminating the sample with excitation light (e.g., blue light) and the sample emitting light with a longer wavelength (e.g., green light) is identical to the general principles of fluorescence in wide field microscopy (A). The differences to wide field microscopy are: (i) the excitation laser light is scanned over the sample and the emitted light originates from this area; (ii) on the detection beam path a pinhole aperture in front of the detector prevents light emitted from above or below the focal plane (dotted lines) from reaching the detector; and (iii) because only light from the focal plane (solid line) reaches the detector an optical section is generated. (C) In two-photon microscopy, a high flux of excitation photons from a pulsed laser caused the simultaneous absorption of 2 long wavelength photons and emission of a photon with a shorter wavelength (anti-Stokes). Because excitation is restricted to a small femtoliter focal volume, out-of-focus emission is negligible and

thus no pinhole is required [35].

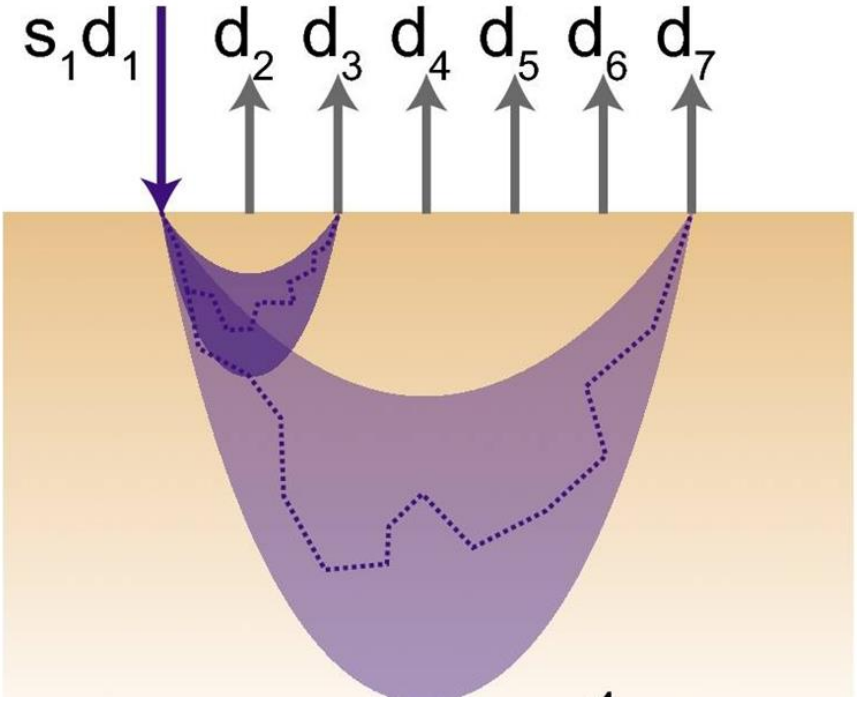

Figure 1-7 The principle of FDOT [36].

To quantitatively compare these techniques, depth-to-resolution ratio (DRR) is usually adopted and high DRR is preferred [19], [30]. Figure 1-8 schematically summarized the major optical and ultrasonic related imaging techniques. Note that the values of DRR listed in Figure 1-8 are for a general comparison among different techniques and the specific value for each technique may vary for different applications. Diffuse optical tomography (DOT) and laminar optical tomography (LOT) are two pure optical imaging techniques and can image several millimeter to centimeter deep tissue with low resolution (submillimeter to millimeters) [26], [28], [36]. They are roughly located on the line of DRR=10. This DRR is fundamentally limited by tissue light scattering [31]. Low-frequency ultrasound (LFUS), high-frequency ultrasound (HFUS), photoacoustic tomography (PAT), photoacoustic microscopy (PAM) and optical coherence tomography (OCT) have improved the DRR up to ~100 [19], [30]. This DRR is fundamentally limited by acoustic diffraction (except OCT) [19], [30]. Optical microscopy, such as optical coherence microscopy (OCM), two photon microscopy (TPM), and confocal laser scanning microscope (CLSM), may theoretically locate around the line of DRR=1000, but with a limited imaging depth (<1 mm, see the horizontal dashed line) [24], [37],

[38]. This DRR is fundamentally limited by the optical diffraction and scattering [24], [37]. To break the light diffraction limit, super-resolution optical microscopy has been intensively developed recently [39]–[41], such as stimulated emission depletion microscopy (STED), photoactivation localization microscopy (PALM), and stochastic optical reconstruction microscopy (STORM) [42], [43]. While these super-resolution techniques can provide much higher spatial resolution (tens of nm) than conventional optical microscopes, their imaging depths are usually limited (tens of microns) [42], [43]. Therefore, the DRR may remain ~1000 [44] (not shown in Figure 1-8).

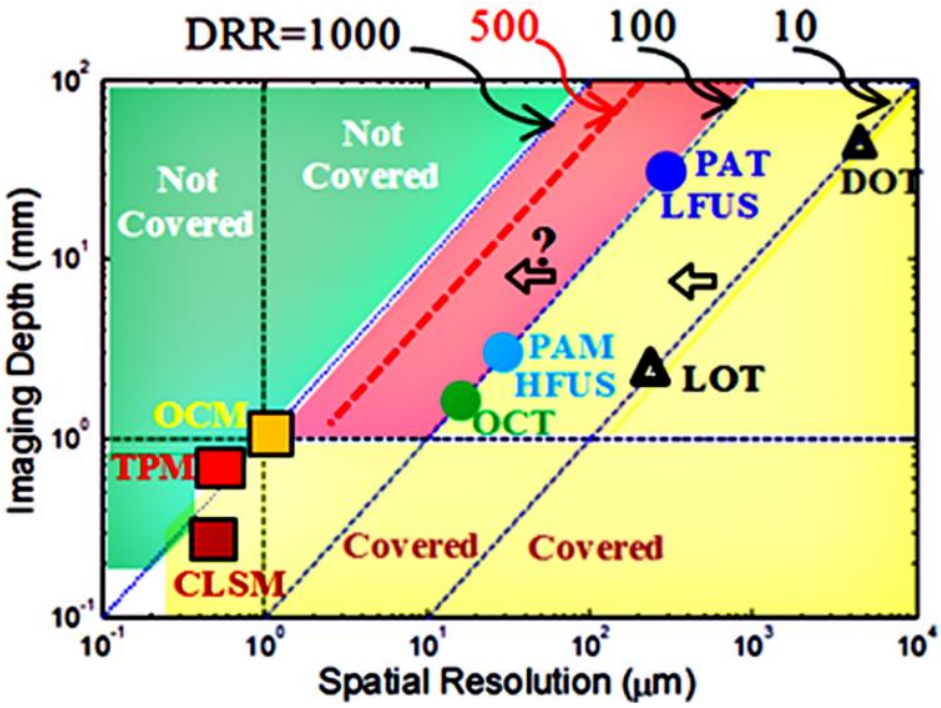

Figure 1-8 Major related optical and ultrasonic imaging techniques.

In Figure 1-8, the horizontal axis represents the spatial resolution in micrometers (μm) and the vertical axis indicates the imaging depth in millimeter (mm). The four 45°-tilted dashed lines represent DRR=10, 100, 500, and 1000, respectively. Theoretically, the yellow area has been covered by the above-mentioned imaging techniques. The light green area has not been covered due to various fundamental physics limits. The third area, shown in red, has a DRR between 100 and 1,000. Currently, optical techniques based on the detection of scattered light (such as DOT and LOT) have difficulties in reaching this area due to strong tissue light scattering [26], [28], [31], [34], [36]. Ultrasound and photoacoustic techniques are difficult to reach beyond the area of DRR>200 (for imaging depth >1 mm) because of the fundamental physics limit of the acoustic diffraction [19], [30]. Accordingly, a fundamental question is whether

it is feasible to develop a new imaging method that is located inside the red area with a DRR>200 (breaking the acoustic diffraction limit in ultrasound and PA techniques) and an imaging depth >>1 mm (breaking the imaging depth limit in optical microscopy). To address this question, one may need to think outside the box to develop some techniques that are fundamentally different from currently existing imaging techniques. Recently, we proposed and developed a fundamentally different technique, ultrasound-switchable fluorescence (USF) imaging [39], [40], [45], [46]. Compared with other imaging modalities, it stands out in the following aspects: high spatial resolution (hundreds of microns), large imaging depth (> 1 cm), high sensitivity (picomole molecule level), excellent safety (non-ionizing radiation), low cost, capable to do multiplex imaging, and feasible to provide tissue structural, functional and molecular information.

1.4 Ultrasound-Switchable Fluorescence (USF) Imaging

1.4.1 Principles of USF Imaging

The basic mechanisms have been discussed in our recent publications in [39], [45], [46]. Briefly, USF imaging requires two basic elements: (1) imaging contrast agents and (2) an acoustic-optical imaging system. The imaging principle is to use a focused ultrasound beam to externally and locally control fluorophore emission from a small volume (close to or even smaller than the ultrasound focal volume). The imaging principle is schematically shown in Figure 1-9. Ideally, without applying ultrasonic energy, the contrast agents should be dark (off, no fluorescence emission). Any detected fluorescence signal should be considered as noise and may be generated from tissue autofluorescence and/or non-100%-off USF contrast agents, which should be extremely weak in USF imaging. When the ultrasonic energy is turned on and focused inside the sample, USF contrast agents in a small volume (usually within the ultrasound focal volume) are switched on and fluoresce. By scanning the ultrasound focus, the distribution of the USF contrast agents can be imaged [39], [45], [46].

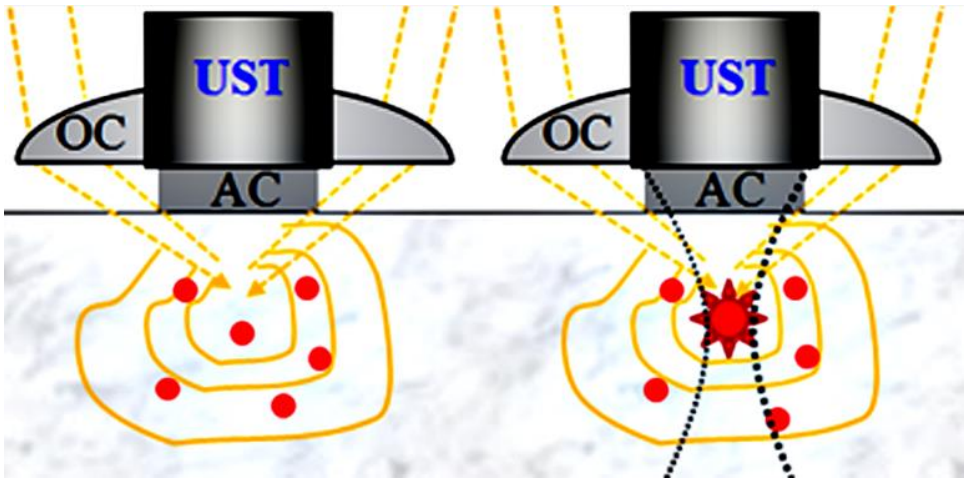

Figure 1-9 Schematic diagrams show the basic principles of USF imaging. The left panel shows the case when ultrasound transducer (UST) is off and the fluorophores are off. The right panel represents that the UST is on and some fluorophores in the focal volume are switched on. OC, optical condenser; AC: acoustic coupling.

Theoretically, there are two types of USF contrast agents: (1) fluorophore-quencher-labeled microbubbles (F–Q microbubbles) [41], [47]–[49] and (2) fluorophore-labeled thermosensitive polymers (FTP) or fluorophore-encapsulated nanoparticles (FEN) [39], [45], [46], [50].

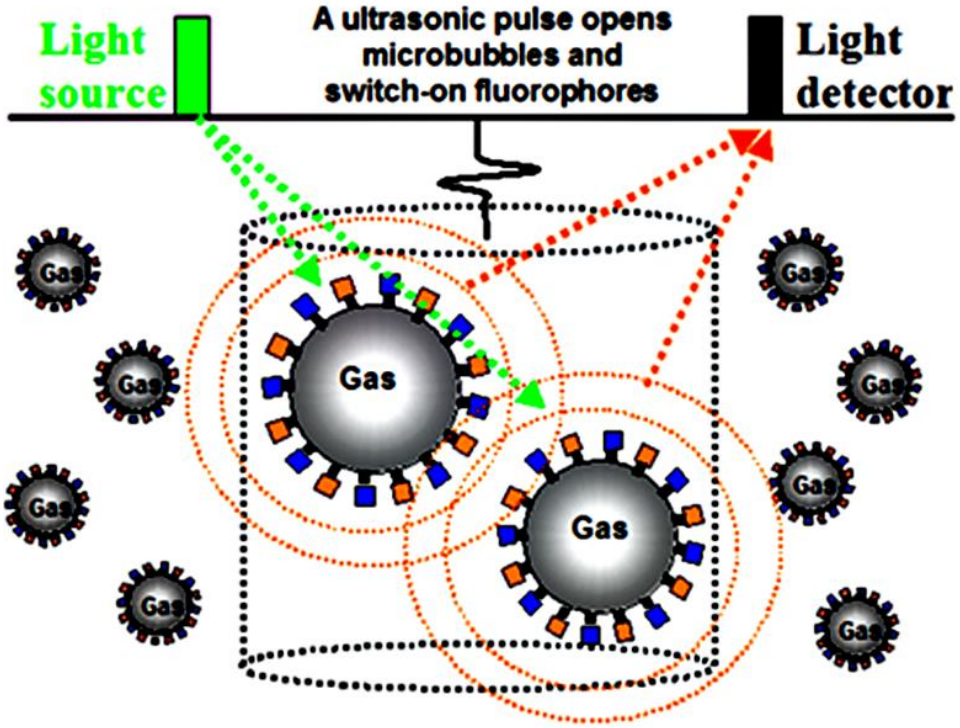

Figure 1-10 Schematic diagram shows the concept of USF based on fluorophore-quencher-labeled microbubbles; F, fluorophores; and Q, quenchers. An ultrasound pressure pulse switches "on" the fluorophores. The dotted cylinder represents ultrasound focal zone in which the ultrasound interacts with F–Q microbubbles. The green dotted arrows indicate the excitation light. The dotted orange circles and arrows represent the fluorescence emission from the expanded (switched-on) microbubbles.

In the first type, fluorophores and quenchers are attached on the microbubble surface *via* various types of labeling techniques. Initially, the fluorophores are significantly quenched by quenchers (or *via* self-quenching) so that no or very weak fluorescence can be detected. To switch on the fluorescence signal, a short and focused ultrasound (mechanical) pressure pulse is used to significantly expand microbubbles. Therefore, the average molecular distance between the fluorophores and quenchers on the microbubble surface can be significantly increased during the expansion cycles (or the surface concentration of the fluorophores on the bubble surface can be significantly reduced if only one type of fluorophores is labeled). Thus, the quenching efficiency is dramatically reduced, which can switch on the fluorescence from the fluorophores. Figure 1-10 displays a schematic diagram to show this concept. The large F–Q microbubbles represent that a negative ultrasound pressure cycle significantly increases the bubble size and reduces the quenching efficiency so that the fluorophores can emit fluorescence signal. The small F-Q microbubbles are located outside of the ultrasound focal volume so the fluorophores remain quenched (off). However, the use of microbubble contrast agents for *in vivo* imaging is technically challenging due to their instability to multiple US pulses, short circulation time and heterogeneous size distributions. It is also intrinsically difficult to evenly distribute fluorophores on the lipid shell due to the formation of concentrated lipid islands, which compromises the switching efficiency of fluorescent emissions. Furthermore, the microscale size of bubbles restricts the use of these contrast agents to the circulatory system, since microbubbles stay within the vascular compartment and do not leak out into the extra-vascular space [51].

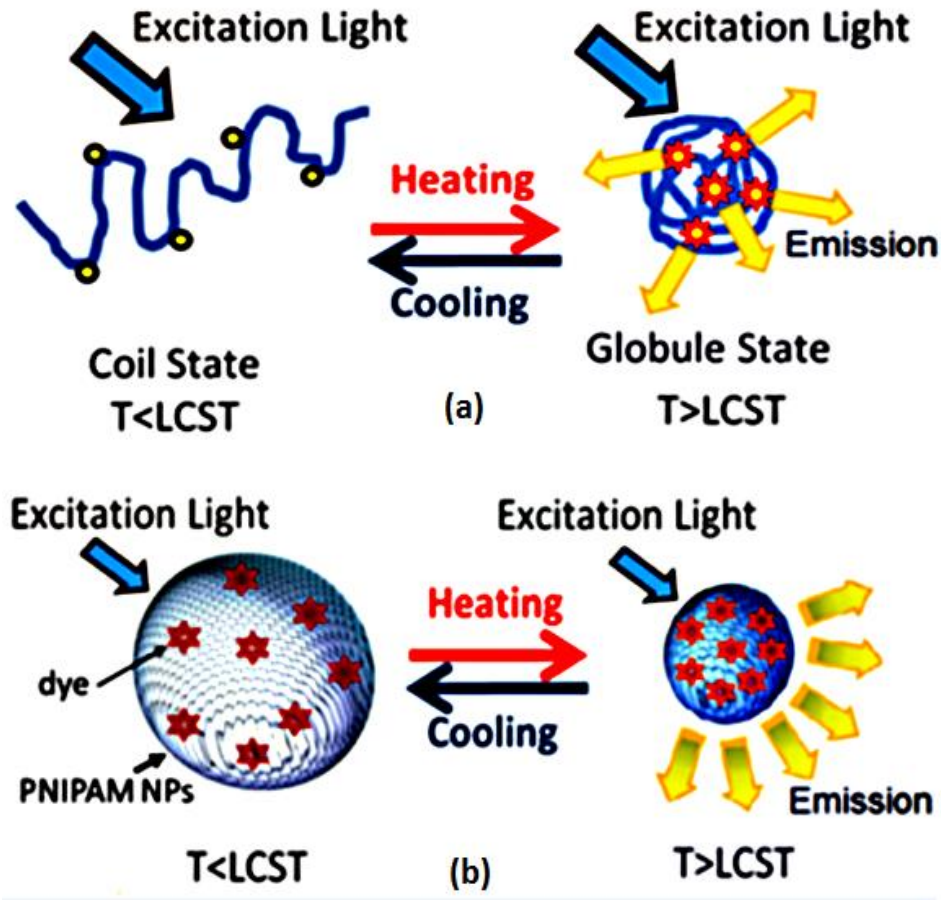

Figure 1-11 Schematic diagrams showing the USF principle based on (a) a polymer chain structure, and (b) a NP structure.

In the second type, polarity-sensitive fluorophores (high-quantum yields in low polarity environment) are either conjugated on the chain of thermosensitive polymers [Figure 1-11(a)] or encapsulated into nanoparticles that are made of thermosensitive polymers [Fig. 4(b)]. To control the fluorescence signal, a relatively long and focused ultrasound pulse (ranging from a few to hundreds of milliseconds) with high intensity is adopted to heat the sample up to a few degrees Celsius in the focal volume. When the temperature (T) of the USF contrast agents is heated up above the lower critical solution temperature (LCST) of the thermosensitive polymers or nanoparticles, these polymers or nanoparticles experience a reversible phase transition. This phase transition (between the two states of T<LCST and T>LCST) leads to a significant change in the polarity microenvironment of the polymer or nanoparticle. Thus, the polarity-sensitive fluorophores are "off" when T<LCST and "on" when T>LCST, which shows a switch-like fluorescence emission property [39], [45], [46], [50], [52]. Specifically, when T<LCST, the polymer chain is

elongated, which is called a coil state. When T>LCST, the polymer chain shrivels into an insoluble glob, which is called a globule state. Because the polarity of the microenvironment is significantly changed between the two states, the polarity-sensitive fluorophores show a switch-like fluorescence emission property [52]. A similar mechanism applies to the nanoparticles. When T<LCST, nanoparticles are inflated with polarized solvent molecules that quench the fluorophores. When T>LCST, the nanoparticles are dramatically shrunk and the polarized solvent molecules (usually with much lower molecular weight than the fluorophores) are squeezed out [53], [54]. Thus, the fluorophores fluoresce significantly. This concept is schematically displayed in Figure 1-11(b). A high-intensity focused ultrasound (HIFU) transducer can be used to externally and rapidly increase the temperature of the tissue above the threshold temperature to switch on the fluorophores (due to tissue absorption of acoustic energy). After ultrasound exposure, the thermal energy is diffused quickly and the temperature recovers to background temperature. Thus, fluorophores are switched off. The fluorophores outside the focal zone always remain off due to T<LCST.

1.4.2 Mechanisms of Breaking Acoustic Diffraction Limit

When adopting fluorophore-labeled thermosensitive polymers or nanoparticles, the spatial resolution can be further improved based on two unique mechanisms, as has been demonstrated recently [39], [40], [45], [46]. (1) When a nonlinear acoustic effect occurs, both lateral and axial acoustic and thermal focal sizes are dramatically reduced below the diffraction-limited size. This means the spatial resolution of the USF technique can be higher than the ultrasound and PA techniques when using the same ultrasound frequency [40]. (2) Unlike ultrasound and PA techniques, the spatial resolution of the USF technique depends on the size of the region where the fluorophores can be switched on. Because of the existence of a threshold of ultrasound-induced temperature to switch on fluorophores, USF fluorophores can be switched on only in a volume where ultrasound energy is above the threshold. Thus, the size of the region where fluorophores can be switched on is usually smaller than the actual focal size of the ultrasound. With appropriate selection of the threshold and ultrasound power, the spatial resolution of USF technique can be further improved in comparison with the spatial resolution determined by the nonlinear-effect-produced focal size.

1.5 Specific Aims

This dissertation describes the development of a fundamentally different imaging technique: ultrasound-switchable fluorescence imaging to achieve high spatial resolution in centimeter-deep tissue with high SNR and picomole sensitivity. This approach is able to compensate the pitfalls of currently existing imaging modalities and stands out in the following aspects: high spatial resolution (hundreds of microns), large imaging depth (> 1 cm), high

sensitivity, high SNR, cost-efficiency, excellent safety (no ionizing radiation), and capability of multiplex imaging. The development includes excellent NIR USF contrast agents and sensitive USF imaging systems. The aims were addressed in the following series of studies:

1. Development of basic USF imaging contrast agents.

In Chapter 2, we developed more than twenty USF imaging contrast agents with environment-sensitive fluorophores and thermosensitive polymers. Different fluorophores and polymer structures (linear or nanoparticle) were explored. Five parameters were defined to compare different contrast agents and a specific fluorescence intensity and lifetime measurement system was developed to characterize those agents. These contrast agents have high lifetime on-to-off ratio (τ_{on}/τ_{off}), high intensity on-to-off ratio (I_{on}/I_{off}), narrow temperature transition bandwidth (T_{BW}), and adjustable temperature threshold (T_{th}). Six FRET systems were reported in this study in which the τ_{on}/τ_{off} and I_{on}/I_{off} of donor fluorophore were significantly improved.

2. Development of NIR USF imaging contrast agents.

In Chapter 3, in order to achieve deep tissue imaging, two NIR environment-sensitive fluorophores were characterized first to investigate their environment-sensitivity. Then a family of NIR USF contrast agents based on them and two types of polymer structures were synthesized and characterized. They have excellent switching properties including high fluorescence intensity on-and-off ratios, the narrow transition bandwidth, the adjustable switching threshold, and the excellent switching repeatability. With the help of those contrast agents, centimeter-deep tissue fluorescence high-resolution imaging with good SNR and sensitivity becomes achievable.

3. Development of sensitive USF imaging systems and an effective signal identification algorithm.

After developing USF contrast agents, in Chapter 4, we explored and developed sensitive USF imaging systems from continuous wave system to frequency domain system which can sensitively detect USF photons. Specific USF temporal patterns were observed and investigated. In the meantime, an effective signal identification algorithm was programmed which can exclusively differentiate USF signals with background noise and differentiate different types of USF agents to achieve multiplex imaging.

4. USF microscopic imaging in centimeter-deep tissue-mimicking phantoms and *ex vivo* tissue samples.

In Chapter 5, centimeter-deep tissue fluorescence microscopic imaging via ultrasound-switchable fluorescence was demonstrated in both tissue-mimicking phantoms and *ex vivo* tissue samples including porcine muscle tissue and *ex vivo* mouse organs. The newly developed approach was validated with traditional diffuse

fluorescence imaging and ultrasound imaging regarding of target shape, position and size. Multiplex USF imaging was also demonstrated, which is very useful in simultaneously imaging multiple targets in the future. The SNR, spatial resolution and sensitivity were calculated to show the performance of this new imaging modality.

5. Evaluation of the *in vivo* feasibility of USF.

In Chapter 6, the feasibility of USF for *in vivo* studies was demonstrated by applying USF in living mice. First, an *in vivo* USF imaging system was developed, including an anesthesia system, a physiological monitoring system and frequency domain USF imaging system. Then, USF imaging was performed on 9 mice to acquire *in vivo* USF images. Two types of contrast agent with different LCSTs and two different injection methods including intravenous injection and local injection were investigated to evaluate the *in vivo* capability of USF.

The last chapter summarizes all the results and concludes this dissertation. Limitations and future directions are discussed.

Chapter 2

Develop Basic USF Imaging Contrast Agents

2.1 Introduction

It is always intriguing to reveal information in deep tissue by noninvasively imaging techniques, which is critical for studying tissue structures, functions, and dysfunctions [17], [25]. However, most biological tissues are optically opaque to human eyes. Therefore, an imaging technique is indispensable [25]. Fluorescence microscopy has been widely used in biological and medical studies because it can provide micron resolution images with structural, functional and molecular contrast in cells or tissues [28]. Unfortunately, it fails to image deep tissues due to the strong light scattering that prevents light from being tightly focused. Fluorescence diffuse optical tomography (FDOT) takes advantage of the tissue scattered light and can thus image centimeter-deep tissues, whereas it suffers from poor spatial resolution (a few millimeters) [19], [26]–[28], [55], [56]. As a result, the majority of micro-information in deep tissues is lost in FDOT. To reveal such essential information located inside organs away from an instrument-accessible surface, deep-tissue high-resolution fluorescence imaging is highly desired.

Several techniques with an aim to achieve deep-tissue high-resolution fluorescence imaging have been proposed and demonstrated, such as multispectral optoacoustic tomography (basing on photoacoustic techniques) [57] and ultrasound-modulated fluorescence imaging (basing on ultrasound-modulated photon techniques) [58], [59]. A new technique has been developed [39], [60], [61] very recently, *i.e.* ultrasound-induced temperature-controlled fluorescence (UTF). In a typical model of UTF, a high-intensity-focused-ultrasound (HIFU) wave is delivered into a sample. In the focal volume of the HIFU beam, the sample temperature is raised by a few Celsius degrees due to the absorption of acoustic energy. At the same time, the sample has been distributed with a temperature-sensitive fluorescent imaging contrast agent. The HIFU-induced temperature increase in the focal volume has been found to significantly enhance the fluorescence emission of the contrast agent. By detecting the HIFU-enhanced fluorescence emission photons and scanning the HIFU focus through the area of interest, one can therefore acquire an image of the distribution of the temperature-sensitive contrast agent. UTF shows significant improvement in spatial resolution in comparison with FDOT. This is a paramount step to achieve the goal of deep-tissue high-resolution fluorescence imaging.

Aiming to efficiently control the fluorescence emission from the contrast agents using a HIFU pulse, we recently proposed and demonstrated a concept of ultrasound-switchable fluorescence (USF), which relies on a

temperature-sensitive fluorescent polymer [39], [45], [46], [50]. Basically, the fluorescent intensity and lifetime of the polymer showed a switch-like relationship with the HIFU-induced temperature. When the temperature was below a threshold, the polymer weakly fluoresced along with a short lifetime; when the temperature was above the threshold, the polymer strongly fluoresced along with a long lifetime. In a turbid medium, the fluorescent polymer functioned as like a deeply-seated light source that could be switched on-and-off by an externally-applied HIFU transducer, when they were illuminated by excitation light.

The promising USF technique highly relies on a unique contrast agent, which must be extremely sensitive to temperature and thereafter of switchable fluorescence. To quantify the performance of a USF contrast agent, the following parameters are defined: (1) peak excitation and emission wavelengths (λ_{ex} and λ_{em}); (2) the fluorescence intensity ratio between on and off states (I_{On}/I_{Off}); (3) the fluorescence lifetime ratio between on and off states (τ_{On}/τ_{Off}); (4) the temperature threshold to switch on fluorophore (T_{th}); and (5) the temperature transition bandwidth (T_{BW}). To achieve the best signal-to-noise ratio, an ideal USF contrast agent should have the following properties: (a) both λ_{ex} and λ_{em} are located at red or near-infrared (NIR) regions to avoid significant tissue absorption (therefore large penetration depth) and autofluorescence (therefore small background fluorescence noise); (b) an I_{On}/I_{Off}, as large as possible, and large τ_{On}/τ_{Off} to reduce background fluorescence generated from fluorophores at the off state and increase the SNR; (c) for different future applications, T_{th} should be adjustable roughly in a range of 25°C to 42°C for both phantom (at room temperature) and *in vivo* studies (>physiological body temperature, ~37°C); (d) T_{BW} should be as narrow as possible (typically a few °C) to avoid tissue thermal damage; and (e) if possible, the fluorescence intensity at on state itself (I_{On}) and the fluorescence lifetime at on state itself (τ_{On}) should be as large as possible to increase signal strength and fluorescence emission decay time, which can help to improve SNR. In practice, if simultaneously achieving all the best values of the above parameters is difficult, parameter optimization based on specific applications should be considered.

The promising results of the USF imaging technique heavily rely on excellent and unique USF contrast agents. Therefore, synthesis of new USF contrast agents is critical for the further development of this new imaging technique. In this chapter, newly synthesized fluorophore-labeled thermosensitive polymers and nanoparticles for USF imaging are presented.

2.2 Materials and Methods

2.2.1 Materials

N-isopropylacrylamide (NIPAM), N-tert-butylacrylamide (TBAm), acrylamide (AAm), acrylic acid (AAc), allylamine (AH), N,N,N',N'-tetramethyl ethylene diamine (TEMED), ammonium persulfate (APS), N-(3-Dimethylaminopropyl)-N'-ethylcarbodiimide hydrochloride (EDC), sodium dodecyl sulfate (SDS), N,N'-methylenebisacrylamide (BIS), and 7-(2-Aminoethylamino)-N,N-dimethyl-4-benzofurazansulfonamide (DBD-ED) were purchased from Sigma-Aldrich Corporate (St. Louis, MO, USA). SeTau 425 mono-N-hydroxysuccinimide (NHS), Square 660 mono-NHS, Seta 700 mono-NHS, Seta 633 mono-NHS and Square 660 mono-NH_2 were purchased from SETA BioMedicals (Urbana, IL, USA), and denoted as ST425, Sq660, St700, Sq633, and Sq660a respectively (note that Sq660 and Sq660a have the same absorbance and fluorescence spectra/lifetime). All chemicals were used directly without further purification.

In this study, poly(N-isopropylacrylamide) (PNIPAM) is selected as the thermoresponsive polymer. Compared with other thermoresponsive polymers, (i.e., Pluronic [62] and poly-N-vinylcaprolactam, [63]), this is because: (1) it has better performance of structure change from a coil state to a globule state, (2) it has relative narrower temperature transition bandwidth (T_{BW}), (3) the methods to adjust LCST of a PNIPAM polymer have been well developed [53], [54] and the LCST can be adjusted from 20˚C to 49˚C [53], [54], [64], which is beneficial for both *in vitro* and *in vivo* studies, and (4) it can be copolymerized with other materials, including amine-containing or carboxyl-containing monomers, which enables conjugation between thermosensitive polymers and environment-sensitive fluorophores with functional groups.

Four polarity-sensitive fluorophores (DBD-ED, St633, Sq660, and St700) are either attached to PNIPAM linear polymer or encapsulated in PNIPAM nanoparticles (NPs) for investigating their fluorescence intensity and lifetime as a function of temperature. In addition, six Förster resonance energy transfer (FRET) systems (including both polymer chain and NP structures) are designed, synthesized, and characterized in which DBD-ED or ST425 is used as the donor and the Sq660(a) as the acceptor. All these dyes with the desired function groups are commercially available and are found polarity sensitive in both fluorescence intensity and lifetime.

2.2.2 USF Contrast Agents Based on Linear Thermosensitive Polymers as Fluorophore Carriers

Figure 2-1 shows the structures of the three types of fluorophore-labeled linear polymer systems, which include donor only, acceptor only, and FRET systems. In general, the thermosensitive linear polymer is first synthesized, and then fluorophores are grafted into the polymer by covalent binding (conjugation). The donor has short excitation/emission wavelengths in visible light, while the acceptor has a red emission (long wavelength). A

short wavelength excitation light (for donor) is used to excite the system, so that there is a small amount of acceptor fluoresced. When the polymer (fluorophores carrier) shrivels into the globule state, donors and acceptors get closer to each other, leading to FRET from the donor to the acceptor. Therefore, the emission of the acceptor (in long wavelength) can be observed.

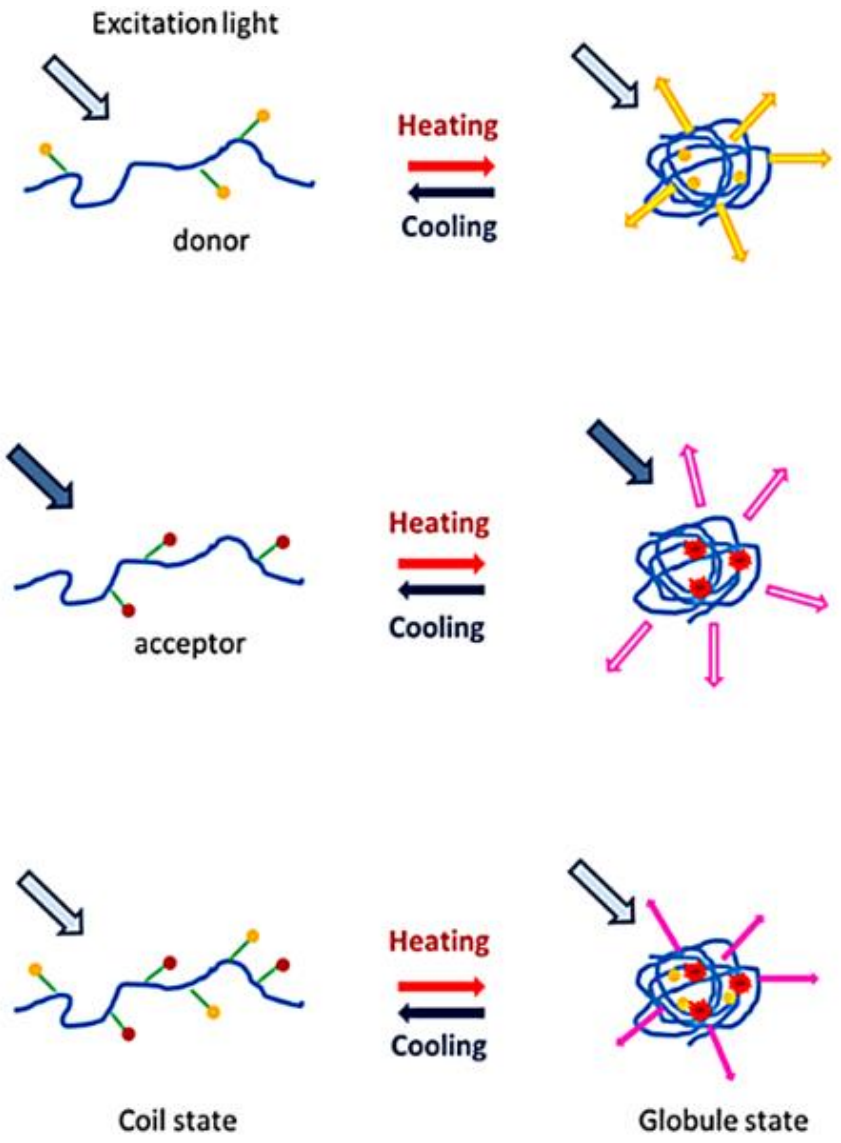

Figure 2-1 Schematic diagrams of the fluorophore-labeled linear polymer systems. From top to bottom: donor only, acceptor only, and FRET system.

2.2.2.1 Synthesis of thermosensitive linear polymers

As shown in Figure 2-2, three components of the polymer are necessarily included: (a) main thermosensitive unit, i.e., NIPAM; (b) LCST-controlling unit, i.e., TBAm or AAm; (c) functional unit, i.e., AAc or AH. AAm monomer has amine group, the activity of which, however, is quite inert in the amide form. We will discuss the functions of these three components in the following sections.

Linear polymers were synthesized through free radical polymerization. All reactions were carried out in a 250 mL Schlenk tube. The three main steps are: (1) purging procedure: The solution was first purged with nitrogen for 10 min. When adding initiator (APS)/accelerator (TEMED) into the solution, oxygen was purged out by vacuuming (1 min) and filling with nitrogen (5 s), which was repeated three times; (2) reaction conditions: 4 h with stirring at room temperature; (3) purification procedure: the sample was dialyzed with appropriate molecular weight cut-off (MWCO) membrane for three days to remove the unreacted monomers, initiator, and other small molecules. These three steps are also used in the synthesis of polymer NPs in the following sections.

Using P(NIPAM-AAc 200:1) as one example, a general procedure is described here. Samples of 1.3644 g NIPAM (monomer) and 4 μL AAc (monomer) at a molar ratio of 200:1 were dissolved with 50 mL deionized (DI) water in the tube. Along with the purging procedure, 0.067 g APS (initiator) and 51 μL TEMED (accelerator) were added into the tube. After the reaction, the sample was dialyzed with a 3.5K MWCO membrane. The resulting solution was collected and freeze-dried, which then was ready for further conjugation with amine-fluorophores. For the conjugation with NHS-fluorophores, the amine-functionalized polymer of P(NIPAM-AH) was synthesized by following the same protocol except using AH instead of AAc.

Our hypothesis is that all of the polarity-sensitive fluorophores grafted into the polymer should be embedded when the polymer shrinks (forming a hydrophobic core, low-polarity environment), by which their fluorescence intensity and lifetime would be increased to the maximum. If any fluorophores are outside of the globule, i.e., in a high-polarity environment (exposed to the solvent), no significant increase in fluorescence intensity or lifetime would be observed. An extra amount of dye is not necessary along the polymer chain, and, as a result, the ratio of dye/polymer needs to be optimized. As shown in Figure 2-2, the percentage of the functional unit in the polymer composition determined the ratio of dye/polymer in the conjugates. To investigate the effect of the amount of AAc, for instance, another two polymers with different ratios of NIPAM to AAc were synthesized by following the same protocol: P(NIPAM-AAc 100:1)and P(NIPAM-AAc 600:1). Since the ratio of the monomer(s) to the initiator remained the

same in all the three batches of P(NIPAM-AAc) polymers, the length of the three polymers were likely in close range. Therefore, the lower molar ratio of NIPAM to AAc indicated the increased conjugating sites (carboxyl from AAc) available for amine-functionalized fluorophores. The fluorescence intensity and lifetime as a function of temperature were measured for all the polymers, and other USF parameters mentioned above were also measured.

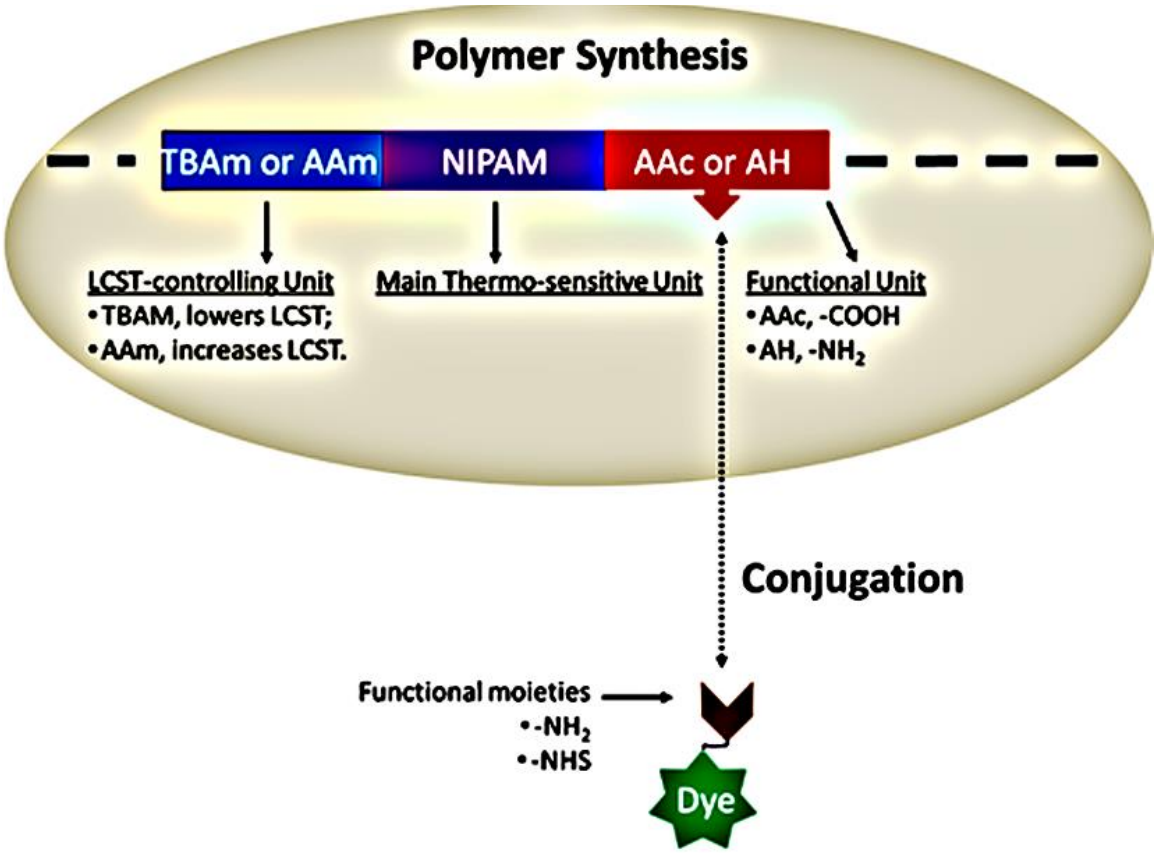

Figure 2-2 Schematic diagram of the composition of polymers in the current study. NIPAM, TBAm, AAm, AAc, H. Dyes are attached to the polymer via post-labeling conjugation.

To control the temperature threshold (LCST) of the polymers, the LCST-controlling unit AAm or TBAm was copolymerized with NIPAM. It was found that adding hydrophilic monomers (such as AAm) could increase the LCST [53], [54], [64] and adding hydrophobic monomers (such as TBAm) could decrease the LCST. More importantly, the introduction of TBAm might further improve the hydrophobicity inside the globule when the temperature >LCST, which could potentially increase the values of I_{On}/I_{Off} and τ_{On}/τ_{Off}. Therefore, the following

polymers were synthesized: P(NIPAM-TBAm-AAc 85:15:1), P(NIPAM-TBAm-AAc 185:15:1), P(NIPAM-TBAm-AAc 585:15:1), and P(NIPAM-AAm-AAc 200:32:1). The TBAm remained at 15% mole in these copolymers because we found that TBAm could be well dissolved in DI water at this ratio.

2.2.2.2 Conjugation of fluorophores on the polymers

After the synthesis of polymers, the conjugation (post-labeling) between the polymer and fluorophores is based on the chemical reaction between carboxyl and primary amine (Figure 2-2). The fluorophores used in this study can be divided into two groups based on the functional groups. The first type is fluorophore with NHS, which is an activated carboxyl group and can directly react with primary amine (NH_2). The corresponding thermosensitive polymer is synthesized with amine-containing monomers (such as AH) to form P(NIPAM-AH). The second type is fluorophore with primary amine that can conjugate with carboxyl in the presence of the condenser EDC. The corresponding thermosensitive polymer is synthesized with carboxyl-containing monomers (such as AAc) to yield P(NIPAM-AAc).

The conjugating reaction was carried on in a 7 mL brown glass tube for protecting light-sensitive dyes. The general procedures for conjugation are: (A) As for amine-containing dyes, i.e., DBD-ED or Sq660a, 5 mg polymer, 25 mg EDC (condenser), and 0.3 mg DBD-ED or/and 5 μL Sq660a (stock solution:1 mg/100 μL DMSO: dimethyl sulfoxide) were dissolved in 5 mL DI water in the tube. Then the tube was stirred and reacted overnight at room temperature. After reaction, the conjugates were purified with appropriate MWCO dialysis membrane as described earlier. (B) As for NHS-dyes, i.e., ST425, St633, Sq660, and St700, 5 mg polymer, and 10 μL dye (stock solution: 1 mg/100 μL DMSO) were dissolved in 5 mL PBS (8 mM sodium phosphate, 2 mM potassium phosphate, 0.14 M NaCl, 10 mM KCl, pH 8.3~8.6). Then, the solution was stirred and reacted overnight at room temperature. After that, 1 mL of 20 mM Tris buffer (pH 7.8) was added into the solution to quench the unreacted NHS moieties of the dye for two hours. Finally, the sample was dialyzed for purification. The similar procedures were also performed in the conjugation between polymer NPs and dyes in the following sections.

It is necessary to point out that the procedures of the conjugation between DBD-ED and polymers in the current study are different from those described previously [39], [52]. In [39], [52], DBD was first chemically reacted with a monomer of acrylic acid (AAc) to form DBD-AAc. Then the DBD-AAc was copolymerized with NIPAM. In the current study, the P(NIPAM-AAc) copolymer was first synthesized, then the amine-containing DBD-ED (commercially available) was conjugated on the carboxyl-containing copolymer (on AAc). The benefits of such post-

labeling strategy in the current procedures include: (1) all chemical components are commercially available and no chemical synthesis at the level of small molecules is needed; (2) the unattached DBD-ED molecules (small molecular weight) can be easily separated from the conjugated polymers (large molecular weight) via a dialysis method with an appropriate MWCO membrane (commercially available). Nevertheless, the procedure in [39], [52] requires a complicated method to separate DBD (a small molecule) from DBD-AA (another small molecule). More interestingly, the polymers synthesized from current protocol show higher values of the ratios of I_{On}/I_{Off} and τ_{On}/τ_{Off} compared with the polymers synthesized from the protocol in [39], [52], but at the expense of the slight increase in the transition bandwidth T_{BW}.

2.2.3 USF Contrast Agents Based on Thermosensitive NPs as Fluorophore Carriers

Instead of linear polymer, PNIPAM-based NPs were used as fluorophores carriers in this section. Fluorophores are either encapsulated inside the NPs [Figure 2-3(a)] or attached on the surface of NPs [Figure 2-3(b)]. As for encapsulation, the synthesis was referred to the protocol in our previous work in which no chemical modification was needed in the dye molecule [45]. The attachment on the NPs' surface was also based on the conjugation between amine and carboxyl (like the conjugation for linear polymers).

2.2.3.1 Encapsulation of fluorophores into NPs

The protocol from our previous method was used [45]. To form polymer NPs, a cross-linker (BIS, 0.0131 g) and a surfactant (SDS, 0.0219 g) were added into the reaction solution. Other reagents are the same as that in the synthesis of linear polymer. No chemical modification at the dye molecule was needed. 1 mg DBD-ED or 10 μL dye-NHS (1 mg/100 μL DMSO) was added prior to polymerization.

Three types of dye-encapsulated NPs were synthesized: (1) dye@P(NIPAM-TBAm 185:15) NPs, (2) dye@PNIPAM NPs, and (3) dye@P(NIPAM-AAm 86:14) NPs. The symbol of @ means the dyes are inside the NPs. The measured LCSTs are 31, 35, and 42˚C, respectively.

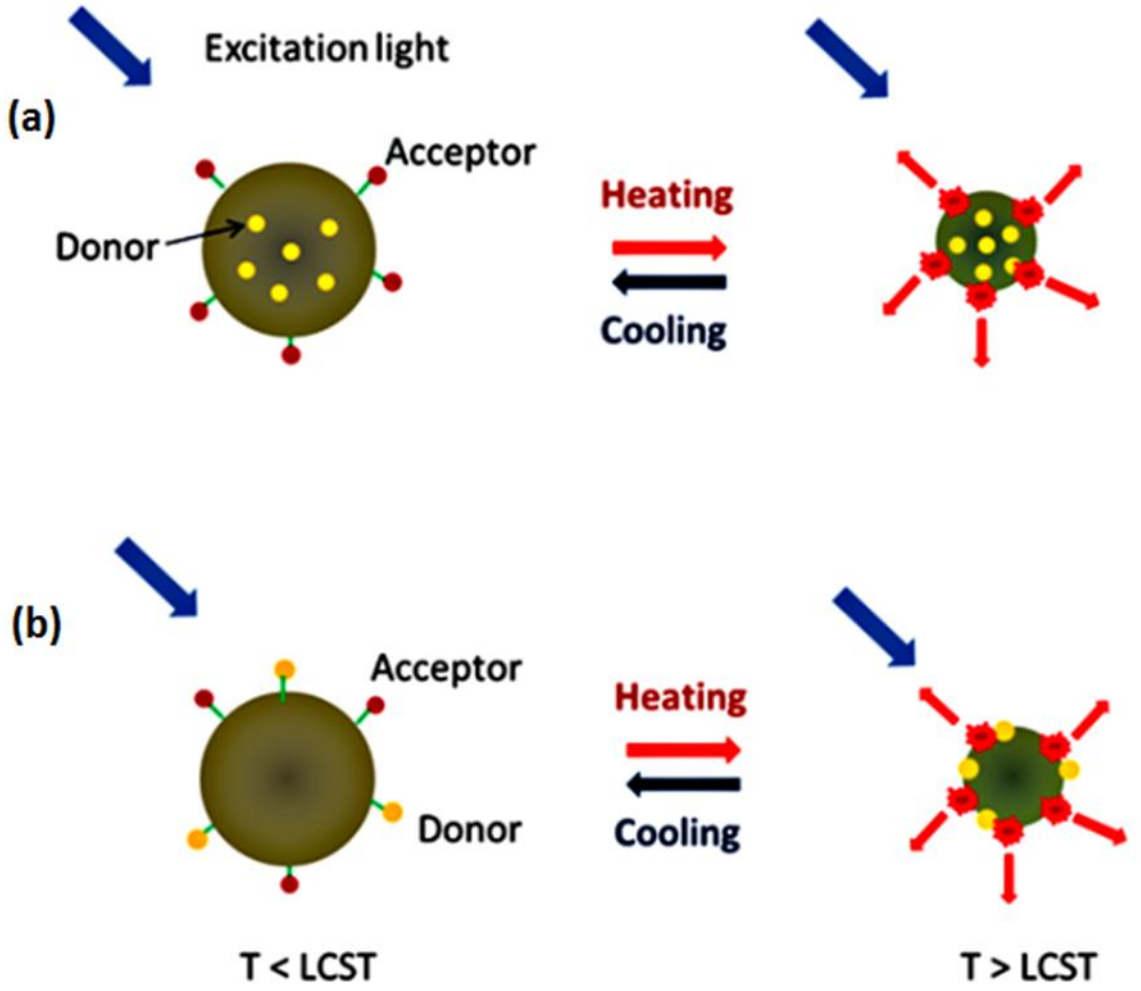

Figure 2-3 Schematic diagrams of the FRET systems based on (a) fluorophore-encapsulated NPs and (b) fluorophore-attached NPs.

2.2.3.2 Conjugation of fluorophores on the surface of NPs

The conjugation procedure is the same as that for linear polymers. The only difference was the use of 5 mL polymer NPs solution or dye-encapsulated polymer NPs solution, rather than using 5 mg linear polymer. Two formats are listed as follows:

I. Donors @NPs~acceptors format, as shown in Figure 2-3(a). The donors are encapsulated inside the NPs, after which the acceptors are grafted onto the surface. For instance, DBD-ED@P(NIPAM-AH 86:14)NPs~Sq660. DBD-ED was encapsulated inside the P(NIPAM-AH 86:14) NPs, and Sq660 was introduced on the surface via NHS (from the dye) and amine (from AH) conjugation. We define this as Protocol I.

II. NPs~donors~acceptors format, as shown in Figure 2-3(b). Both donors and acceptors are grafted onto the surface of the polymer NPs. For instance, P(NIPAM-AAc 200:1)NPs~DBD-ED~Sq660a. Two dyes were covalently binded to the surface via the conjugation between amine (from dyes) and carboxyl (from AAc). We define this as Protocol II.

2.2.4 Fluorescence Intensity and Lifetime Measurement

A fluorescence intensity and lifetime measurement system was developed to characterize the synthesized USF contrast agents. Briefly, Figure 2-4 shows the major components including a subnanosecond pulse nitrogen laser (800 ps pulse width, nitrogen laser: OL-4300, dye laser: OL-401, Optical Building Blocks Corporation, Birmingham, NJ), a pulse delay generator (PDG, DG645, Stanford Research Systems, CA), a temperature controller (PTC10, Stanford Research System, Sunnyvale, CA), a photomultiplier tube (PMT, H10721-20, Hamamatsu, Japan), an amplifier (C5594, Hamamatsu, Japan) and a multichannel GHz oscilloscope (DPO 7254, Tektronix, OR). The dye laser is pumped by nitrogen laser illuminated excitation pulses with a pulse width of ~800 ps. The pulse energy was adjusted by a rotational neutral density filter and measured by a pulse energy meter system (Labmax-Top laser power/energy meter, Santa Clara, CA). The excitation wavelength was selected as 470 or 609 nm. The former was adopted as the excitation wavelength for the DBD-ED and the FRET systems. The latter was adopted as the excitation wavelength for the square dyes. For DBD-ED samples, a 561 nm long-pass filter was used as the emission filter to reject excitation photons. For red dye samples and the FRET systems, a bandpass filter with a central wavelength of 711 nm and a bandwidth of 25 nm was used as the emission filter, except for using 650/60 nm bandpass filter for the St633 dye.

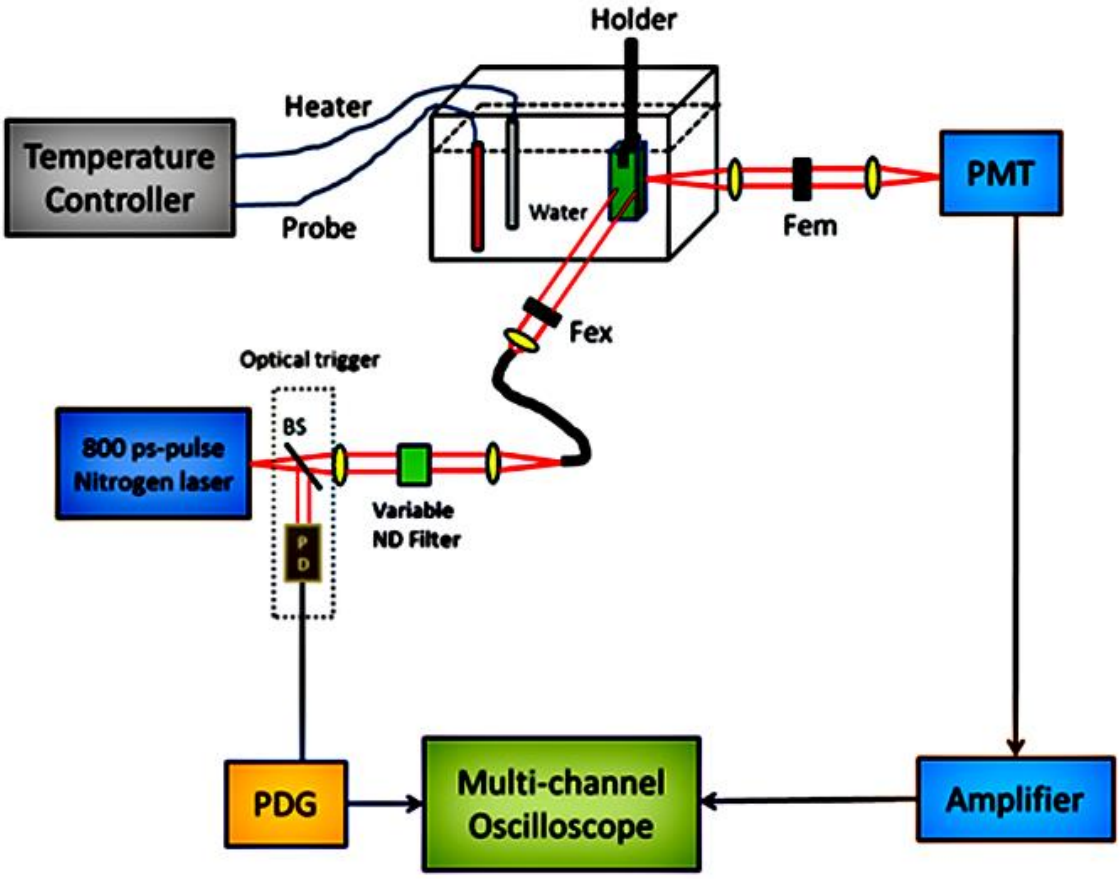

Figure 2-4 Fluorescence intensity and lifetime measurement system. PDG: pulse delay generator. PMT: photomultiplier tube. BS: beam splitter. PD: photodiode. ND Filter: neutral density filter.

To accurately synchronize the laser pulse, fluorescence signal, and data acquisition, the following strategies were adopted. The laser pulse was delayed ~100 ns by coupling the laser beam into a 20 m optical fiber (FT200EMT, Thorlabs Inc., Newton, NJ). When an excitation light pulse was fired by the laser, a small amount of laser energy was split by a beam splitter and was delivered to a fast photodiode (PD) to generate an electronic pulse. This pulse was used to trigger the PDG. The output of the PDG was used to trigger the oscilloscope for data acquisition. The triggering time was adjusted by controlling the output delay time of the PDG. Thus, the data acquisition of the oscilloscope was well synchronized and matched with the fluorescence signal. Our experimental data showed that the 100 ns delay from the laser pulse was large enough to account for the total electronic delay of the trigger signal.

The sample was placed in a quartz cuvette (Starna Cells, Atascadero, CA) that was submerged in a transparent water tank. The temperature of the water bath was controlled by the temperature controller with a heater and a

temperature feedback probe. The fluorescence signal was averaged 100 times and the averaged data was fit to a single exponential decay function to calculate the fluorescence lifetime. The peak fluorescence intensity of the emission decay curve was adopted to calculate the intensity related parameters.

2.3 Results

As mentioned previously, five parameters are used to evaluate the performance of a USF contrast agent: λ_{ex} and λ_{em}, I_{On}/I_{Off}, τ_{On}/τ_{Off}, T_{th}, and T_{BW}. We summarize the performance of all the USF contrast agents developed in this work in Table 2-1 (linear polymers-based) and Table 2-2 (NPs-based). Conjugates of polymer/dyes are classified into three groups: donor only, acceptor only, and FRET system (donor and acceptor). The ideal contrast agent for deep tissue imaging would be of large λ_{ex} and λ_{em}, I_{On}/I_{Off}, and τ_{On}/τ_{Off} and τ_{On}, but narrow T_{BW}, along with appropriate T_{th}.

Table 2-1 Overview of USF contrast agents based on linear polymers

		λ_{ex} &λ_{em} (nm)	I_{On}/I_{Off}	τ_{On}/τ_{Off} &τ_{On} (ns)	T_{th} (° C)	T_{BW} (° C)	Reference	Label No.
DBD (donor)	PNIPAM (chain), co-polymerization	470 & 580	4.2	~3.5 &~14	31	~1	[39]	1.1
	P(NIPAM-AAc 100:1), post-labeling	470 &560lp	~1.4	~4.7 & ~4.8	35	~8	This work	1.2
	P(NIPAM-AAc 200:1), post-labeling	470 &560lp	~1.6	~3.1 & ~5.2	36	~5	This work	1.3
	P(NIPAM-AAc 600:1), post-labeling	470 &560lp	~1.6	~1.9 & ~2.5	32	~5	This work	1.4
	P(NIPAM-TBAm-AAc 185:15:1), post-labeling	470 &560lp	~1.8	~5.4 & ~10	26	~4	This work	1.5
	P(NIPAM-AAm-AAc 200:32:1), post-labeling	470 &560lp	~1.1	~2 & ~2.2	42	~9	This work	1.6
Red dyes (acceptor)	P(NIPAM-AH 200:1), post-labeling, St633	609&650/60	~4.2	~1.1 & ~0.9	32	~5	This work	2.1
	P(NIPAM-AH 200:1), post-labeling, Sq660	609&711/25	~1.6	~2.2 & ~2.1	35	~3	This work	2.2
	P(NIPAM-AH 200:1), post-labeling, St700	609&711/25	~0.6	~0.7 &~1.1	33	~8	This work	/
FRET	P(NIPAM-AAc 200:1), ~DBD-ED, ~Sq660a, post-labeling	470&711/25	~3.8	& ~3.4 ~5.3	34	~3	This work	3.1
	P(NIPAM-TBAm-AAc 185:15:1), ~DBD-ED, ~Sq660a, post-labeling,	470&711/25	~3	~1.7 & ~5.3	26	~3	This work	3.2

Table 2-2 Overview of USF contrast agents based on polymer NPs

		λ_{ex} & λ_{em} (nm)	I_{On}/I_{Off}	τ_{On}/τ_{Off} & τ_{On} (ns)	T_{th} (°C)	T_{BW} (°C)	Reference	Label No.
DBD (donor)	@PNIPAM NPs, encapsulated	470 & 560lp	~4	~3.3 & ~6	35	~5	This work	4.1
	@P(NIPAM-AAm 86:14) NPs, encapsulated	470 & 560lp	~3.5	~2.2 & ~3.8	42	~9	This work	4.2
	@P(NIPAM-TBAm 185:15) NPs, encapsulated	470 & 560lp	~3.7	~3.6 & ~7.2	31	~5	This work	4.3
	@P(NIPAM-AH 86:14) NPs, encapsulated	470 & 560lp	~3	~2.6 & ~5.3	33	~8	This work	4.4
Red dyes (acceptor)	@PNIPAM NPs, encapsulated, St700	630 & 711/25	~0.7	~0.7 & ~1.2	36	~9	This work	5.1
	@PNIPAM NPs, encapsulated, Sq660	609 & 711/25	~3.3	~1.3 & ~2.9	35	~5	This work	5.2
FRET	DBD-ED@ P(NIPAM-AH 86:14) NPs~Sq660	470 & 711/25	~6.9	~1.4 & ~3.42	35	~7	This work	6.1
	P(NIPAM-AAc 200:1) NPs~DBD-ED~Sq660a	470 & 711/25	~5.3	~3.3 & ~6	35	~5	This work	6.2
	P(NIPAM-TBAm-AAc 185:15:1) NPs~DBD-ED~Sq660a	470 & 711/25	~6.5	~2.7 & ~5.2	33	~9	This work	6.3
	P(NIPAM-AAc 200:1) NPs~ST425~Sq660a	456 & 711/25	~7	~1.5 & ~3.65	36	~4	This work	6.4

2.3.1 USF Contrast Agents Based on Linear Thermosensitive Polymer as Fluorophore Carriers

2.3.1.1 DBD-ED (donor)-labeled linear thermosensitive polymer

Although the λ_{ex} and λ_{em} are located at a visible wavelength range, the DBD dye has shown long fluorescence lifetime (τ_{On}) when the temperature is above the temperature threshold (T_{th}), i.e., 14 ns, whereas it has a short τ_{Off} (~4 ns) when the temperature is below T_{th} [39], [52]. Thus, the large value of τ_{On}/τ_{Off} makes this dye attractive in USF imaging because the background fluorescence noise can be potentially suppressed by using a time-gating detection method [39]. Accordingly, this unique property motivates us to investigate this type of dye as candidates for synthesizing USF contrast agents.

A unique property of USF contrast agents is the switching-like fluorescence response to temperature. Figure 2-5 shows this switching property in which the fluorescence intensity and lifetime are plotted as a function of temperature. The three systems have similar polymer, P(NIPAM-AAc 200:1) or P(NIPAM-AH 200:1), but different

dyes: (A) DBD-ED, (B) Sq660, and (C) DBD-ED, and Sq660a (note that Sq660 and Sq660a have the same absorbance and fluorescence spectra/lifetime). As an example, Figure 2-5(a) demonstrates how the above-mentioned five parameters are defined based on the fluorescence lifetime change (blue solid curve with filled triangles) and fluorescence intensity change (blue dashed curve with blank triangles). In this case, DBD-ED was grafted onto the linear thermosensitive polymer P(NIPAM-AAc 200:1) via post-synthesis conjugation. The fluorescence lifetime of DBD-ED fluctuates between ~1.34 to ~2.0 ns (mean value 1.67 ns) when the temperature is below LCST of the polymer. It increases sharply at ~35°C, and then saturates at 5.2 ns (mean value) when temperature is above 40°C. Therefore, the lifetime ratio τ_{On}/τ_{Off} can be calculated as ~3.1 (5.2/1.67) (marked by green dashed lines). T_{th} and T_{BW} can be found as ~35 °C (pointed out by the black solid arrow) and ~5°C (35–40, light-blue round dot lines) respectively. Similarly, I_{On}/I_{Off} can be calculated as ~1.6 (0.66/0.42) (see the pink dash dot lines). Similar parameters for the other two systems can be found in Table 2-1 (see the label 2.2 and 3.1). The signal induced by ambient temperature fluctuation was found negligible.

It can be seen in Figure 2-2 that AAc provides the binding site for DBD-ED. Thus, the AAc content in the co-polymer P(NIPAM-AAc) will potentially determine the amount of DBD-ED in the final conjugate product. Assuming NIPAM-to-AAc is at a perfect molar ratio and the conjugation efficiency is also adequately high, the resulted DBD-labeled conjugation would show comparable performance to that prepared through DBD-AAc copolymerization in our previous report [39]. Three sets of experiments including ratios of NIPAM/AAc at 100:1, 200:1, and 600:1 were investigated, and the results are shown in Table 2-1 **(**label No.1.2-1.4**).** P(NIPAM-AAc 100:1)~DBD-ED shows the highest values of τ_{On}/τ_{Off}, which is ~4.7. The fluorescence lifetime ratio τ_{On}/τ_{Off} is higher than that in the previous report (3.5); however, the I_{On}/I_{Off} (1.4) and τ_{On} (4.8 ns) are about three-fold smaller than those in the previous report [39] and T_{BW} (~8 °C) is wider. By fixing the ratio of NIPAM/AAc at 200:1, τ_{On}/τ_{Off}, I_{On}/I_{Off} and τ_{On} can be further improved to be 5.4, 1.8, and 10 ns by copolymerization with TBAm (with a molar ratio of TBAm-to-NIPAM at 15:185), a monomer that is of higher hydrophobicity than NIPAM (see No. 1.5 in Table 2-1). A great diversity of T_{th} was accomplished by adjusting the ratio of LCST-controlling unit (TBAm-to-NIPAM = 85:185; AAm-to-NIPAM = 32: 200), which had also been demonstrated in Table 2-1 (label No. 1.5 & 1.6).This will allow us to target a board range of applications (such as from phantom test to *in vivo* animal studies) in future work.

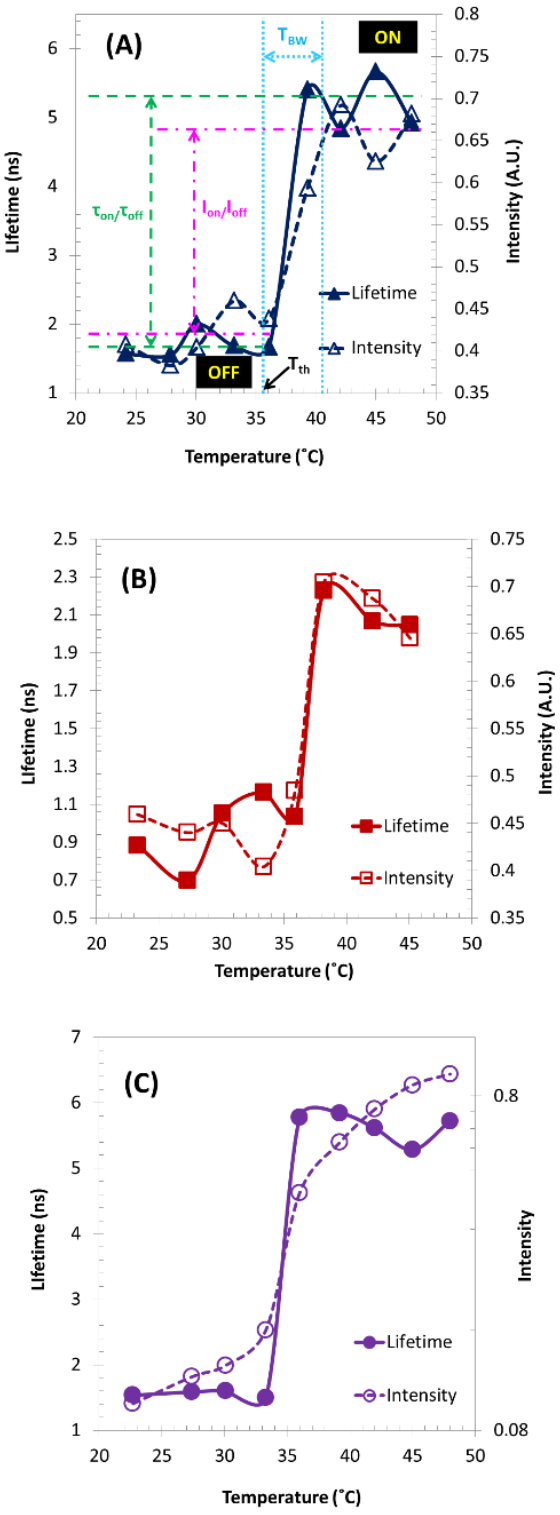

Figure 2-5 Fluorescence lifetime and intensity changes as a function of temperature of linear thermosensitive polymer-based USF contrast agent. (a) Polymer labeled with DBD-ED alone, (b) Sq660 alone, and (c) DBD-ED and Sq660a for FRET study. Excitation wavelength: (a, c) 470 nm; (b) 609 nm. Emission detection filter: (a) 561 nm

long-pass filter; (b, c) 711/25 nm band-pass filter. For (a and c): P(NIPAM-AAc 200:1); for (b): P(NIPAM-AH 200:1).

2.3.1.2 Red dye (acceptor) labeled linear thermosensitive polymer

Red or NIR dyes are more intriguing for deep tissue imaging applications because of the less tissue absorption and autofluorescence emission. Red polarity-sensitive dyes were attached to the linear thermosensitive polymer, and the conjugates' fluorescence responses toward temperature increase were investigated (see the labels of No.2.1-2.2 in Table 2-1 for detailed results). St633 shows an excellent I_{On}/I_{Off} (4.3), but the τ_{On}/τ_{Off} was found barely increased. Sq660 has a good τ_{On}/τ_{Off} (2.2), and the I_{On}/I_{Off} is also acceptable (1.6), as shown in Figure 2-5(b).

2.3.1.3 Linear-polymer-based FRET systems

Ideally, to achieve high SNR, large values of both I_{On}/I_{Off} and τ_{On}/τ_{Off} are preferred. While fluorophore-labeled thermosensitive polymers show good switching effect via the significant change in the polarity microenvironment, Förster resonance energy transfer (FRET) can be considered as the second switching mechanism. If polarity sensitive dyes can be used as either donors or acceptors or both, the combination of the two switching mechanisms (polarity change and FRET efficiency change between T<LCST and T>LCST) may enhance the switching efficiency and the two ratios. The hypothesis is that, when T<LCST, the FRET between donors and acceptors is weak because both are at the off state and the average donor-acceptor distance is relatively large. When the T>LCST, the FRET becomes strong because both are at the on state and the average donor-acceptor distance is significantly reduced. Another benefit is that FRET makes the lifetime signal detected from the acceptors much longer than the signal when no FRET occurs because the lifetime of the FRET signal is determined by the longer lifetime between the donor and acceptor.

Figure 2-5(c) shows the fluorescence lifetime and intensity changes of Sq660a in the FRET system as a function of temperature, which is obtained by using 470 nm as the excitation wavelength and a 711/25 nm bandpass filter for emission detection. The lifetime of Sq660a in the FRET system of P(NIPAM-AAc 200:1)~DBD-ED~Sq660a was found to increase when temperature reaches 34°C (purple solid line with filled circles). The saturated lifetime was found to be ~5.3 ns (T=36°C), whereas the maximum lifetime of Sq660a alone is only 2.1 ns (consistent with the result of testing pure Sq660a dye in low polarity solvent, e.g., 1,4-dioxane). This result strongly indicates that FRET does happen between DBD-ED and Sq660a when T>LCST. Also, the combination of the two switching mechanisms

(polarity change and FRET efficiency change) leads to improvement at τ_{On}/τ_{Off} (~3.4) and I_{On}/I_{Off} (~3.8), compared with the results of Sq660 alone [2.2 and 1.6 in Figure 2-5(b)].

2.3.2 USF Contrast Agents Based on Thermosensitive NPs as Fluorophore Carriers

2.3.2.1 DBD-ED (donor)-encapsulated thermosensitive NPs

The dye was encapsulated into thermosensitive NPs by following the similar steps as described in our previous work [45]. No functional unit in polymer composition and no conjugation are needed. The size of the NPs is about ~120 nm ± 40 nm [45]. Similarly, Figure 2-6(a) shows the switching-like fluorescence response of DBD-ED@PNIPAM NPs. τ_{On}/τ_{Off} is ~3.3 and τ_{On} is ~6 ns. More importantly, I_{On}/I_{Off} was estimated to be ~4, which is the highest I_{On}/I_{Off} ratios among linear polymer-based contrast agents (Table 2-1).

Interestingly, DBD-ED@P(NIPAM-AAm 86:14) NPs (No. 4.2 in Table 2-2**)** shows an improved performance in comparison with P(NIPAM-AAm-AAc 200:32:1)~DBD-ED (No. 1.6 in Table 2-1). The underlying mechanisms are still being investigated. The T_{th} is slightly above 37°C and can be further adjusted by controlling the NIPAM-to-AAm ratio.

2.3.2.2 Red dye (acceptor)-encapsulated thermosensitive NPs

Sq660 was encapsulated inside thermosensitive NPs, and the resulting product Sq660@PNIPAM NPs were tested [Figure 2-6(b)]. The I_{On}/I_{Off} ratio was estimated to be ~3.3, which is two-fold larger than that with linear polymer format (~1.6). Although τ_{On}/τ_{Off} is limited at ~1.3, the lifetime versus temperature curve maintains excellent switching-like shape. The temperature threshold is 35 °C and the temperature transition bandwidth is around 5 °C. Compared with linear polymer format, its NP format shows a better match between the lifetime and intensity change.

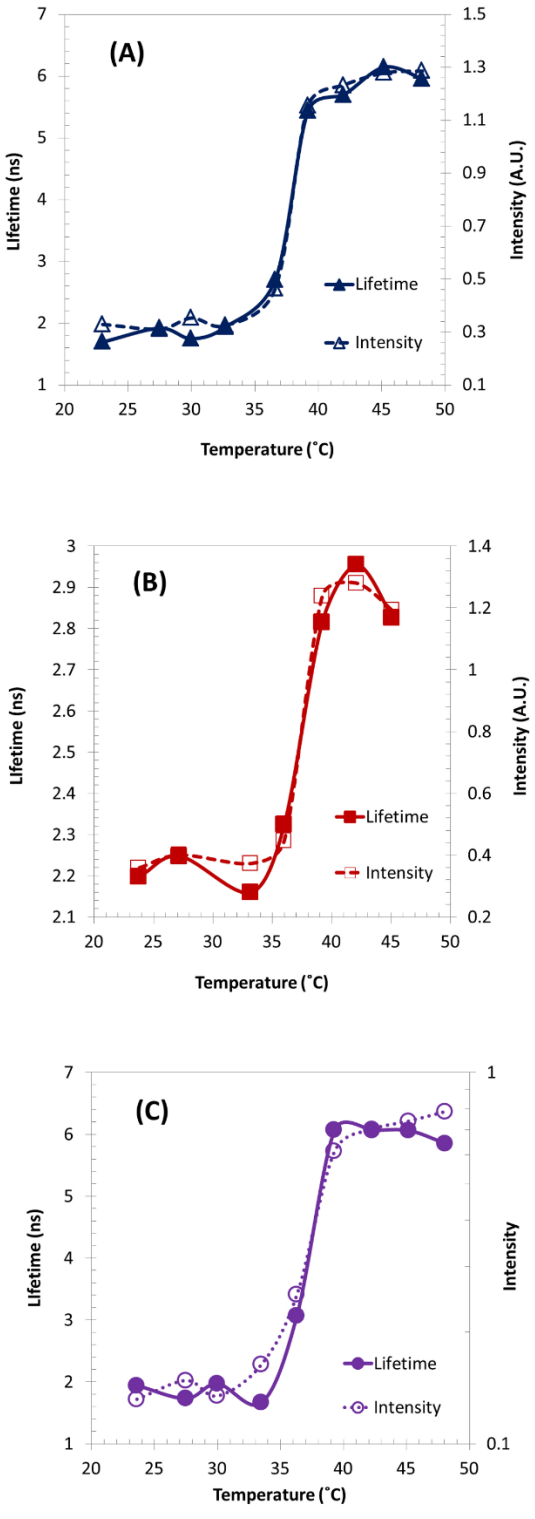

Figure 2-6 Fluorescence lifetime and intensity changes as a function of temperature of thermosensitive NPs-based USF contrast agent. (a) DBD-ED@PNIPAM NPs, (b) Sq660@PNIPAM NPs, and (c) P(NIPAM-AAc 200:1)~DBD-

ED~Sq660a NPs for FRET studies. Excitation wavelength: (a, c) 470 nm, (b) 609 nm. Emission detection filter: (a) 561 nm long-pass filter, (b, c) 711/25 nm bandpass filter.

2.3.2.3 Nanoparticle-based FRET systems

I. Protocol I, donors@NPs~acceptors

Measuring at 711/25 nm, the τ_{On} value of Sq660 in the FRET system DBD-ED@P(NIPAM-AH 86:14)~Sq660 was found to be ~3.4 ns (No. 6.1 in Table 2-2), which is larger than the longest lifetime of Sq660 when in hydrophobic conditions (~2.1 ns). This confirms the FRET occurrence between encapsulated DBD-ED and surface-grafted Sq660. The I_{On}/I_{Off} ratio (~6.9) is one of the highest in the present work, which is two-fold higher than that of linear polymer format [Figure 2-5(c)]. To improve τ_{On}/τ_{Off} (1.4) and τ_{On}, a new design for an NPs-based FRET system was carried out and denoted as Protocol II.

II. Protocol II, NPs~donors~acceptors

In this protocol, the donors and acceptors were conjugated simultaneously on the surface of NPs. The fluorescence lifetime and intensity changes of Sq660a in the FRET system, as function of temperature, were measured, as shown in Figure 2-6(c). The τ_{On} and τ_{On}/τ_{Off} are ~6 ns and ~3.3, which are markedly improved compared with that in Protocol I (~3.4 ns and ~1.4). Taken together, one can deduce that this type of NPs-based FRET system's performance is better than that used for linear polymer, see No. 3.1 in Table 2-1 and No. 6.2 in Table 2-2.

2.4 Discussion

2.4.1 Linear Polymer-Based USF Contrast Agents

As mentioned above, the synthesis protocol of DBD-conjugated thermosensitive polymers in this study is different from the one used in [39], [52]. We named our current method post-synthesis conjugation, while the method in previous reports was named DBD-AAc copolymerization. The current method is of great advantage in the convenience of synthesis and purification. The difference in I_{On}/I_{Off} and τ_{On}/τ_{Off} between the two synthesis methods, the green squares (1.2–1.6) and the brown star (1.1) in Figure 2-7, can be attributed to the low efficiency of post-synthesis conjugation. Some functional units (AAc) along the chain might be blocked by the random coils [65] formed by hydrophobic moieties in the polymer, i.e., isopropyl side group of NIPAM. These functional units seem the perfect sites for locating DBD-ED (because of high hydrophobicity environment), but unfortunately, are not completely available for the post-synthesis conjugation. Thus, the two ratios (I_{On}/I_{Off} and τ_{On}/τ_{Off}) are limited in a certain range.

When TBAm was introduced into the polymer through copolymerization, the τ_{On}/τ_{Off} (5.4) is higher than that in previous report (3.5). It has a relatively broader T_{BW} (4°C), which is in an acceptable range for USF imaging.

Three red or NIR polarity-sensitive dyes, St633, Sq660, and St700, were investigated. One of the most important advantages is that tissue autofluorescence and absorption are significantly suppressed at red or NIR light. Among them, Sq660 shows acceptable I_{On}/I_{Off} and τ_{On}/τ_{Off} ratios (the blue star with No. 2.2 in Figure 2-7). Although St700 is a polarity sensitive dye, the conjugate with a linear polymer shows a negatively-switching performance (I_{On}/I_{Off} and τ_{On}/τ_{Off} ratios drop as temperature increases, No. 5.1 in Figure 2-7). The mechanism is unclear.

The I_{On}/I_{Off} ratio is generally below 2 when the polymer is labeled with donor/or acceptor alone, whereas the τ_{On}/τ_{Off} ratio for acceptor alone (Sq660) is smaller than 2.5. These two ratios were improved in the FRET system, where τ_{On}/τ_{Off} =3.4 and I_{On}/I_{Off}=3.8. Also, the τ_{On} reaches 5.3 ns, which is two-fold larger than the maximum lifetime of Sq660 itself. The long fluorescence decay time can further be used to reduce the background noise from autofluorescence (generally < 4 ns). The trade-off is that the FRET system needs a short wavelength to excite the sample (470 nm). With the help of the time-gating method [39], such a FRET system would be potentially applicable in surface tissue bioimaging.

2.4.2 NPs-based USF Contrast Agents

It is apparent that NPs-based contrast agents listed in Table 2-2 have higher I_{On}/I_{Off} ratios (>3) than those using linear polymers (Table 2-1). Herein, the problem of low efficiency in conjugation does not exist, since fluorophores are directly encapsulated into the NPs. It is possible that the ratio of fluorophores/monomer is higher in NPs format than linear polymer format, leading to increase in I_{On}/I_{Off}. On the other hand, τ_{On}/τ_{Off} is slightly smaller in NPs format, likely due to the self-quenching between fluorophores inside NPs.

As fluorophores are attached on the surface of NPs for FRET study, the dropping of τ_{On}/τ_{Off} by self-quenching is much less. For example, when both of DBD-ED and Sq660a were immobilized on the surface of NPs, the τ_{On}/τ_{Off} is 3.3 (No. 6.2 in Figure 2-7); however, when DBD-ED was encapsulated inside the NPs, but Sq660 was immobilized on the surface, the τ_{On}/τ_{Off} is 1.4 (No. 6.1 in Figure 2-7). Like linear polymer-based format (see No. 3.1 and No. 3.2 in Figure 2-7), the introduction of hydrophobic TBAm monomer in the FRET system is not beneficial in improving the two ratios (see No. 6.2 and No. 6.3 in Figure 2-7).

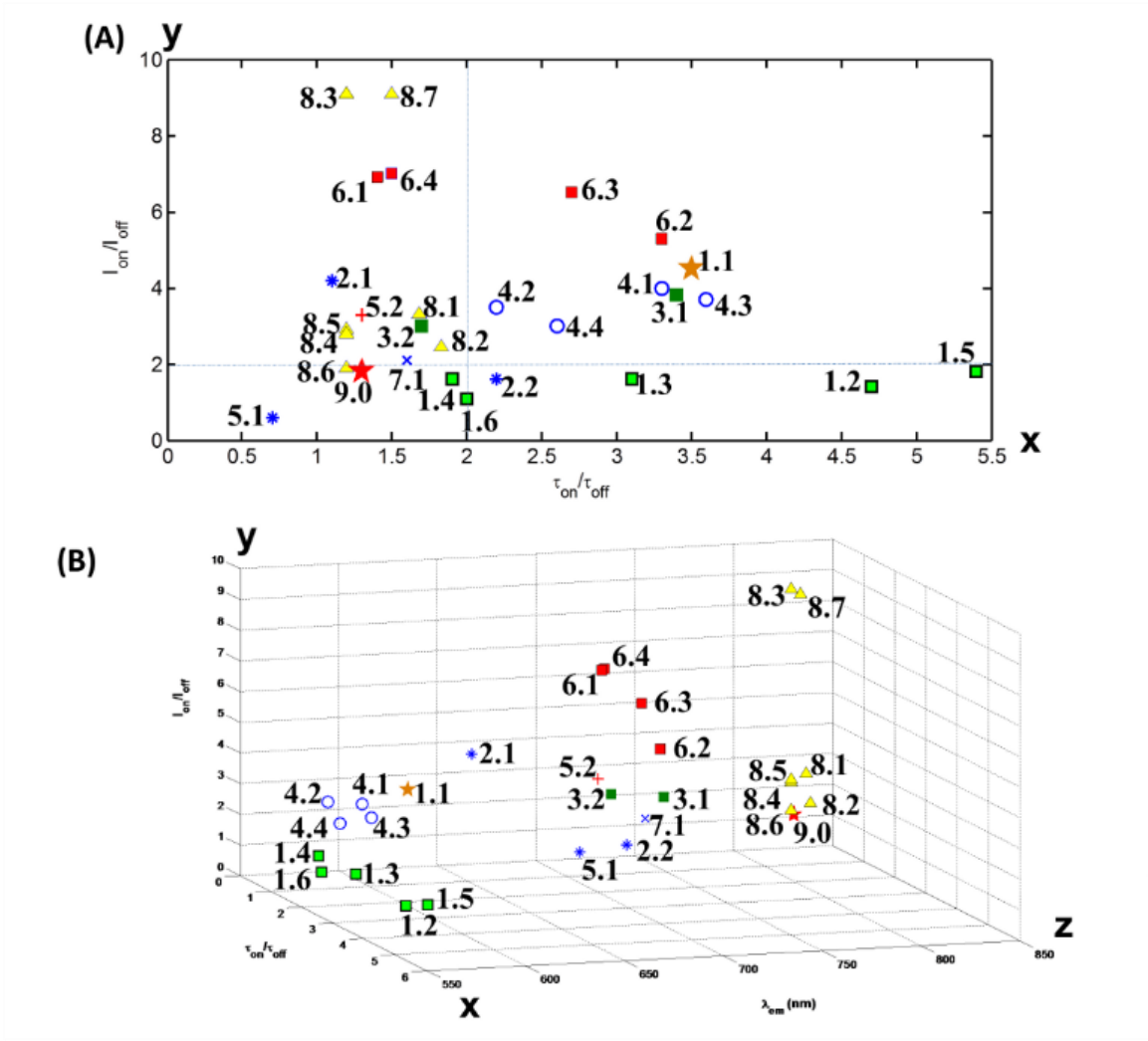

Figure 2-7 (A) Overview of the performance, i.e., fluorescence lifetime ratios and intensity ratios, as well as (B) emission wavelength of all thermoresponsive fluorescence contrast agents in our studies and related literatures. The number labeled on each point can be referred to Table 2-1 and Table 2-2 (from 1.1 to 6.4). Labels from 7.1 to 9.0 are data points cited in our previous works [45], which includes: (7.1) DL700@P(NIPAM-AAc 200:1) NPs; (8.1 and 8.2) ICG@PNIPAM NPs; (8.3 and 8.4) ICG@P(NIPAM-AAm 86:14) NPs; (8.5 and 8.6) ICG@P(NIPAM-TBAm 185:15) NPs; (8.7) ICG@P(NIPAM-AAm 90:10) NPs; (9.0) ICG@Pluronic micelle. Data points (1.1) and (9.0) are adopted from [52] and [61].

2.4.3 Overview of USF-Qualified Contrast Agents

We summarized all contrast agents developed in this chapter in Figure 2-7 based on I_{on}/I_{off} and τ_{on}/τ_{off} [and λ_{em} in Figure 2-7(B)]. For comparison, our recently developed ICG-based USF contrast agents (No. 8.1-8.7 in Figure 2-7) and two other contrast agents from other groups (No. 1.1 and 9.0 in Figure 2-7) [52], [61] were included. If we divide Figure 2-7(A) into four areas by crosslines (x=2, y=2; blue dashed lines), the samples in the top right area are good candidates for USF imaging because both two ratios are high. The samples in the top left area have high I_{on}/I_{off} and low τ_{on}/τ_{off}. Therefore, the time-gating method may be relatively less efficient due to the low τ_{on}/τ_{off} value. Thus, the USF detection method will be mainly based on fluorescence intensity change of the USF contrast agents [45], [46]. The samples in the bottom right area have high τ_{on}/τ_{off} and low $I_{on}/I_{off..}$ Thus, the time-gating USF detection method used in [39] should be adopted for significantly attenuating background noise. The samples in the bottom left area have lower values for both ratios. Thus, they are relatively less efficient or not suitable (No. 5.1 in the Figure 2-7) for USF imaging. We tested the reversibility of our contrast agents at several heating/cooling cycles, i.e., room temperature and 41°C (data not shown). No significant loss in florescence intensity and lifetime was observed for six cycles.

2.5 Conclusion

In this study, USF contrast agents were synthesized by using environment-sensitive fluorophores and thermosensitive polymers or NPs. These contrast agents in blue or red range show acceptable lifetime on-to-off ratio (τ_{on}/τ_{off}), acceptable intensity on-to-off ratio (I_{on}/I_{off}), narrow temperature transition bandwidth (T_{BW}), and adjustable temperature threshold (T_{th}). Six FRET systems, where both donor (DBD-ED or ST425) and acceptor (Sq660) are environment-sensitive, were reported in the present work in which the τ_{on}/τ_{off} and I_{on}/I_{off} of Sq660 were significantly improved in comparison with that of Sq660 alone. The present work offers a series of potentially applicable contrast agents for future tissue imaging by using USF technique. Although in this work the polarity microenvironment change was used to explain the mechanism of switching on the fluorescence signal, it is also worth pointing out that other mechanisms may exist simultaneously. This may include the changes of hydrogen bonding possibility and/or viscosity microenvironment of the fluorophores caused by the polymer phase transition [52]. The details should be investigated in future for USF imaging.

Chapter 3

Develop NIR USF Imaging Contrast Agents

3.1 Introduction

We recently proposed and demonstrated a concept of ultrasound-switchable fluorescence (USF), which aims to achieve high spatial resolution in deep tissue. The promising USF technique highly relies on a unique contrast agent, which must be extremely sensitive to temperature and thereafter of switchable fluorescence. This type of contrast agent highly depends on switchable-fluorescence probes (SFP) and thermosensitive polymers. Recently, switchable fluorescent probes (SFP) have been attracting much attention for imaging specific environmental changes and molecular targets. This is because 1) SFP can provide high target-to-background ratio [66], [67] and therefore has high detection sensitivity, and 2) SFP can specifically respond to certain stimuli and therefore has high specificity. Generally, the fluorescence of SFP stays undetectable (therefore generates a dark background) until the probes are switched on by a specific change in microenvironment or by a unique interaction with a type of molecules or proteins, such as a physical (temperature, polarity, viscosity, etc.), chemical (pH, ion concentration, etc.) or biological (interaction with biomolecules, proteins or DNA, etc.) stimulation.

Many types of SFPs have been developed during the past years. One of the commonly used SFPs is based on environment-sensitive fluorescent dyes. For example, a molecular rotor is a fluorescent molecule that can undergo an intra-molecular twisting motion in the excited state. This twisted excitation state (in some molecular rotors) can lead to significant non-radiation relaxation. Thus, the quantum yield may be extremely low if the formation rate of the twisted state is high. However, when the local viscosity increases, the rotation capability of the molecular rotors is restricted or disabled, and the non-radiation relaxation is suppressed. The quantum yield can dramatically increase and then the molecules are switched on by the viscosity change [68]. Binding with proteins or cell membrane or other cell organelles can lead to the increase of molecular viscosity or the restriction of the rotation, and then switch on the fluorescence. Thus, some molecular rotors can be used for wash-free protein or cell imaging because the signal from those unbound molecules is ignorable.

In last chapter, four SFPs which are sensitive to the polarity of the surrounding environment have been investigated, including: DBD-ED, St633, Sq660, and St700. The concept of USF contrast agents based on them was demonstrated. Basic USF contrast agents were synthesized by using those fluorophores and thermosensitive polymers or NPs. These contrast agents in blue and red wavelength range show high τ_{on}/τ_{off}, acceptable I_{on}/I_{off}, narrow

temperature transition bandwidth (T_{BW}), and adjustable temperature threshold (T_{th}). However, the visible excitation (λ_{ex}) and emission (λ_{em}) photons can be significantly absorbed by biological tissues, so that they may be limited to applications in superficial tissues. Also, the blue excitation light (~470 nm) can generate large autofluorescence in biological tissues, which may lead to significant background noise.

NIR USF contrast agents with outstanding switching properties, such as a large ON-to-OFF ratio in fluorescence intensity (I_{ON}/I_{OFF}), a sharp temperature transition bandwidth between OFF and ON states (T_{BW}), and an adjustable switching threshold (T_{th}) are highly desired, because NIR light can efficiently minimize tissue absorption and therefore can penetrate centimeter-deep tissue. It excites minimal tissue autofluorescence and thus can avoid background noise [69]. A large ratio of I_{ON}/I_{OFF} is essential for suppressing the background fluorescence noise generated by fluorophores in the OFF state (so-called non-100% off fluorescence) and enhancing the signal produced by ultrasonically switched-on fluorophores. Also, the temperature threshold of the USF contrast agents should be adjustable in a board range (e.g. from 20 to 42°C), meeting the need of phantom and *in vivo* animal studies. In this chapter, we investigated the switching mechanism of a recently reported NIR azaBODPIY-based fluorescent dye ($ADP(CA)_2$) first. Then we synthesized and characterized NIR USF contrast agents based on two NIR SFPs with extremely large I_{On}/I_{Off} for centimeter-deep tissue USF imaging.

3.2 Materials and Methods

3.2.1 Materials

N-isopropylacrylamide (NIPAM), acrylamide (AAm), ammonium persulfate (APS), sodium dodecyl sulfate (SDS), N,N,N′,N′-tetramethyl ethylene diamine (TEMED), N,N′-methylenebisacrylamide (BIS), acrylic acid (AAc), N-tert-butylacrylamide (TBAM), sodium ascorbate, indocyanine green (ICG), tetrabutylammonium iodide (TBAI), 4-dimethylaminopyridine (DMAP), dicyclohexylcarbodiimide (DCC), 4-carboxy benzaldehyde, 4,4'-azobis(4-cyanovaleric acid) (ACA), 1-ethyl-3-(3-dimethylaminopropyl) carbodiimide (EDCI), piperidine, cyanoacetic acid, acetonitrile, N,N-dimethyl formamide (DMF), and dimethyl sulfoxide (DMSO, anhydrous) were purchased from Sigma-Aldrich Corporate (St. Louis, MO, USA). Pluronic F127 and F98 were obtained from BASF (Florham Park, NJ, USA). Methoxyl PEG carboxylic acid (PEG-COOH) products (molecular weight (MW) = 20000, 30000, and 40000) were purchased from Nanocs Inc. (New York, NY, USA). Bulk solvents dichloromethane, hexane, and methanol were purchased from Fisher Chemicals (Pittsburgh, PA, USA). All chemicals were used as received.

3.2.2 Characterization of NIR Environment-Sensitive Fluorophores

3.2.2.1 Characterization of $ADP(CA)_2$

The dye is an aza-BODIPY (abbreviated as ADP) derivative. The ADP (core) was chemically reacted with two cyanocinnamic acids (CA), and therefore denoted as $ADP(CA)_2$. $ADP(CA)_2$ has a molecular weight of 927.67 g/M and peak excitation/emission wavelengths of 683/717 nm (in dichloromethane, DCM; Figure 3-1). They are 27-nm red shifted compared with those of the ADP core (656/690 nm, respectively). Also, the two CAs can provide two carboxyl acid (COOH) groups for conjugation with other units for future use.

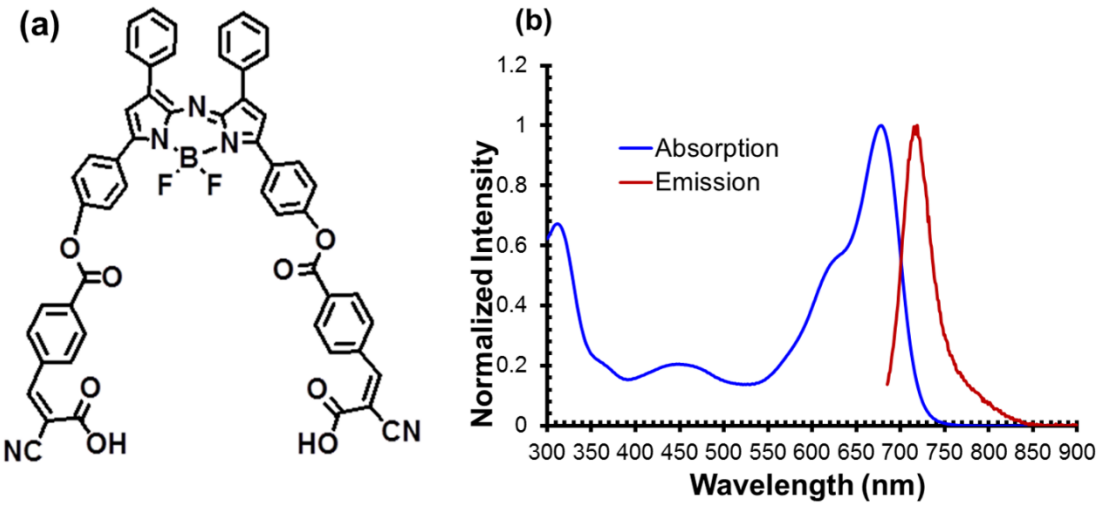

Figure 3-1 Chemical structure, absorption and emission spectra (in dichloromethane) of $ADP(CA)_2$.

The fluorescence measurement system was adopted according to our previous report [50], which also has been described in Chapter 2. Briefly, the excitation wavelength was changed into 655 nm and a 711/25 nm band-pass filter was adopted as the emission filter to reject excitation photons. No temperature control accessories were applied in the current section.

A stock solution was prepared by dissolving $ADP(CA)_2$ in methanol at a concentration of 20 mg/mL (21.5 mM).

Fluorescence response to polarity. Five solvents with different polarity indexes [70] were selected, including water (62.8), dimethyl sulfoxide (DMSO, 45.1), 1,2-dichloroethane (41.3), 1,4-dioxane (36) and toluene (33.9). The final concentration of $ADP(CA)_2$ solution was set as 8.6 nM for measurement, with a total volume of 3 mL.

Fluorescence response to viscosity. Eight solutions with different viscosities were prepared by mixing glycerol and ethylene glycol at different volume ratios, including 0/100, 8/92, 16/84, 25/75, 50/50, 75/25, 90/10, and 100/0. The final concentration of $ADP(CA)_2$ solution was set as 8.6 nM, with a total volume of 3 mL.

Fluorescence response to pH. The pH values of deionized water, including 4.0, 5.9, 6.9, 7.6, and 9.4, were adjusted using 1 M NaOH and 1M HCl. The final concentration of $ADP(CA)_2$ solution was set as 8.6 nM, with a total volume of 3 mL.

*Fluorescence response to KCl***.** A series of KCl solutions were prepared at 0, 50, 100, 150, 200, 250 and 500 mM. The fluorescence measurement was carried out with a cell imaging system as described in the following section. The final concentration of $ADP(CA)_2$ solution was set as 21.5 μM with a total volume of 0.5 mL.

*Fluorescence response to biological macromolecules and surfactant***.** Bovine serum albumin (BSA) solution (1%, w/v) and sodium dodecyl sulfate (SDS) solution (1‰, w/v) were prepared. The final concentration of $ADP(CA)_2$ solution for measurement was 21.5 μM with a total volume of 0.5 mL. The fluorescence measurement was executed on a cell imaging system discussed in the following section.

Fluorescence response in cells. The cell imaging system consists of an inverted fluorescence microscope (Nikon Instruments Inc., Model: Eclipse Ti-U, Melville, NY, USA) and a high-resolution charge-coupled device (CCD) camera (ANDOR, Model: DR-328G-C01-SIL, South Windsor, CT, USA). Adenocarcinomic human alveolar basal epithelial cells (A549, ATCC, Manassas, VA, USA) were cultured at 37 ˚C using RPMI medium supplemented with 10% FBS and 100 U Pen-Strep for use. Prior to imaging, A549 cells were seeded in a 48-well plate at a density of 12,000 cells/cm^2. After 24 h, cell loading was carried out. In $ADP(CA)_2$ cell imaging, 10.75 nmole $ADP(CA)_2$ was added into 500 uL cell media (per well). The fluorescence images were taken directly at the indicated time points without either washing or removing $ADP(CA)_2$-containing culture media. The $ADP(CA)_2$ was excited at 632 nm using a lamp and a band-pass filter (632/22 nm band pass, central wavelength: 632 nm; bandwidth: 22 nm). The emission filter was a 711/25 nm band-pass filter (central wavelength: 711 nm; bandwidth: 25nm). A 20X objective lens was adopted and the exposure time was set to be 3 seconds in all microscope-related imaging experiments. The laser intensity was optimized depending on different imaging experiments.

Fluorescence response in animals. Female Balb/c mice (20-25 gram, n = 3), purchased from Taconic Farms (Germantown, NY), were used in this study. The animal protocols were approved by the University of Texas at Arlington's Animal Care and Use Committee. Animals were anesthetized with a mixture of 2%–3.5% isoflurane and

1–2 l/min of 100% oxygen. To perform fluorescence imaging in live mice, $ADP(CA)_2$ solutions (100 μL) with four different concentrations (10.75 μM, 21.5 μM, 64.5 μM, and 107.5 μM) were injected subcutaneously on the back of the mice. After injection, whole body fluorescence images were taken subsequently at various time points. Those fluorescence images were taken using KODAK In-Vivo FX Pro system (f-stop: 2.5, excitation filter: 630 nm, emission filter: 700 nm, 4 × 4 binning; Carestream Health, Rochester, NY). After background correction, regions of interest were drawn over the implantation locations in the fluorescence images and the mean fluorescence intensities for all pixels in the regions of interest were calculated. All data analyses were performed by using Carestream Molecular Imaging Software, Network Edition 4.5 (Carestream Health).

3.2.2.2 Characterization of ICG

In this study, we also adopted ICG because: 1) it is commercially available with relative low cost; 2) it has relatively large polarity-sensitivity compared with the other two commercially available dyes, Dylight-700 and IR-820 [71]; 3) its peak excitation (780 nm) and emission (830 nm) wavelengths are well located in the far NIR range compared with Dylight-700; 4) its photoactivity has been well studied and is a U.S. Food and Drug Administration (FDA)-approved NIR dye.

Fluorescence response to polarity and viscosity. Two solvents with different polarity indexes [70] were selected, including water (62.8) and 1,4-dioxane (36) to investigate its polarity-sensitivity. Two solvents with different viscosities were chosen, including pure glycerol and pure ethylene glycol to investigate its viscosity-sensitivity. The final concentration of ICG was maintained the same during the measurements, with a total volume of 3 mL. The samples were excited by using a nitrogen-pumped dye laser with a pulse width around 800 picosecond at 775 nm. Two 830 nm long-pass emission filters were used for the fluorescence detection.

3.2.3 Conjugation between Pluronic and PEG

Using Pluronic-F98 and PEG-COOH (MW=30000) as an example, the general procedure is described here. Solution I: Samples of 59.78 mg PEG-COOH and 10.36 mg Pluronic-F98 were dissolved in 15 mL DMSO with gentle heating and vigorous shaking. Solution II: DCC (14.93 mg) was dissolved in 15 mL DMSO. Solution III: DMAP (8.9 mg) was dissolved in 15 mL DMSO. The solution I was transferred into a three-neck flask and purged with nitrogen for 10 minutes. With nitrogen protection, the solution II was dropped into the flask with a pressure-equalizing funnel (1 drop/second). In the same manner, solution III was added to the mixture solution of I and II at a much slower dropping rate (1 drop/3 seconds). After that, the reaction was carried out in a nitrogen-protected environment for 48

hours at room temperature. The resulting solution was dialyzed with a dialysis tubing with 50K molecular-weight cutoff (Spectrum Laboratories Inc, Rancho Dominguez, CA) against DMSO and then water. The purified sample was then collected, freeze-dried, and stored at -20 °C for further use. The Pluronic F98 conjugating with PEG with MW of 20000, 30000 and 4000 represent as F98~PEG20K, F98~PEG30K and F98~PEG40K, respectively.

3.2.4 Synthesis of NIR USF Contrast Agents

3.2.4.1 Synthesis of ADP$(CA)_2$-encapsulated Pluronic nano-capsules (NCs)

Pluronic F127 or F98 was dissolved in deionized water (pH 8, w/v:5%). The dye/TBAI (molar ratio = 1:6) was dissolved in chloroform and kept in sonication for 30 minutes. The dye/TBAI chloroform solution was then dropped into the Pluronic aqueous solution with agitation. The solution was further dispersed with a sonicator (Qsonica, LLC., Newtown, CT, USA) at 20 W for four minutes, and the resulting solution was kept stirring until the chloroform was completely evaporated. The USF contrast agents were collected by solution filtration using a 1.2 μm membrane (Fisher Scientific, Pittsburgh, PA, USA) and an Amicon Ultra centrifugal filter (10000 molecular weight cut-off, Millipore, Billerica, MA, USA).

3.2.4.2 Synthesis of ICG-encapsulated PNIPAM-based NPs

The ICG-encapsulated PNIPAM NPs were used as one example to describe the protocol, and others are similar. ICG was added directly into the reaction solution prior to the polymerization and then loaded into the NPs, likely as a result of the amphiphilic property of the ICG molecule itself. NIPAM (monomer, 0.6822 g), BIS (cross-linker, 0.0131 g), and SDS (surfactant, 0.0219 g) were dissolved with 50 mL de-ionized water in a 250 mL Schlenk tube, followed by purging with nitrogen for 10 minutes. ICG (fluorophore, 0.0034 g), APS (initiator, 0.039 g), and TEMED (accelerator, 51 mL) were added into the tube, which was vacuumed and then filled with nitrogen. The vacuuming/filling procedure was repeated three times to secure a nitrogen-protected environment inside the reaction tube. The reaction was conducted at room temperature for four hours and thereafter stopped by exposure to air when the valve was loosened. The sample was dialyzed against deionized water, using a 10-kDa molecular weight cutoff membrane for 3 days to remove extra surfactants and unreacted materials. The LCST of the PNIPAM-based polymer is adjustable. It has been proved that the introduction of a hydrophilic monomer (such as AAm) into NPs leads to a higher LCST [54]. In contrast, the introduction of a hydrophobic monomer (such as TBAm) will decrease the LCST. ICG-encapsulated PNIPAM copolymer NPs were synthesized by following the above-mentioned protocols except for adding appropriate amounts of monomers, either TBAm or AAm. Because water was used as the solvent for synthesis,

15 mol% of TBAm was found to be the maximum amount of TBAm that can be dissolved in water. Another protocol: in order to maintain the good stability of the ICG-encapsulated PNIPAM nanoparticles, instead of ammonium persulfate (APS), ACA was employed as the initiator (0.070 g). The reaction was carried out at 70°C for overnight in the absence of N,N,N',N'-tetramethyl ethylene diamine (TEMED).

3.2.5 Characterization of NIR USF Contrast Agents

3.2.5.1 Characterization of ADP$(CA)_2$ NCs

We adopted commercially available thermo-sensitive polymers (Pluronics) and their co-polymers with polyethylene glycol (PEG) to synthesize thermo-sensitive nanocapsules for encapsulating the ADP$(CA)_2$: (1) Pluronic-F127, (2) Pluronic-F98, (3) Pluronic-F98~PEG20k, (4) Pluronic-F98~PEG30k, and (5) Pluronic-F98~PEG40k. The size and morphology of the ADP$(CA)_2$ NCs were detected by transmission electron microscopy (TEM, JEOL 1200 EX, Peabody, MA, USA). Samples were prepared by casting an aqueous dispersion of nano-capsules (0.5~1 mg/mL) onto a carbon-coated copper grid (FF200-Cu-50, Electron Microscopy Sciences, Hatfield, PA, USA), followed by staining with 1% uranyl acetate (SPI-ChemTM, SPI, West Chester, PA, USA). A system and steps similar to the one adopted in chapter 2 were used to characterize the optical switching properties of the five NCs (excitation wavelength: 655 nm; emission filter: a 711/25 nm band-pass interference filter).

3.2.5.2 Characterization of ICG NPs

Four USF contrast agents based on ICG were synthesized, including (1) ICG-encapsulated P(NIPAM-TBAm 185:15) NPs, (2) ICG-encapsulated PNIPAM NPs, (3) ICG-encapsulated P(NIPAM-AAm 90:10) NPs, and (4) ICG-encapsulated P(NIPAM-AAm 86:14) NPs.

The diameter of NPs was measured by dynamic light scattering. 200 µL of the sample was diluted with 2.8 mL of deionized water and then measured with Nanotrac 150 (Microtrac, Inc., Nikkiso, San Diego, CA, USA). All measurements were performed in deionized water at room temperature (25 °C). Transmission electron microscopy (TEM, JEOL 1200 EX, Peabody, MA) was used to determine the morphology of the synthesized NPs. In general, samples were prepared by drop casting an aqueous dispersion of NPs (usually at 1 mg/mL) onto a carbon-coated copper grid (FF200-Cu-50, Electron Microscopy Sciences, Hatfield, PA), followed by staining with 0.2% uranyl acetate. The components of the samples were characterized with a Fourier transform infrared (FTIR) spectrometer (data not shown, Thermo Nicolet 6700, West Palm Beach, FL). The spectrum was taken from 4,000 to 600 cm^{-1}. A

system and steps similar to the one adopted in chapter 2 were used to characterize the optical switching properties of the ICG NPs (excitation wavelength: 808 nm; emission filter: an 830 nm long-pass interference filter).

3.3 Results and Discussion

3.3.1 Characterization of NIR Environment-Sensitive Fluorophores

3.3.1.1 ADP(CA)$_2$ characterization

ADP(CA)$_2$ (Compound **(2))**, shows an absorption peak at ~683 nm in dichloromethane (DCM), while its fluorescence emission peak is located at ~717 nm. No significant difference in the fluorescence emission wavelength was found between the reagent (Compound **(1)**) and the product (ADP(CA)$_2$). The result indicates that the functionalization of two cyanocinnamic acid (CA) groups does not affect the Stokes' shift.

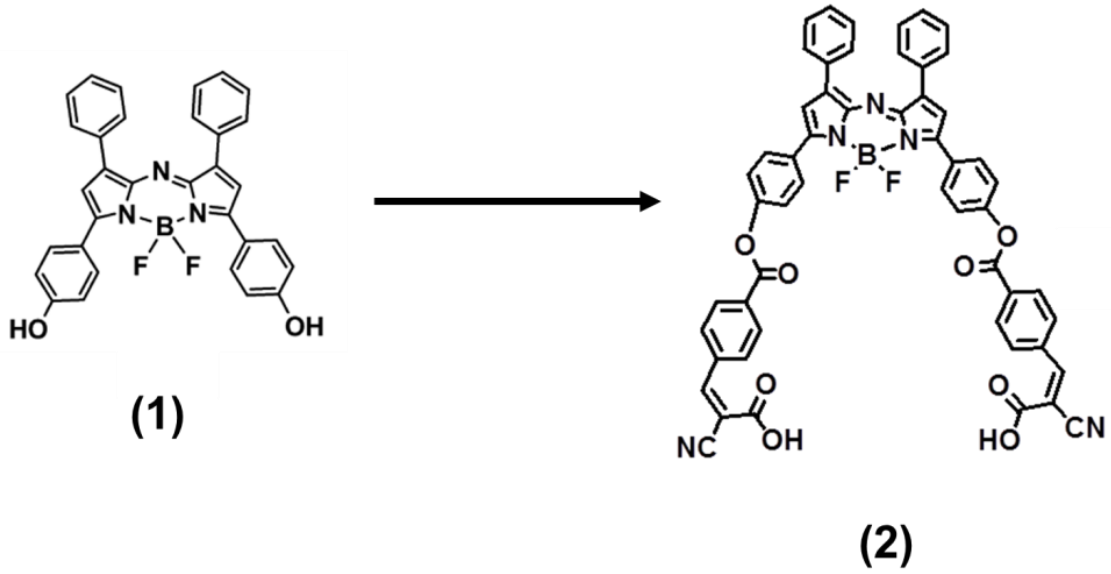

Figure 3-2 Chemical structures and synthesis route of ADP(CA)$_2$.

Fluorescence response to polarity. Our results indicate that ADP(CA)$_2$ is a solvatochromic fluorophore [72], [73] whose emission properties are highly sensitive to the surrounding environment, although the fluorescence of the core fluorophore (azaBODIPY) was reported insensitive to solvent [74]. Water is the most polar solvent, with a polarity index (PI) of 62.8 in terms of $E_T(30)$ [70]. The fluorescence of ADP(CA)$_2$ in water was barely observed as shown as the first red-square point in Figure 3-3(A). As the PI of the solvent decreases, ADP(CA)$_2$ fluoresces stronger. For instance, the fluorescence intensity increases by ~20 times when the solvent was changed from water to dimethyl sulfoxide (DMSO, PI = 45.1). Finally, the fluorescence intensity ratio of $I_{toluene}/I_{water}$ can be ~275. Since very low

concentration of ADP(CA)$_2$ was employed (8.6 nM), we exclude the possibility that fluorescence intensity differs due to the solubility of ADP(CA)$_2$. The non-radiative decay was favored in polar solvent and competed strongly with fluorescence, so when the microenvironment was changed to non-polar solvent, ADP(CA)$_2$ fluoresces strongly and exhibited a "switch-like" fluorescence emission [Figure 3-3(A)]. The mechanism of this fluorescence "switch" is likely related to an internal photo-induced electron transfer (PeT) from the benzene moieties to the aza-BODIPY core. Such PeT resulted in fluorescence quenching that occurred more easily in polar media than non-polar media [75]. It is evidence that the fluorescence lifetime of ADP(CA)$_2$ increases when the solvent polarity decreases (data not shown).

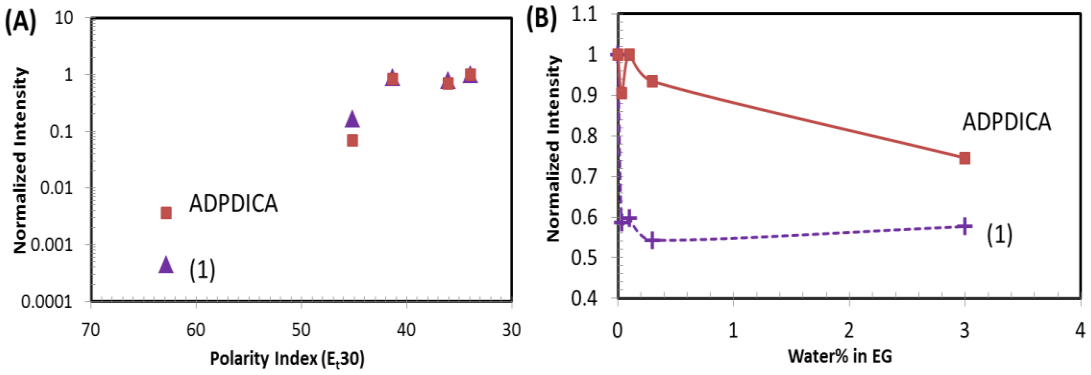

Figure 3-3 (A) Polarity-dependent fluorescence intensity of ADP(CA)$_2$ and Compound (1). Five solvents with different polarity index [70] were employed, which are water (62.8), dimethyl sulfoxide (DMSO, 45.1), 1,2-dichloroethane (41.3), 1,4-dioxane (36) and toluene (33.9). (B) Fluorescence intensity of ADP(CA)$_2$ and Compound (1) in a water/ethylene glycol mixture with different compositions. Excitation: 655 nm; Emission filter: 711/25 band-pass; Laser energy: 50 pJ (A) and 140 pJ (B).

Another possibility is the fluorescence of ADP(CA)$_2$ was significantly quenched in water due to the existence of hydrogen bonding with water [52], [76]. We investigated the fluorescence intensity change as function of the water content in the mixture of water and ethylene glycol (EG, Figure 3-3(B)). EG is a highly polar solvent, with a polarity index that is close to water. Adding of 3% v/v water into EG does not change the polarity. Therefore, the fluorescence intensity of ADP(CA)$_2$ in EG should not change after adding 3% v/v water unless there is hydrogen bonding that quenches the fluorescence. This hypothesis was verified by our results in Figure 3-3(B). Significant decrease of fluorescence intensity was observed for both ADP(CA)$_2$ and Compound **(1)** samples. Furthermore, the fluorescence of Compound **(1)** was found extremely sensitive to water (addition of 0.033% v/v water leads to a 40% drop in

intensity). This huge decrease suggests that the fluorescence of Compound **(1)** can be easily quenched by the formation of hydrogen bonding. The hydrogen bonding site is believed to be located at the oxygen atoms of the phenol groups in Compound **(1)** and ester groups in ADP(CA)$_2$, which were very vulnerable to offer the lone pair electrons to the hydrogen on water. Since the phenol is of much more polarity than ester, the hydrogen bonding with water at the oxygen atoms of Compound **(1)** is stronger. That's why Compound **(1)** is more sensitive to water compared with ADP(CA)$_2$. In a word, the formation of hydrogen bonding with water did make contributions to the switch-like fluorescence of ADP(CA)$_2$.

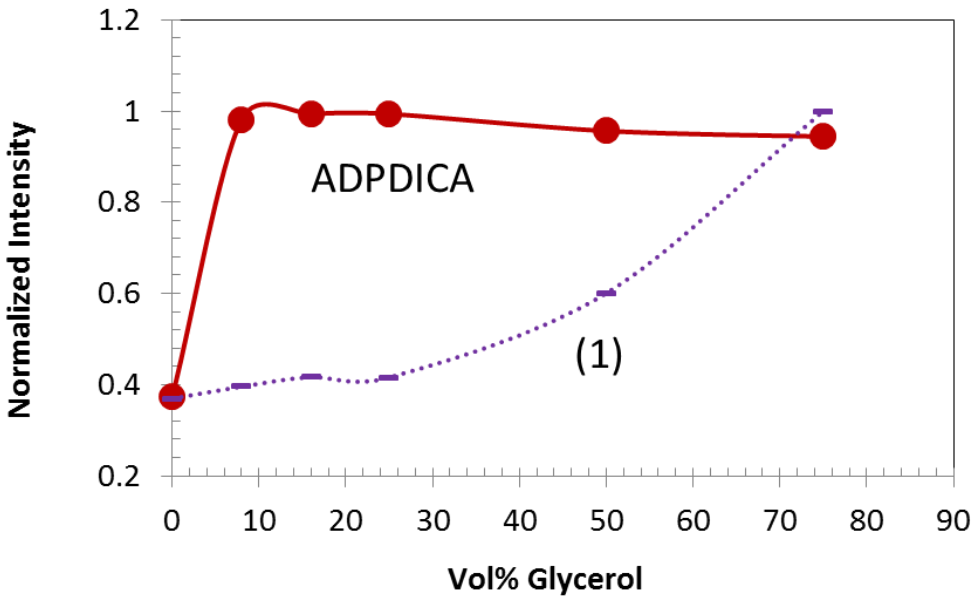

Figure 3-4 Viscosity-dependent fluorescence intensity of ADP(CA)$_2$ in a glycerol/ethylene glycol mixture with different compositions. Excitation: 655 nm; Emission filter: 711/25 nm band-pass; Laser energy: 50 pJ (ADP(CA)2) and 140 pJ (Compound **(1)**).

Fluorescence response to viscosity. Similar to polarity, ADP(CA)$_2$'s fluorescence is also very sensitive to viscosity of the media and shows a switch-like performance (red solid line in Figure 3-4). We herein chose the mixture of ethylene glycol (0.0161 Pa·s) and glycerol (1.412 Pa·s [77]), because the polarity of these two compounds is close to each other. As shown in Figure 3-4, the fluorescence intensity increased 2.5 folds when the volume percentage of glycerol is 8% or above. The fluorescence enhancement can be ascribed to the suppression of the non-radiative decay and the reduction of twisted intramolecular charge transfer (TICT) state, as the rotation of the benzene moieties was

hindered by the increase in viscosity [68]. By contrast, the fluorescence of Compound **(1)** was less sensitive to the increase of viscosity, as shown as the purple dashed line in Figure 3-4.

Fluorescence response to pH. $ADP(CA)_2$ shows pH-independent and weak fluorescence in the pH range of 4~8 (Figure 3-5(A)), whereas it fluoresces strongly under alkaline conditions (pH > 8). Protonation of the tertiary amine makes aza-BODIPY dyes sensitive to pH, and the protonated form often has higher quantum yield than neutral form [73]. Our results suggest that the pK_a value of $ADP(CA)_2$ is above eight, unlike those in relevant reports [73], [78] that pK_a values are below four.

Fluorescence response to KCl. Potassium, the most abundant ion in the cytoplasm, was chosen as an example to investigate the effect of ion concentration on $ADP(CA)_2$'s fluorescence. As shown in Figure 3-5(B), the fluorescence cannot be turned "ON" by the increase of KCl concentration [78].

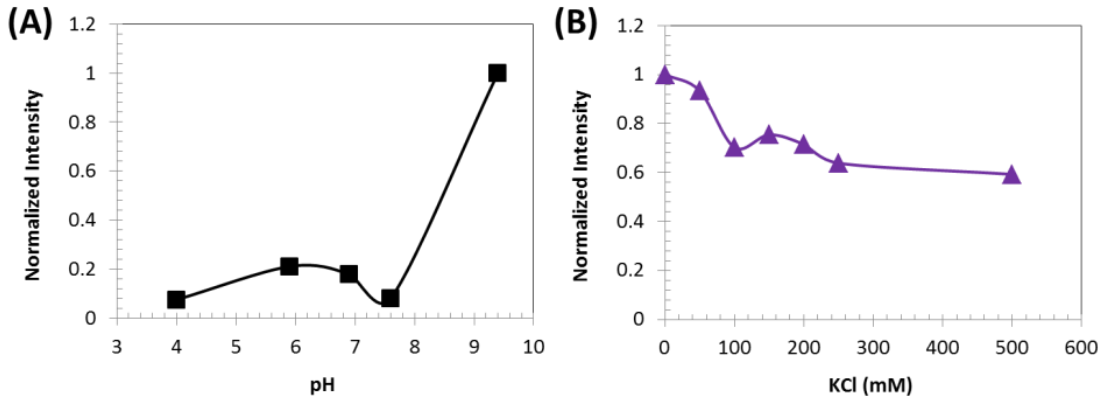

Figure 3-5 Fluorescence intensity of $ADP(CA)_2$ aqueous solutions as a function of pH (A) and KCl concentration (B). (A) Excitation: 655 nm; Filter: 711/25 nm band-pass filter; Laser power: 21.8 nJ. (B) Excitation filter: 632/22 band-pass filter; Emission filter: 711/25 band-pass filter; Light source energy: 100%; Objective: 20X; Exposure time: 3s.

*Fluorescence response to biological macromolecules and surfactant***.** In this chapter, we also investigated $ADP(CA)_2$'s fluorescence change in the absence and presence of biological macromolecules. Bovine serum albumin (BSA) was selected as one example and added into the dye solution for incubation. Non-surprisingly, the fluorescence of $ADP(CA)_2$ was negligibly weak in water (Figure 3-6(a)). The fluorescence intensity for BSA-incubated sample was found to be increased by 12 folds (Figure 3-6(b)), in comparison with that in the absence of BSA. The hydrophobic surface on BSA favors the fluorescence enhancement, as like that in non-polar media. The polarity of BSA surface is

similar with that of acetone [75]. The increase in fluorescence intensity verified that the microenvironment surrounding $ADP(CA)_2$ has been changed, e.g. the polarity becomes smaller, which comes from the interaction between $ADP(CA)_2$ and BSA. Besides, we cannot exclude the possibility that $ADP(CA)_2$ binds to BSA so that the rotation was restricted.

Once $ADP(CA)_2$ was incubated with sodium dodecyl sulfate (SDS, a type of popular surfactant molecules), its fluorescence intensity was found to be increased by 24 folds (Figure 3-6(c)) in comparison with that in water. This enhancement suggests that some $ADP(CA)_2$ may be encapsulated inside the micelle formed by SDS aggregation. The polarity of SDS micelle core was reported to be close to that of methanol in terms of $E_T(30)$ value [70], [79]. Apparently the increase in polarity leads to the fluorescence enhancement of $ADP(CA)_2$.

Taken together, we confirmed that $ADP(CA)_2$'s fluorescence is highly sensitive to polarity and it can be switched on while binding to BSA or being encapsulated in micelle. This property allows us to use it as a switchable fluorescence probe for the investigation of the conformation change of protein or the protein penetration in cellular membrane in the future.

So far, the mechanism of the switching property of $ADP(CA)_2$ is clear. It can be switched on by physical stimulation (including: polarity and viscosity) and biological stimulation (the interactions with proteins). It cannot be switched by chemical simulation (including: pH and ion concentration in physiological range).

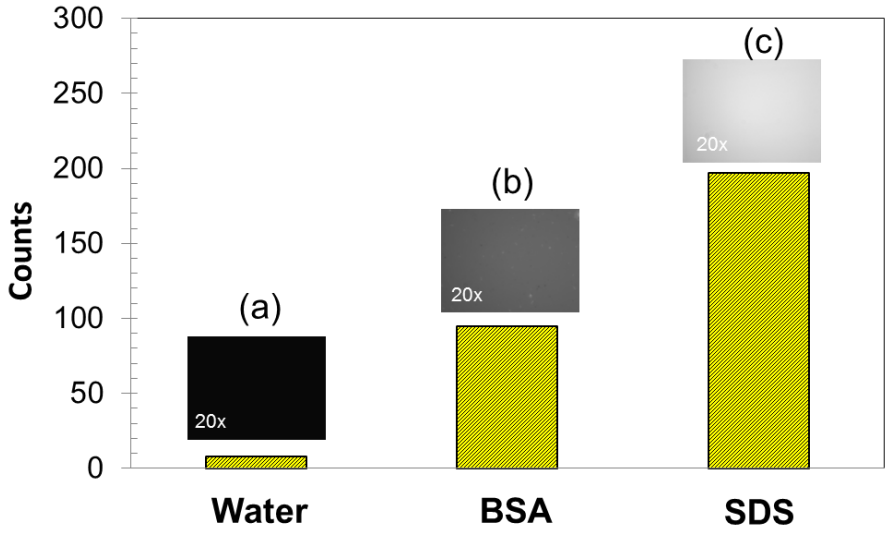

Figure 3-6 Fluorescence intensity of $ADP(CA)_2$ in water (a), 1% BSA solution (b), and 1‰ SDS solution. Excitation filter: 632/22 band-pass filter; Emission filter: 711/25 band-pass filter; Light source energy: 25%; Objective: 20X; Exposure time: 3s.

Fluorescence response in cells. Wash-free live-cell imaging was carried out using adenocarcinomic human alveolar basal epithelial cells (A549 cells). The cells had been incubated with $ADP(CA)_2$ (21.5 μM) for 4 hours. Then the cell fluorescence imaging was performed without any washing steps or removing cell culture medium. As shown in Figure 3-7(B), the cytoplasm was of bright and well-distributed fluorescence while the nucleus stayed dark (no fluorescence). Since cytoplasm contains abundant membrane structures (e.g. endoplasmic reticulum) and all kinds of proteins, $ADP(CA)_2$ would have interactions with them so that the fluorescence of $ADP(CA)_2$ can be switched "ON" significantly. Furthermore, the intracellular viscosity is higher and inhomogeneous, especially the perinuclear region is of the largest viscosity [80]. Thus, we believed that the fluorescence of $ADP(CA)_2$ inside the cells is a comprehensive enhancement by biological and physical stimulation.

The cell culture medium showed very weak fluorescence compared to cells (Figure 3-7(B)). Under the given conditions, the contrast (S/B Ratio, between intracellular fluorescence signal and extracellular background) can be 6 after 120 min incubation (Figure 3-7(C)). We continued measuring the contrast for 2 days, and it remained at 5.3. The high contrast and longtime intracellular fluorescence of $ADP(CA)_2$ make it an excellent fluorescent probe for wash-free live-cell imaging and *in vivo* cell tracking in the future.

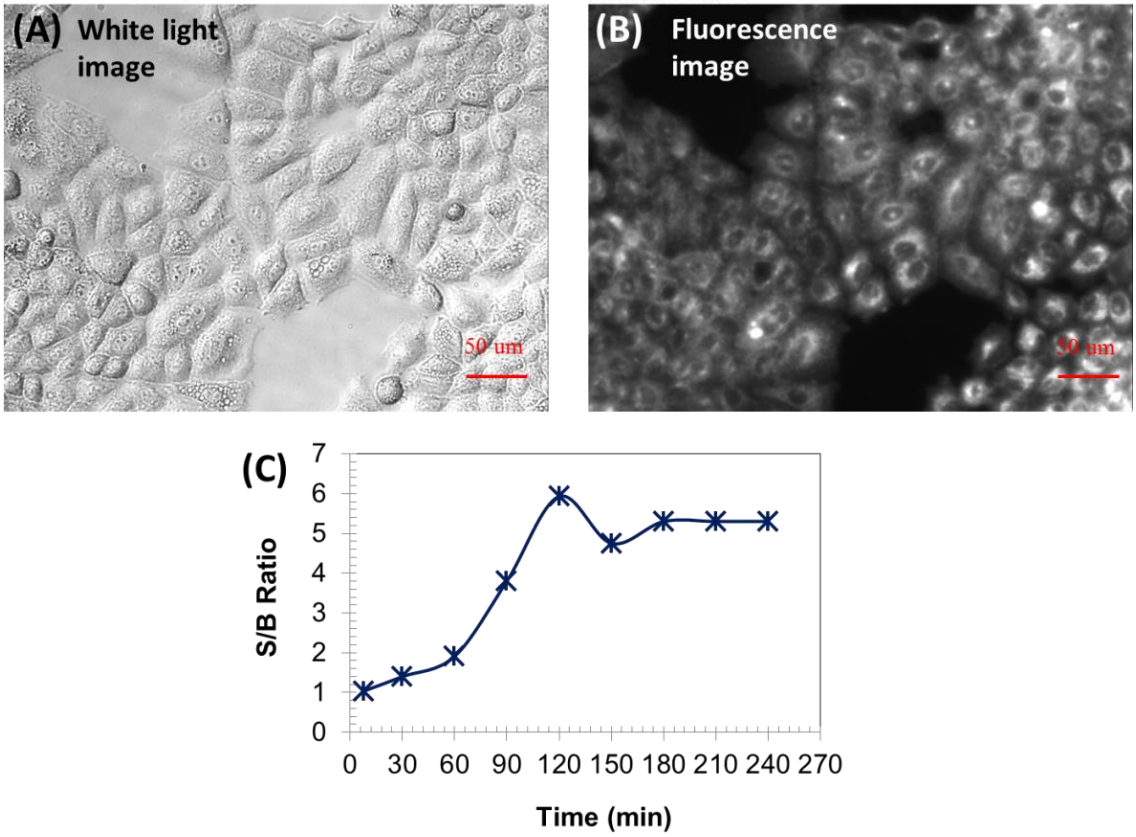

Figure 3-7 White light (A) and fluorescence image (B) of living A549 cells loading with ADP$(CA)_2$ for 120 min without washing. Excitation filter: 632/22 band-pass filter; Emission filter: 711/25 band-pass filter; Light source energy: 25%; Objective: 20X; Exposure time: 3s. (C) S/B ratio as a function of loading time.

The cellular uptake will become more efficient if the fluorophore has hydrophilic moieties [81]. We conjugated ADP$(CA)_2$ with a water-soluble polymer (See Appendix A) and used the conjugate for wash-free cell imaging. Under the same incubation time (e.g. 120 min), the brightness of cytoplasm was found much larger than that using ADP$(CA)_2$ alone (Table 3-1). This is likely attributed to a faster cellular uptake towards ADP$(CA)_2$~Polymer conjugate. Without sacrificing the contrast, the high brightness permits the use of much lower light energy, which in turn will be beneficial to the prevention from photo-bleaching during imaging process.

Table 3-1 The comparison between $ADP(CA)_2$ and $ADP(CA)_2$~polymer conjugate

	S/B ratio	**Intensity (brightness)**	**Loading time**
$ADP(CA)_2$	5.93	172 (light source: 50%)	120min
$ADP(CA)_2$~Polymer	3.75	255*(light source: 50%)	120min
$ADP(CA)_2$~Polymer	4.5	143 (light source: 25%)	120min

*: The intensity is saturated.

Fluorescence response in animals. In order to further demonstrate the switching property of $ADP(CA)_2$ in *in vivo* fluorescence imaging, $ADP(CA)_2$ solutions with four different concentrations were injected subcutaneously on the back of a mouse. As shown in the first image in Figure 3-8(A), four injecting sites were circled in red corresponding to four concentrations (0.5X: 10.75 μM; 1X: 21.5 μM; 3X: 64.5 μM; 5X: 107.5 μM). After injection, whole body fluorescence images were recorded at different time points (Figure 3-8(A)). The results proved that $ADP(CA)_2$ was not fluorescent immediately after injection. A substantial increase in fluorescence intensity was found at the injection sites after 30 minutes (Figure 3-8). That is because only the dye entered the cells can be switched on and the cellular uptake process takes time. With the time increase, more and more dyes were uptaken into the cells. Therefore, the fluorescence intensity increased at the four sites as a function of time. After 4.5 hours, the fluorescence intensity increased 9.7 times at 1X site which is shown in green line in Figure 3-8(B). The final fluorescence intensity depends on how much probe the cells can uptake. Based on our results, 21.5 μM is the best concentration. We also found out the cellular uptake speed is independent of the probe concentration. The *in vivo* results further confirmed the previous conclusion. We believe that when $ADP(CA)_2$ working as the SFP in wash-free live-cell imaging and *in vivo* tissue fluorescence imaging, only intracellular microenvironment could turn on its fluorescence and the fluorescence can be remained for at least 2 days.

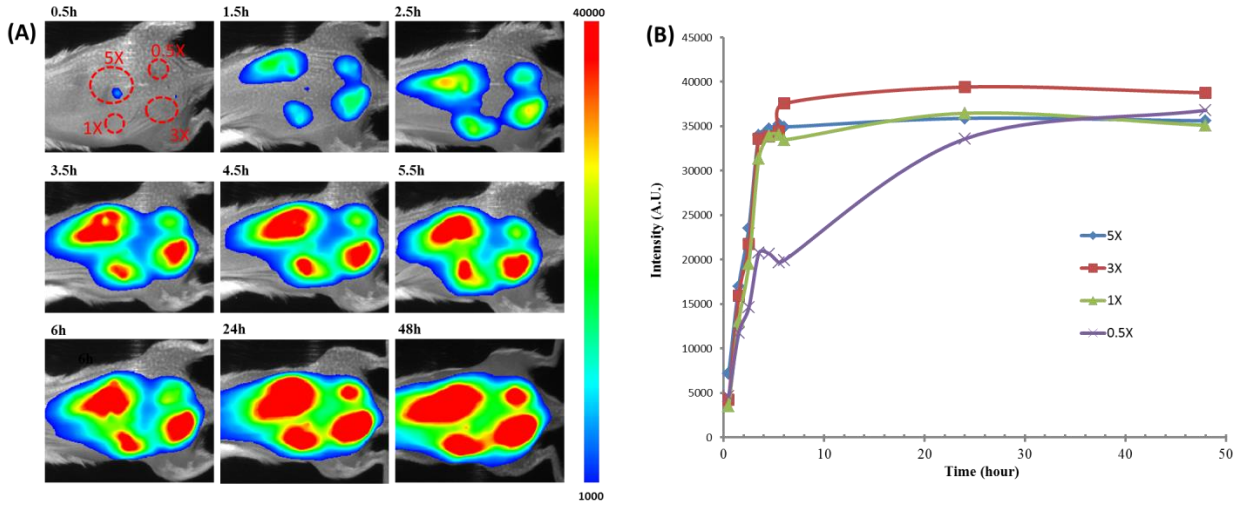

Figure 3-8 ADP(CA)$_2$ solutions with four different concentrations were injected subcutaneously in the back of animals. (A) *In vivo* fluorescence imaging at different time points. (B) The mean fluorescence intensities at the four injection sites as a function of time. Those fluorescence images were taken using KODAK In-Vivo FX Pro system (f-stop: 2.5, excitation filter: 630 nm, emission filter: 700 nm, 4 × 4 binning; Carestream Health, Rochester, NY). All data analyses were performed by using Carestream Molecular Imaging Software, Network Edition 4.5 (Carestream Health).

3.3.1.2 ICG characterization

ICG is a commonly used NIR dye that has a peak excitation at 780 nm and a peak emission at 830 nm [82]. The results indicate ICG is sensitive to the polarity. As shown in Figure 3-9(A), the fluorescence of ICG is stronger when its microenvironment changed from polar (water) to low polar (dioxane). However, regarding of the viscosity, our data shows that a very small increase in fluorescence intensity was observed when increased the viscosity of ICG's surrounding environment (Figure 3-9(B)). Taken together, our data show that ICG is more sensitive to the change of the solvent's polarity than to that of the solvent's viscosity.

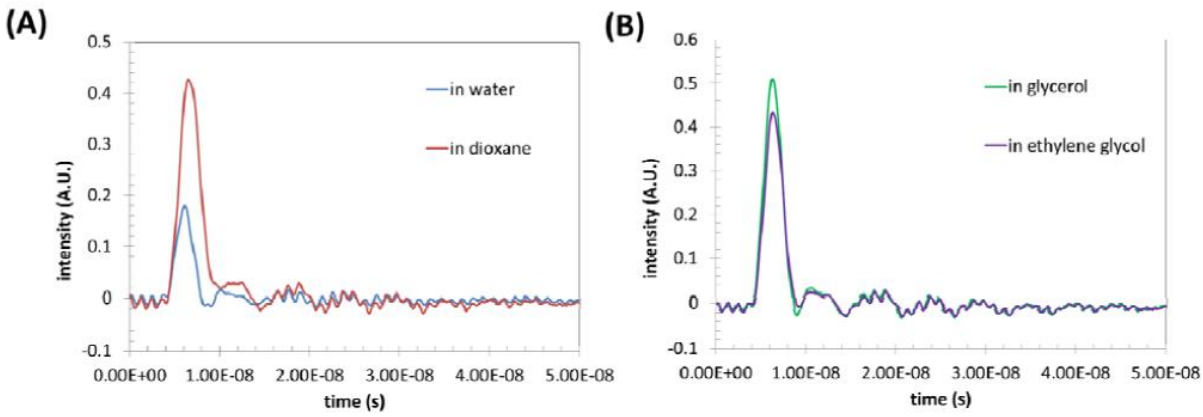

Figure 3-9 Fluorescence of ICG dye in different solvents with varying polarity **(A)** and viscosity **(B)**. The concentration was maintained the same (the difference in solubility is negligible). The samples were excited by using a nitrogen laser-pumped dye laser with a pulse width around 0.8 ns at 775 nm. Two 830 nm long pass emission filters were used for the fluorescence detection.

3.3.2 Characterization of NIR USF Contrast Agents

3.3.2.1 Characterization of ADP$(CA)_2$ NCs

When we encapsulate the environment-sensitive fluorescent dye (ADP$(CA)_2$) into a thermo-sensitive nanocapsule, the dye's fluorescence emission exhibits a switch-like function of the temperature. Figure 3-10 schematically shows the USF concept of the synthesized nanocapsules. When the temperature is below a certain threshold (T_{th1}), the nanocapsule exhibits hydrophilicity and provides a water-rich, polar, and non-viscous microenvironment in which the dye shows very low emission efficiency (so-called OFF). When the temperature is above a threshold (T_{th2}), the nanocapsule exhibits hydrophobicity and can dramatically shrink and expel water molecules. Thus, the nanocapsule provides a polymer-rich, non-polar, and viscous microenvironment in which the dye shows strong emission (so-called ON). If the transition bandwidth ($T_{BW}=T_{th2}-T_{th1}$) is narrow, the fluorescence intensity appears a switch function of the temperature (see Figure 3-12).

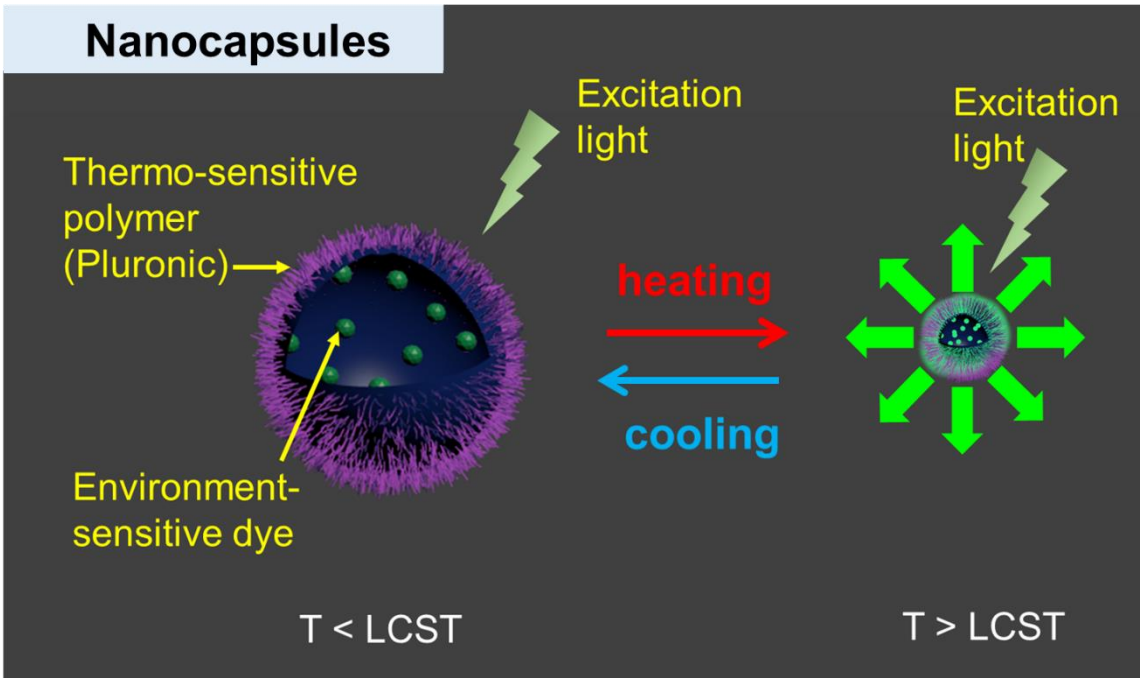

Figure 3-10 A scheme displays the principle of USF nanocapsules (LCST: lower critical solution temperature).

Achieving a high SNR and high sensitivity in centimeter-deep tissue requires a large value of I_{ON}/I_{OFF}. We synthesized (with the help of our collaborator in University of North Texas) and characterized an extremely environment-sensitive NIR dye $ADP(CA)_2$, which has a molecular weight of 927.67 g/M and peak excitation/emission wavelengths of 683/717 nm (in dichloromethane, DCM; Figure 3-1(b)). We found $ADP(CA)_2$ to be extremely sensitive to the polarity (Figure 3-3(A)) and moderately sensitive to the viscosity (Figure 3-4) of its solvent. Meanwhile, $ADP(CA)_2$ is relatively insensitive to pH and KCl ions in the physiological range (pH: 6.8–7.4; KCl:<150 mM) (see Figure 3-5). Therefore, we believe it is an excellent candidate for USF imaging.

We adopted commercially available thermo-sensitive polymers (Pluronics) and their co-polymers with polyethylene glycol (PEG) to synthesize thermo-sensitive nanocapsules for encapsulating the $ADP(CA)_2$: (1) Pluronic-F127, (2) Pluronic-F98, (3) Pluronic-F98~PEG20k, (4) Pluronic-F98~PEG30k, and (5) Pluronic-F98~PEG40k. The diameters of these nanocapsules were found to be in a range of 20–70 nm via transmission electron microscopy (TEM) (see Figure 3-11). The TEM images were acquired from my colleague Dr. Mingyuan Wei.

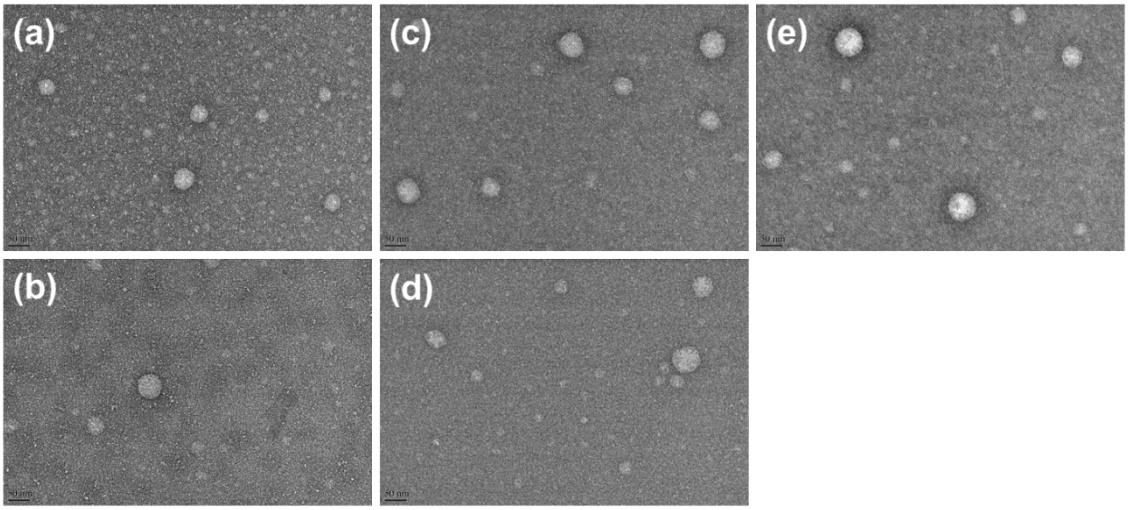

Figure 3-11 TEM images of dye-encapsulated nano-capsules: (a) F127, (b) F98, (c) F98~PEG20K, (d) F98~PEG30K, and (e) F98~PEG40K. Average diameter: (a) 26.0±6.4 (STD) nm, (b) 40.8±9.4 nm, (c) 48.7±10.9 nm, (d) 36.7±9.8 nm, and (e) 56.4±13.7 nm.

Figure 3-12 shows their fluorescence switching performance as a function of temperature; Table 3-2 provides a summary of those contrast agents. Impressively, all the intensity ratios (I_{ON}/I_{OFF}) are >200, while previously developed agents have I_{ON}/I_{OFF} <10 [45], [50], [60], [61]. Figures 3-13 and Figure 3-14 show that ADP$(CA)_2$-encapsulated Pluronic-F127 nanocapsules have excellent stability and switching repeatability. We measured the two curves in Figure 3-13 three days and ten months after synthesizing the agent, respectively. The switching curves match very well. To verify whether the nanocapsules can be repeatedly switched on and off, as an example, Figure 3-14 shows the data measured from ADP$(CA)_2$-encapsulated Pluronic-F127 nanocapsules at low (15 °C) and high (35 °C) temperatures. The fluorescence intensity can be repeatedly switched between the two temperatures for at least eight rounds. Based on the data described above, we expect that ADP$(CA)_2$-based agents should provide high SNR and sensitivity for deep-tissue USF imaging. Among five different nanocapsules, we used ADP$(CA)_2$-encapsulated Pluronic-F127 nanocapsules in the following experiments. The final concentrations of ADP$(CA)_2$ and the Pluronic polymers in the injectable agent solution were ~50 μM and ~16.3 mg/mL, respectively. All the above synthesis protocols and measurement methods can be found in Methods.

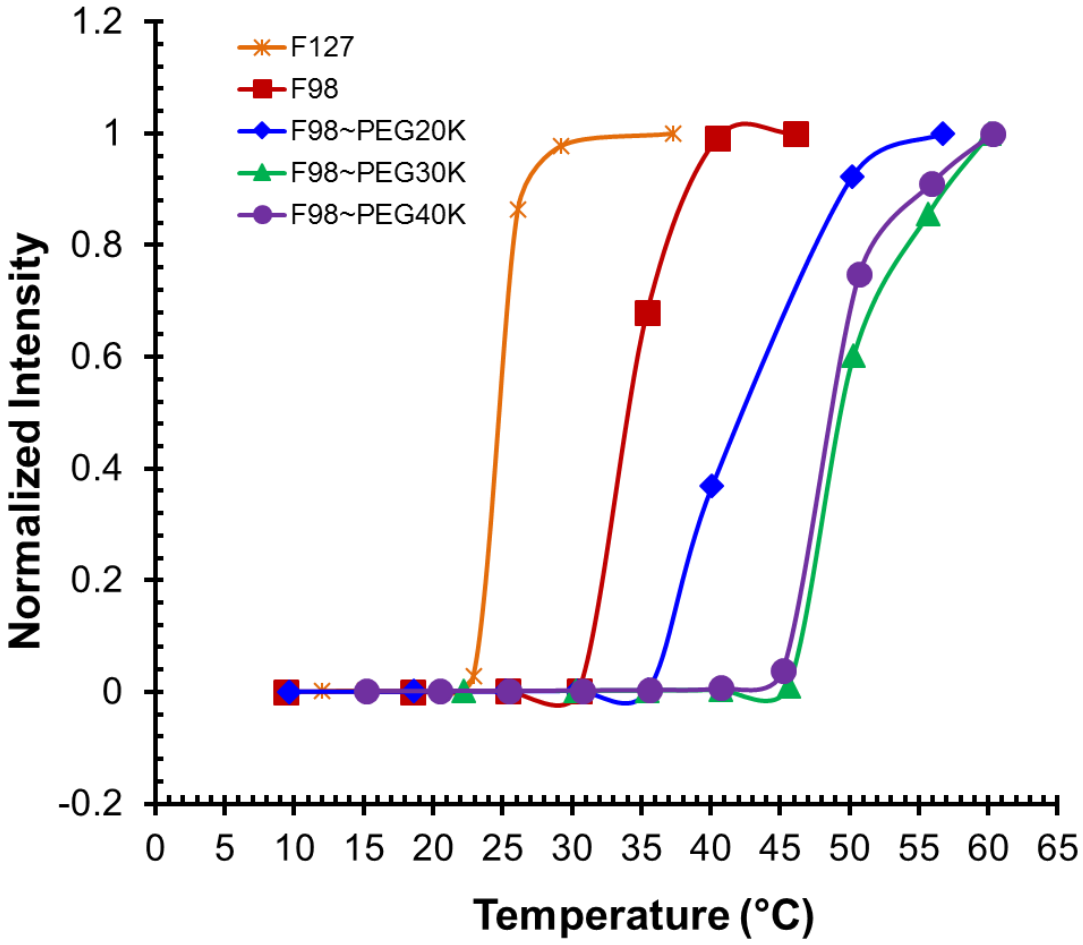

Figure 3-12 The switching relationship between the fluorescence intensity of these ADP$(CA)_2$-based USF contrast agents and the temperature: Pluronic-F127 (stars); Pluronic-F98 (squares); Pluronic-F98~PEG20k (diamonds); Pluronic-F98~PEG30k (triangles); Pluronic-F98~PEG40k (solid circles).

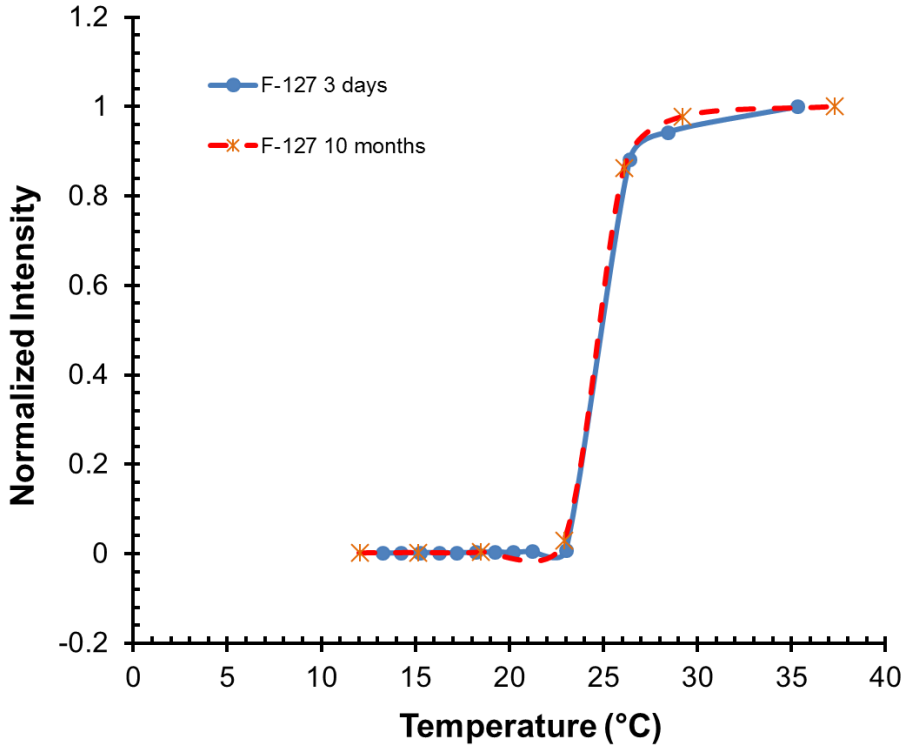

Figure 3-13 The two switching curves measured at different time from the adopted contrast agent, ADP$(CA)_2$-encapsulated Pluronic-F127 nanocapsules. The blue solid line represents the data acquired three days after the agent was synthesized. The red dashed line represents the data acquired ten months after the agent was synthesized.

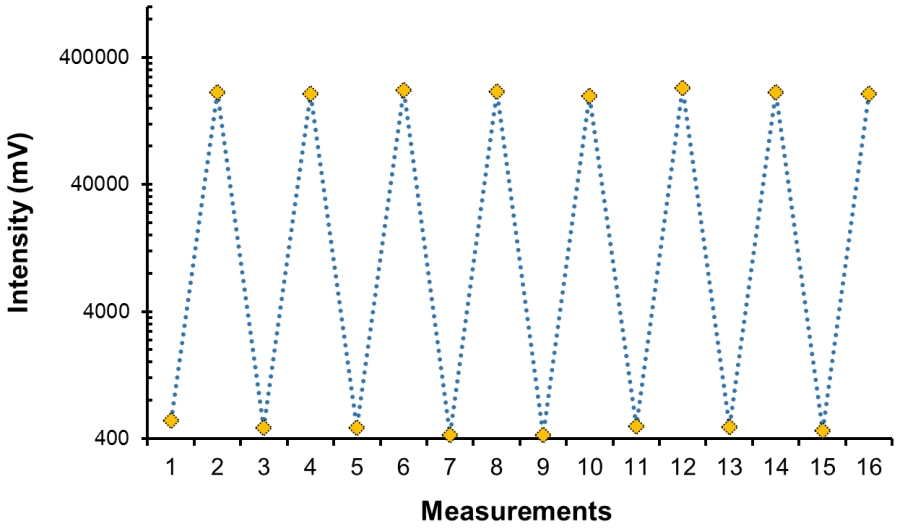

Figure 3-14 Repeatable switching of the fluorescence intensity measured from ADP$(CA)_2$-encapsulated Pluronic-F127 nanocapsules at low (15 °C) and high (35 °C) temperatures.

Table 3-2 Summary of USF contrast agents based on ADP$(CA)_2$. λ_{ex} is the wavelength of the excitation laser in the measurements (655 nm), and λ_{em} is the central wavelength of the band pass emission filter. The number of 25 in the parentheses is the bandwidth of the emission filter. The definitions of the other three parameters are the same as those in our previous publication [50].

Pluronic based Polymers	**λ_{ex}, λ_{em} (nm)**	**I_{On}/I_{off}**	**T_{th1} (°C)**	**T_{BW} (°C)**
F127	655, 711(25)	362	23	4.5
F98	655, 711(25)	352.4	30.5	6.5
F98~PEG20K	655, 711(25)	272.1	35.5	14.7
F98~PEG30K	655, 711(25)	211.6	45.6	10
F98~PEG40K	655,711 (25)	287.6	45.2	6.8

3.3.2.2 Characterization of ICG NPs

Here I would like to acknowledge my colleague Dr. Mingyuan Wei who made major contributions in the experimental results in this section and see the reference [45]. We synthesized a family of USF contrast agents by encapsulating an environment-sensitive NIR dye of ICG into thermo-sensitive nanoparticles. When the environment's temperature is below a threshold (the LCST of the NPs), the NPs are hydrophilic and absorb a dramatic amount of water. Therefore, their size is relatively large [83]. ICG molecules fluoresce weakly in water-rich microenvironment because water provides a polar and non-viscous solvent microenvironment, which can increase the non-radiative decay rate of the excited fluorophores. When the temperature increases above the threshold (LCST), the NPs experience a phase transition from hydrophilic to hydrophobic. Thus, the water molecules are dramatically expelled from the NPs,

and the NPs significantly shrink. Accordingly, the ICG molecules inside the NPs are exposed to a polymer-rich microenvironment, which has a relatively lower polarity and higher viscosity compared with the water-rich microenvironment. This type of microenvironment can suppress the non-radiative decay rate of the excited fluorophores [52], [76], and therefore the fluorescence intensity from the ICG increases dramatically. This phase transition caused by the environment's temperature crossing LCST is reversible. A high intensity focused ultrasound (HIFU) transducer can be used to control the temperature in its focal volume and then locally switch on/off the contrast agents [39].

The NPs are made of thermo-sensitive polymers of either poly (Nisopropylacrylamide) (PNIPAM) or its copolymer with acrylamide (AAm) or N-tert-butylacrylamide (TBAm). Copolymerizing an appropriate amount of AAm or TBAm can increase or decrease the LCST (and therefore the switching threshold) of the copolymer compared with the pure PNIPAM polymer. ICG is a commonly used NIR dye that has a peak excitation at 780 nm and a peak emission at 830 nm. The size of the NPs was found to be between 70 and 150 nm via dynamic light scattering and transmission electron microscopy [45].

Four USF contrast agents based on ICG were synthesized, including (1) ICG-encapsulated P(NIPAM-TBAm 185:15) NPs, (2) ICG-encapsulated PNIPAM NPs, (3) ICG-encapsulated P(NIPAM-AAm 90:10) NPs, and (4) ICG-encapsulated P(NIPAM-AAm 86:14) NPs. The ratio in each NP refers to the molar ratio between the monomer of NIPAM and the monomer of TBAm or AAm. The sharp switching features clearly can be seen for all the four ICG NPs with different switching thresholds (LCSTs: 28, 31, 37, and 41 °C, respectively) [45]. The I_{ON}/I_{OFF} can reach 2.9, 3.3, 9.1, and 9.1 [45], respectively, corresponding to the four LCSTs, which are 1.6–5.1 times higher than that of other contrast agents [61]. This is mainly attributed to the extremely high temperature sensitivity of PNIPAM. To verify whether the NPs can be repeatedly used, as an example, the fluorescence intensity of ICG-encapsulated P(NIPAM-AAm 90:10) NPs was measured at low (25 °C) and high (44 °C) temperatures. The fluorescence intensity can be repeatedly switched between the two temperatures for at least 6 rounds. The results suggest that the ICG molecules are not likely to be released in a short period because of their relatively larger molecular weight (774.96 g mol^{-1}) compared with that of a water molecule (18 g mol^{-1}) [83].

The synthesized USF contrast agents in this study have the following advantages. First, they are NIR contrast agents and therefore can be used for deep-tissue imaging. Second, their ON-to-OFF ratios (I_{ON}/I_{OFF}) are much higher than those of the existing contrast agents. Third, the switching threshold (T_{th}) can be well controlled and therefore can

be potentially used for *in vivo* animal studies in the future whereby the T_{th} should be slightly higher than body temperature (37 °C). Fourth, the transition between on and off states is sharp (generally 3–5 °C). Such a narrow transition bandwidth (T_{BW}) is necessary for efficiently switching on/off fluorescence and avoids potential tissue thermal damage in animal studies. Fifth, the excellent switching repeatability of the developed USF contrast agents allows acquisition of multiple images at the same location for either improving signal-to-noise ratio (SNR) via averaging or monitoring tissue dynamic processes.

3.4 Conclusion

In this chapter, we have characterized two NIR environment-sensitive fluorophores, $ADP(CA)_2$ and ICG. Both of them showed very weak fluorescence in aqueous solution whereas strong fluorescence in non-polar and high-viscose media. Specially, $ADP(CA)_2$ is much more sensitive to its microenvironment compared with ICG. A family of NIR USF contrast agents based on two types of fluorophores and two types of thermosensitive polymers have been synthesized and characterized. They have excellent switching properties including high fluorescence on-and-off ratios, narrow transition bandwidth, adjustable switching threshold, and the excellent switching repeatability. With the help of those contrast agents, centimeter-deep tissue fluorescence high-resolution imaging with good SNR and sensitivity becomes achievable.

Chapter 4

Develop a Sensitive USF Imaging System and an Effective Signal Identification Algorithm

4.1 Introduction

Fluorescence microscopy has broken many physical limits to allow imaging of biological samples and live tissues with unprecedented resolution, contrast, sensitivity, and specificity [24]. Despite significant progresses, fluorescence microscopy is limited to thin samples or superficial tissues (~1 mm) because focusing light into centimeter-deep tissues is extremely difficult [19], [24]. However, high-resolution deep-tissue fluorescence imaging is highly desirable for at least the following reasons [17], [23], [25], [26], [39], [45], [60], [61], [84]–[90]: (1) Much interesting *in vivo* micro-information may deeply locate in tissue, including microcirculation, micro-angiogenesis, micro-lymphangiogenesis, tumor micro-metastasis, and vascularization of implanted tissue scaffolds, etc; (2) Far-red or near-infrared (NIR) light can penetrate centimeter-deep tissue via scattering, although the micro-information is completely blurred; (3) Compared with other imaging modalities such as ultrasound (US), computed tomography (CT), magnetic resonance imaging (MRI), or positron emission tomography (PET), fluorescence imaging stands out in the following respects: high sensitivity, low cost, usage of non-ionizing radiation, feasibility of multi-wavelength imaging, and feasibility of tissue structural, functional, and molecular imaging.

To conduct high-resolution imaging in centimeter-deep tissue via fluorescence, we must address the following fundamental challenges [39], [45], [60], [61], [85]–[90]: (1) confining the fluorescence emission into a small volume to achieve high spatial resolution; (2) increasing fluorescence emission efficiency and sensitively detecting those photons to compensate for the signal attenuation caused by the small voxel size in high-resolution imaging and by tissue scattering/absorption during the propagation toward the photodetector (i.e., increase signal strength and detection sensitivity to signal photons); and (3) exclusively differentiating signal photons from other background photons to increase signal-to-noise ratio (SNR) and sensitivity (i.e., increase the detection specificity to signal photons and reduce noise).

To address the first challenge, optical focusing has been replaced by ultrasonic focusing because tissue acoustic scattering is ~1000 times lower than optical scattering [39], [45], [60], [61], [85]–[89], [91], [92]. Using this method, high-resolution (from microns to hundreds of microns) fluorescence images have been demonstrated at millimeters depth in tissue phantoms [39], [45], [85]–[87], [89]. Despite these successes, these technologies face a fundamental barrier: the quick degradation of SNR and sensitivity to an unacceptable level with the increase of the

imaging depth, the spatial resolution, or both. This is due mainly to the fluorescence signal's quick attenuation below the noise level. Accordingly, high-resolution centimeter-deep tissue fluorescence imaging with high SNR and high sensitivity still remains unachievable.

To break this barrier, we must address the challenges described above. The second challenge has been conquered by developing excellent NIR USF contrast agents in the chapter 2 and 3. The unique USF contrast agents' fluorescence emission can be switched on or off by a focused ultrasound wave. The emission intensity on-to-off ratio (I_{ON}/I_{OFF}) can reach >200, which is >100 times higher than that of the current agent with a similar structure (~1.8) [60], [61]. The large value of I_{ON}/I_{OFF} is one of the keys to achieve high SNR and high sensitivity in centimeter-deep tissue. In this chapter, we developed several USF systems and finally focused on a NIR frequency-domain ultrasound-switchable fluorescence (FD-USF) imaging system to break the third limitation. This FD-USF imaging system can sensitively detect USF signals while significantly suppress noise. Meanwhile, we developed a unique USF signal identification algorithm via correlation to differentiate USF signals from noise effectively.

4.2 Materials and Methods

4.2.1 Continuous Wave (CW) USF Imaging System

4.2.1.1 System setup

A diode laser (MDL-III-808R) was used as the excitation light source. A band pass filter F1 (FF01-785/62-25, Semrock, New York; central wavelength: 785 nm; bandwidth: 62 nm) was used as an excitation filter to clean up any undesirable sideband components of the diode laser, which is located in the pass band of the emission filters. The shutter had a fast response time (0.5 ms). To achieve the best SNR (maximally blocking the leakage of the excitation light and maintaining a high fluorescence signal), two long pass interference filters (F2 and F5; BLP01-830R-25, Semrock, New York; edge wavelength: 830 nm) and two long pass absorptive glass filters (F3 and F4; FSR-RG830, Newport, Irvine, California, cut-on 830 nm) were adopted and positioned at particular places after intensive experimental trials. The excitation laser and corresponding filter sets are changeable to best match different contrast agents' excitation and emission spectrum (i.e., the excitation laser and filter setup mentioned above is for ICG NPs; the excitation laser and filter setup described in the following Section 4.2.2 is for $ADP(CA)_2$ NCs). Two NIR achromatic doublet lenses (AC-254-035-B, Thorlabs, New Jersey) were used to collimate the fluorescence photons for best rejecting the excitation photons by the interference filters and to focus the filtered photons onto a cooled and low-noise PMT (H7422P-20 driven by a high-voltage source C8137-02, Hamamatsu, Japan). The signal was further

amplified by a low-noise current preamplifier (SR570, Stanford Research Systems, California) and acquired by a multichannel oscilloscope (DPO4102B-L, Tektronix, Oregon). A gated sinusoidal wave signal with a central frequency of 2.5 MHz was generated by a function generator (FG, 33220A, Agilent, California) and was further amplified by the radio-frequency (RF) power amplifier (325LA, E&I, New York). The amplified signal was input into the matching network (MNW) to drive the HIFU transducer. The HIFU transducer was focused on the target. A pulse delay generator (PDG, P400, Highland, California) was used to synchronize the entire system. The HIFU transducer was mounted on a three-dimensional translation stage for both initial HIFU positioning and subsequent scanning. In the initial positioning, the HIFU transducer was moved to the position where the temperature signal from the thermocouple reached the maximum (indicating that the thermocouple junction was located on the HIFU focus). This position was considered the center of the image. A rectangular area (4.06×1.02 mm^2) was raster scanned by the HIFU transducer surrounding the center.

4.2.1.2 USF imaging in porcine muscle tissue

USF imaging based on ICG NPs. A small silicone tube (with a mean inner diameter of 0.69 mm) was filled with the aqueous solution of the ICG-encapsulated PNIPAM NPs (LCST = 31°C) and embedded into a piece of porcine muscle tissue to simulate a blood vessel as a target for USF imaging. The porcine tissue has a thickness of ~8 mm (z) and a width of 20 mm (x). The tube was inserted into the tissue along the y direction. The distance from the tube center to the top surface of the tissue is ~4 mm. A fiber bundle with a diameter of ~3 mm (Edmund Optics NT39-366, New Jersey) was used to deliver the excitation light from a laser to the bottom of the tissue to excite the HIFU switched-on fluorophores. The second fiber bundle (Edmund Optics NT42-345) was placed on the top of the tissue to collect USF photons. A 2.5 MHz HIFU transducer (H-108, Sonic Concepts, Washington; active diameter: 60 mm; focal length: 50 mm) was positioned at the bottom of the tissue and focused on the tube region. To efficiently transmit the acoustic energy into the tissue, the HIFU transducer, the bottom surface of the tissue sample, and the fiber bundle for delivering the excitation light were submerged into water. For imaging the tube two dimensionally, the HIFU transducer was scanned on the x-y plane.

USF imaging based on $ADP(CA)_2$ NCs. In this work, a small silicone tube with inner diameter of 0.78 mm and outer diameter of 2.38 mm was filled with the aqueous solution of the $ADP(CA)_2$ contrast agents and embedded into a piece of porcine muscle tissue to simulate a blood vessel as the target for USF imaging. The thickness of the tissue is ~12 mm. The tube was inserted into the tissue along the y direction and the distance from the tube center to

the top surface of the tissue is ~6 mm. The temperature measurement system was excluded. The excitation light source was changed into a diode laser (MLL-FN-671). One 650/60 nm band-pass filter (central wavelength: 650 nm; bandwidth: 60 nm) was applied as the excitation filter and two long-pass filters (edge wavelength: 715 nm) were adopted as the emission filter. A rectangular area (5.08 × 2.03 mm^2) was scanned by the HIFU transducer.

4.2.2 Frequency-Domain USF Imaging System via One Lock-in (LIA) Amplifier

4.2.2.1 System setup

A diode laser (MLL-FN-671, 671 nm, Dragon Lasers, Changchun, Jilin, China) was the excitation light source. The laser was modulated at 1 KHz via a FG (33220A, Agilent, Santa Clara, CA, USA). At the same time, the same FG generated a phase-locked signal and sent it to the LIA (SR830, Stanford Research Systems, Sunnyvale, CA, USA) as its reference signal. We used a band-pass filter F_6 (FF01-673/11-25, Semrock, NY, USA; central wavelength: 673 nm; bandwidth: 11 nm) as an excitation filter to clean up any undesirable sideband components of the diode laser, which was located in the pass band of the emission filters. To achieve the best SNR (maximally suppressing laser leakage), we adopted three long-pass interference filters (F_1 to F_3; FF01-715/LP-25, Semrock, Rochester, NY, USA; edge wavelength: 715 nm) and two long-pass absorptive glass filters (F_4 and F_5; FSR-RG695, Newport, Irvine, CA, USA, cut-on 695 nm) and positioned them in particular places after intensive experimental trials. The excitation laser and corresponding emission filter sets are changeable to best match different contrast agents' excitation and emission spectrum. We used two NIR achromatic doublet lenses (AC-254-035-B, Thorlabs, Newton, NJ, USA) to collimate the fluorescence photons so that the interference filters could best reject the excitation photons and to focus the filtered photons onto a cooled and low-noise PMT (H7422-20 driven by a high-voltage source C8137-02, Hamamatsu, Japan). The signal was further amplified by a low-noise current preamplifier (SR570, Stanford Research Systems, Sunnyvale, CA, USA) and was then fed into the LIA as the input signal. The output signal of the LIA was acquired by a multichannel oscilloscope (MSO4102B-L, Tektronix, Beaverton, OR, USA) and a data acquisition card (BNC-2110, National Instruments, Austin, TX, USA), after which the data was sent to a PC for offline processing. A gated sinusoidal wave signal with a central frequency of 2.5 MHz was generated by the second FG (33220A, Agilent, Santa Clara, CA, USA) and further amplified by the RF power amplifier (325LA, E&I, Rochester, NY, USA). The amplified signal was input to the MNW to drive the HIFU transducer (H108, Sonic Concepts Inc., Bothell, Washington, USA). The HIFU transducer was focused on the micro-vessel. We used the PDG (P400, Highland Technology Inc., San Francisco, CA, USA) to synchronize the entire system. We mounted the HIFU transducer on a manual three-

dimensional translation stage for initial positioning and mounted the sample on a motorized three-dimensional translation stage for subsequent scanning. After initially localizing the HIFU transducer on the vessel, we performed a raster scan.

4.2.2.2 USF imaging in porcine muscle tissue

We purchased the tissues from a local grocery store and cut it into pieces with a thickness of 8 mm. The experimental parameters were as follows: laser power: 2.5 mW; corresponding laser intensity right before entering the tissue: 0.21 mW/cm^2; LIA sensitivity: 500 mV nA; HIFU driving voltage: 80 mV (the estimated mechanical index is 1.7). The LIA time constant was set as 300 ms.

4.2.2.3 Definition of SNR of a USF image or profile

In this study, we defined and calculated the SNR of a USF image (or a profile) based on the following rules. First, we plotted the USF profile along the x direction at each y location on a USF image. We found and defined the profile's peak strength of the profile as signal strength (S). Second, we defined a range on the x-axis, centered at the peak location of the profile and with a width of three times of the FWHM of the profile, as the region for potentially detected USF signals. We defined the area outside this region as the background region and defined standard deviation of all the data measured in the background region as noise strength (N). Third, we defined the ratio of S to noise strength (S/N) as the SNR of the profile. Fourth, we defined the average and the standard deviation of the SNRs of all the profiles on each USF image as the SNR of the USF image and the corresponding error.

4.2.2.4 Effective signal identification algorithm

Because background noise such as auto-fluorescence, laser leakage, or background fluorescence generated from fluorophores outside the ultrasound heating spot does not have the switching property, they therefore do not respond to the ultrasound pulse. Accordingly, all these noises do not have the USF signal's unique temporal pattern (see Figure 4-4(a), (c–d)). Thus, the uniqueness of the USF signal's shape provides an excellent indicator to differentiate them from other background noise. To differentiate USF signal from noise, we selected one of the strongest USF signals at a specific location in an USF image as the reference (such as the signal in Figure 4-4(a) or Figure 4-5(a)). All the data acquired at other locations were correlated with this reference based on the equation 4-1. In the calibration experiments, known targets inside centimeter-deep tissues (including shape, position, and size) were imaged by FD-USF and processed by this algorithm.

After acquiring all USF data, we checked the raw data point by point and compared their curves with the calculated correlation coefficients to make sure they matched (e.g., all the signals in the background area show curves with no specific USF pattern and the calculated coefficients are less than 0.3; all the signals in the targeting area show curves with the USF pattern, and the corresponding coefficients are larger than 0.8). In addition, we knew the target's shape, position, and true size. After intensive trials, we modified the algorithm until the processed image approximated the true case (shape, position, and size). After calibration, we finalized our algorithm and applied it to the experiments presented in the following chapters. We adopted the following strategies: (1) any signal with a CrC<0.3 was considered noise, and its USF strength (I_{USF}) was set as zero; (2) any signal with a 0.3<CrC<0.8 was considered moderately possible to be a USF signal. Its USF strength was modified by multiplying the original I_{USF} with the cube of CrC ($I_{USF}\times CrC^3$) to significantly suppress its level but still leave a certain contribution; (3) any signal with a CrC >0.8 was considered a USF signal and no modification was applied to its I_{USF}. The results of the USF images this algorithm processed are accurate and can be verified by other imaging modalities such as ultrasound imaging and diffuse fluorescence imaging.

4.3 Results and Discussion

4.3.1 Continuous Wave USF Imaging System

Here I would like to acknowledge my colleague Dr. Yanbo Pei, who made major contributions in developing this CW system and see the reference [45].

4.3.1.1 USF imaging system

The system mainly consists of four subsystems: (1) an optical system, (2) an ultrasonic system, (3) a temperature measurement system, and (4) an electronic control system [45]. The optical system includes the delivery of the excitation light and the collection of the emission light. The excitation light is generated from an 808 nm laser and is delivered to the bottom of the sample tissue via the fiber bundle. Although the laser is operated in a continuous wave mode (continuously illuminates once turned on), the time delivering the light to the sample and the illumination duration are controlled by using a fast mechanical shutter (UNIBITZ LS3T2, New York) that is triggered by a pulse delay generator (PDG). The collected fluorescence photons via the second fiber bundle are delivered to a set of emission filters and then received by a photomultiplier tube (PMT).

The carefully designed combination of the four emission filters can maximally reject the excitation photons and pass the emission fluorescence photons. The signal after the PMT is further amplified and then acquired by an

oscilloscope. The ultrasonic system consists of the HIFU transducer and the driving components, including an impedance matching network (MNW), a radio-frequency (RF) power amplifier, and a function generator (FG). The temperature at the HIFU focus is measured by a micron-sized thermocouple via an amplifier and the second oscilloscope. The entire system is controlled by the PDG, including the firing of the HIFU heating pulse, the firing of the excitation light pulse, and the data acquisition of the oscilloscope.

4.3.1.2 Principles

In this study, the ultrasonic exposure time is 300 ms, determined by the width of the gating pulse from the PDG. During the ultrasonic exposure period, the tissue temperature at the HIFU focus rises. After the exposure, the temperature reduces as a result of thermal diffusion. The excitation light illuminates the tissue for 2 ms right before the end of the ultrasonic exposure. At the same time, the fluorescence signal is acquired by the oscilloscope, which is triggered by a pulse from the PDG. The HIFU transducer is scanned by a three-dimensional translation stage. The details about the system can be found in Methods.

Generally, the CW-USF signal is weak and may be contaminated with noise. This problem becomes even more severe when high resolution is desired. This is because the high resolution requires the small focal size and therefore the small amount of USF contrast agents in the focal volume can be switched on. Thus, the amount of the detectable USF photons (the desired signal) dramatically decreases as the resolution increases, while the amount of the noise photons remains stable because noise is not correlated with the focal size and the resolution (see the next paragraph). Accordingly, to successfully image the small tube in deeper tissue, it is necessary to optimize the USF imaging system and use the NIR USF contrast agent with a large I_{ON}/I_{OFF}.

The PMT-received photons potentially consist of four components: (1) excitation photons from the laser due to the leakage of the emission filters, (2) tissue autofluorescence photons within the pass band of the emission filters, (3) photons emitted from the non–100% off USF contrast agents, and (4) USF photons. The first three components are the major noise sources. They can be generated from the entire tissue sample and are not correlated with the ultrasound focus. Therefore, they can be called global noise. The last component is the desired signal, which is uniquely related to the ultrasound focus. It can be called local signal. As the resolution increases, the SNR quickly reduces. Accordingly, minimizing the global noise and increasing the signal level become critical. In the current system, the laser leakage has been significantly suppressed by using the specially designed combination of the emission filters (see the details in Methods). The adoption of the NIR USF contrast agents dramatically avoids the

autofluorescence noise. The large value of I_{ON}/I_{OFF} limits the noise generated from the non–100% off contrast agents and also improves the USF signal. Therefore, it is feasible to differentiate the local USF signal from the global noise by directly monitoring the fluorescence intensity change at different locations.

4.3.1.3 High resolution USF images

USF imaging based on ICG NPs. Here I would like to acknowledge my colleague Dr. Yanbo Pei, who made major contributions in the experimental results discussed in this paragraph and see the reference [45]. The USF image of the tube on the x-y plane was acquired. The full-width-at-half-maximum (FWHM) of the USF image profile along the x direction at each y location was calculated. The averaged FWHM at different y locations were 0.48 ± 0.13 mm. To compare the USF image with a pure ultrasound image, the same sample was scanned on the x-y plane using the same HIFU transducer via the commonly used pulse-and-echo method. At each x-y location, the reflected ultrasonic echo from the top inner boundary of the tube was recorded and used to generate the ultrasound image. Its averaged FWHM is 0.76 ± 0.01 mm and is larger than that of the USF image [45].

Two possible mechanisms may lead to breaking the acoustic diffraction for achieving high resolution—a nonlinear acoustic effect and a threshold effect—both of which have been discussed in our recent publications [39], [40], [45], [46]. Briefly, when a nonlinear acoustic effect occurs, both lateral and axial focal sizes are dramatically reduced below the diffraction-limited size, which can improve the USF spatial resolution. Furthermore, because of the existence of a threshold to switch on fluorescence, USF contrast agents can be switched on only in a volume where the temperature is above the threshold. The size of this volume is usually smaller than the actual size of the ultrasound focal volume if one appropriately selects the threshold and ultrasound exposure power. Thus, the spatial resolution of the USF technique can be further improved.

USF imaging based on ADP(CA)$_2$ NCs. To improve the imaging depth to centimeters (i.e., 1.2 cm in this experiment) by using this system, ADP(CA)$_2$ NCs were adopted. In this study, USF imaging was performed in 12 mm porcine muscle tissue by using ADP(CA)$_2$-encapsulated Pluronic-F127 NCs. Figure 4-1(A) shows an USF image of the tube inside tissue on x-y plane. The detailed sample formation can be found in Methods. The two vertical dashed lines represent the two edges of the tube. When the sample was scanned, the laser light was blocked at y = 0 and y = 2 mm. The full-width-at-half-maximum (FWHM) of the USF image profile along x direction at each y location was calculated. The average FWHM at different y locations was 2.09 ± 0.09 mm. Figure 4-1(B) represents the profile of USF image at y = 1 mm and its FWHM is 2.1 mm. The FWHM is larger than the inner diameter of tube (I.D./O.D.:

0.78/ 2.38 mm). Two possible reasons can cause the large FWHM: (1) In USF, the thermal focal size of the HIFU transducer plays a dominant role compared with its acoustic focal size and usually the former is larger than the later; and (2) The tube thick wall also made contributions since silicone tube wall absorbs most of the acoustic energy compared with tissue which can generate sufficient heat to switch on the $ADP(CA)_2$ NCs. Thus the FWHM is actually the convolution between the HIFU thermal focal size and the partial outer laser of the silicone tube. However, our results indicate the tube was successfully imaged in deep tissue by CW-USF with an acceptable signal-to-background contrast.

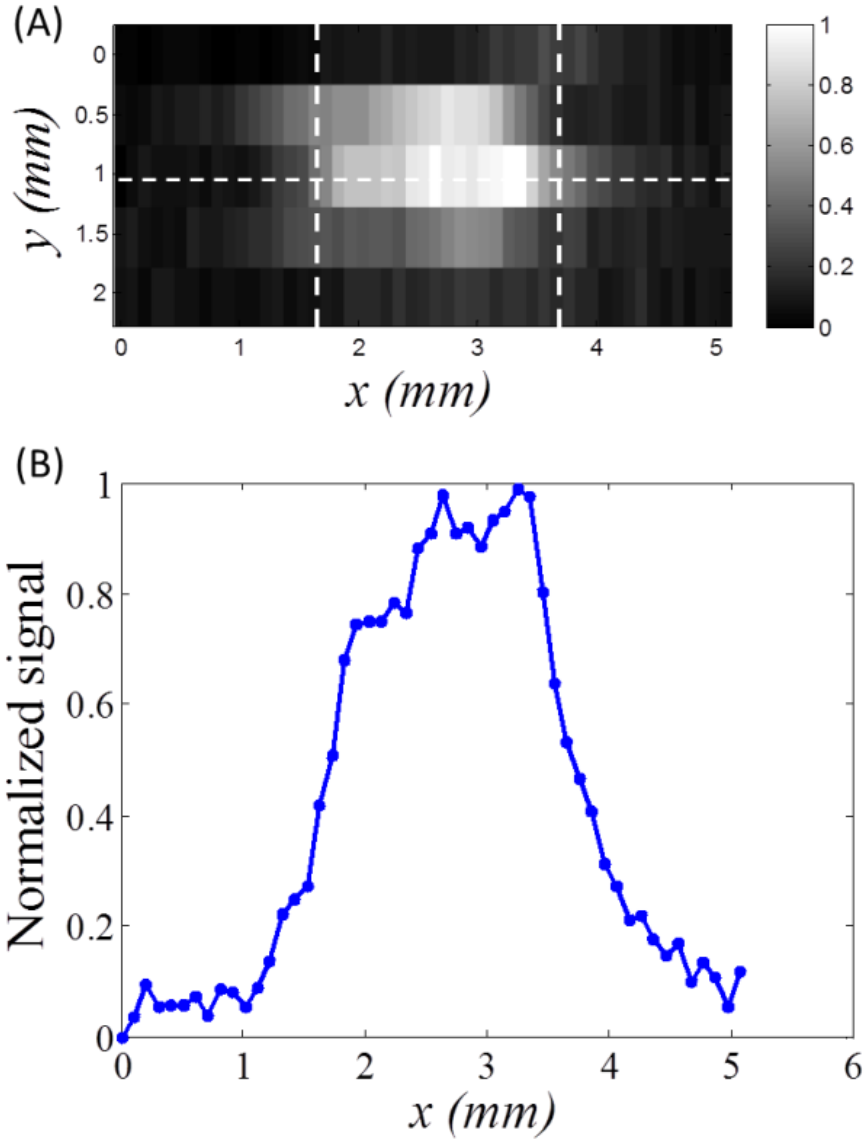

Figure 4-1 (A) The USF image of the tube embedded into the porcine muscle tissue. ADP$(CA)_2$-encapsulated NCs were used as the contrast agents. (B) The profile of the USF signal along the x axis at y = 1 (the horizontal dashed line in (A)). Both the USF image and profile were normalized.

4.3.2 Frequency-Domain USF Imaging System

4.3.2.1 USF imaging system

While excellent USF contrast agents are essential for improving SNR by enhancing fluorescence signal (large I_{ON}) and suppressing background fluorescence noise (small I_{OFF}), a highly sensitive and specific imaging method is also critical for improving SNR. In Section 4.3.1, a CW USF imaging system was developed, which can achieve super high resolution in deep tissue. However, its USF signal is still weak. Thus the detection sensitivity and the SNR of the USF image are relatively poor. In order to further improve the sensitivity, SNR and the imaging depth, a frequency-domain USF imaging system was developed. Figure 4-2 displays a schematic diagram of the imaging system. To increase system's sensitivity to photons and specificity to USF signal (and then achieve a large imaging depth with a high SNR), the following strategies have been adopted: (1) maximizing the system sensitivity to USF photons by adopting a lock-in amplifier; (2) maximizing system's recognition capability between the USF signal and the noises (noises are mainly generated from the laser leakage and/or autofluorescence) via a correlation algorithm; (3) only detecting the change of the fluorescence signal caused by the ultrasound; (4) suppressing laser leakage by optimizing an emission-light-filtering system (ELFS) via a collimation tube combined with multiple emission filters; (5) minimizing autofluorescence by using a far red excitation laser and NIR dyes.

This system is a frequency-domain (FD) system because the excitation laser is modulated at 1 kHz while our previous system is a continuous wave (CW) system without modulation that has relatively lower sensitivity. In the optical sub-system, the excitation laser (at 671 nm) was modulated at 1 kHz via a function generator (FG). The laser sidebands were cleaned up by an excitation filter (F_6) and the excitation light was delivered to the bottom of the tissue sample or animal. The emission light was picked up by a fiber bundle with an inner diameter ~3 mm from the top of the tissue sample or animal. The collected fluorescence photons were collimated, filtered and refocused on a cooled photomultiplier tube (PMT) via two lenses and five emission filters. The combination of three interference filters and two absorption filters was found an efficient way to reject the excitation light and pass the fluorescence light. After the PMT, the 1 kHz fluorescence current signal was converted into voltage signal (with the same frequency) and

further amplified via a low-noise pre-amplifier. Then, a lock-in amplifier (LIA) was used to sensitively detect the change of the amplitude of the 1 kHz fluorescence voltage signal by interfering with a phase-locked reference signal generated from the FG. The output of LIA was acquired by a data acquisition card (DAC, for forming USF images) and an oscilloscope (for monitoring the signal) simultaneously. A pulse delay generator (PDG) was used to control the time sequences by triggering the DAC, oscilloscope, the ultrasonic sub-system and the mechanical scanning sub-system. The acquired data by the DAC was fed into a computer for further off-line processing. The ultrasonic sub-system included a second FG, a radio-frequency amplifier (RF-Amp), an impedance matching network (MNW) and a high-intensity-focused-ultrasound (HIFU) transducer. A mechanical translation stage controlled by the computer was used to scan the sample.

To quantify the point spread function (PSF) and the equivalent spatial resolution of the FD-USF imaging, the profile of the actual tube was de-convolved from the acquired USF profile. The result was considered to be the PSF. The FWHM of the PSF was calculated as ~0.9 mm as the equivalent spatial resolution. The FWHM of the transducer's lateral acoustic profile was defined by the lateral focal size of the HIFU transducer (with a central frequency of 2.5 MHz and f-number of 0.83), which was measured ~0.42 mm. The estimated FWHM of the PSF (~0.9 mm) is ~2 times larger, also larger than what we have observed in our CW system (0.29 mm), which means current FD-USF resolution is ~2 times worse than the lateral acoustic focal size of the HIFU transducer and ~3 times worse than the resolution our previous study reported, where we had adopted a CW system. Thermal diffusion is the main cause of this resolution loss. In the current system, although the ultrasound exposure time remained at 300 ms, USF photon detection required a few seconds because we have adopted the lock-in amplifier. In this study, we set the total data acquisition time at each location to five seconds—much longer than the tissue thermal diffusion time constant (~360 ms) in the current setup. Accordingly, thermal confinement is no longer satisfied and the spatial resolution is degraded, compared to the acoustic focal size of the HIFU transducer and the spatial resolution of the CW-USF system. However, the gain is the improved sensitivity, SNR, imaging depth, and low concentration of the contrast agent.

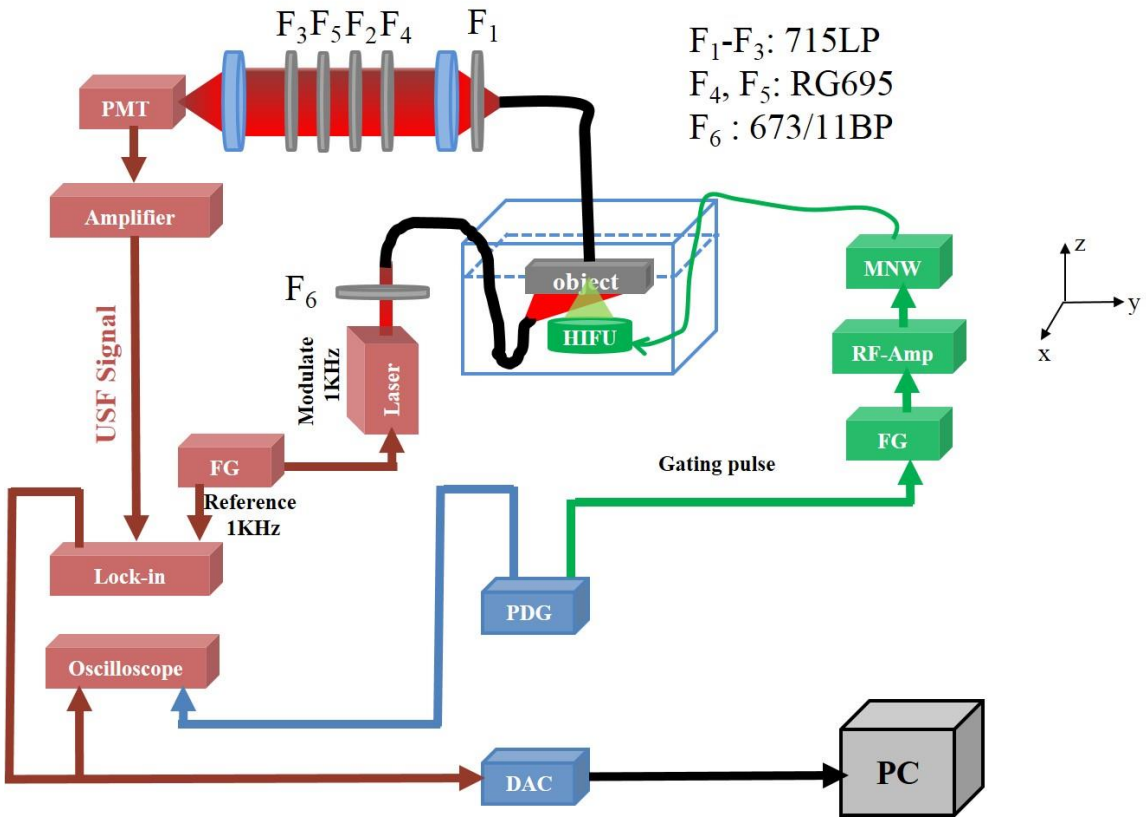

Figure 4-2 The schematic diagram of the USF imaging system. PDG: pulse delay generator; FG: function generator; RF-Amp: radio-frequency power amplifier; MNW: matching network; HIFU: high intensity focused ultrasound; PMT: photomultiplier tube; F1-F5: emission filters; F6: excitation filter; DAC: data acquisition card; PC: personal computer.

4.3.2.2 Principles

Figures 4-3 shows the schematic time sequences of the FD-USF system. The HIFU exposure time is 300 ms (panel 1), which can be adjusted to induce the temperature to rise inside the focal volume (panel 2). The 1 kHz excitation laser is continuously running (panel 3). The HIFU-induced temperature rise leads to a change in the amplitude of the 1 kHz fluorescence signal (panel 4). After interfering with a phase-locked reference signal (panel 5), the LIA outputs the USF signal (panel 6). The peak of LIA output could be delayed to 1–3 seconds due to the LIA integration function. We subtract the LIA output baseline (I_{BG}) from its maximum value (I_{Max}) and use the difference ($I_{USF}=I_{Max}-I_{BG}$) to represent the USF strength (I_{USF}) at that location. I_{USF} can be acquired at each location if the sample or the HIFU focus is scanned to form a USF image.

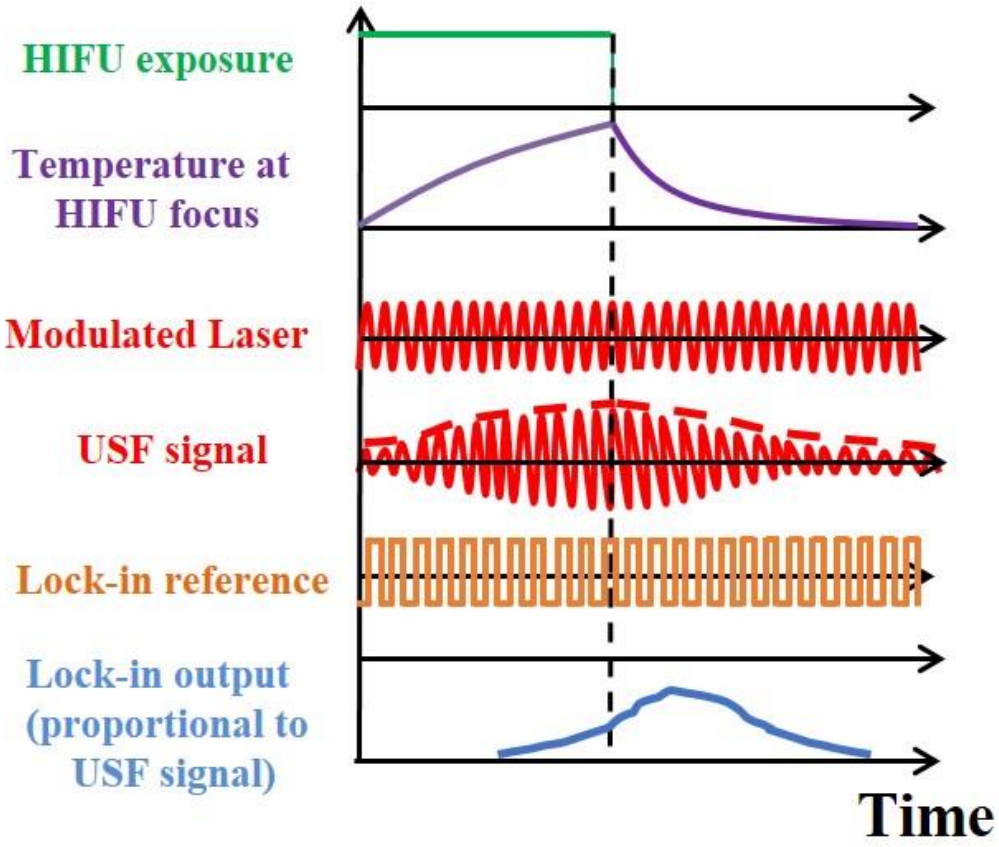

Figure 4-3 The schematic diagram of time sequences of six different events in USF imaging, including HIFU transducer gating pulse, temperature change at HIFU focus, modulated laser output, USF signal, lock-in reference and lock-in output.

4.3.2.3 Typical FD-USF signals

Figures 4-4(a) and (b), respectively, show the typical USF signal and background noise of $ADP(CA)_2$ NCs as a function of time. Clearly, the shape of the USF signal does not correlate with the background noise. Figure 4-4(c) shows a total of seven USF signals with different strengths (see figure caption for detailed values) that overlap substantially after normalization, indicating that the shape of the USF signal is also independent of the signal strength. In contrast, the shape of the USF signal depends on the contrast agent type. Figures 4-5(a) and (b), respectively, show the typical USF signal and background noise of ICG NPs as a function of time. Figure 4-4(d) shows the typical USF signals acquired from those two types of USF contrast agents: (1) $ADP(CA)_2$-encapsulated Pluronic-F127 nanocapsules and (2) ICG-encapsulated PNIPAM nanoparticles. The two curves have quite different dynamic shapes.

Based on the results described above, we can use a correlation algorithm to differentiate USF signals from background noise (to increase SNR) and to differentiate different types of USF contrast agents (to achieve multiplex imaging).

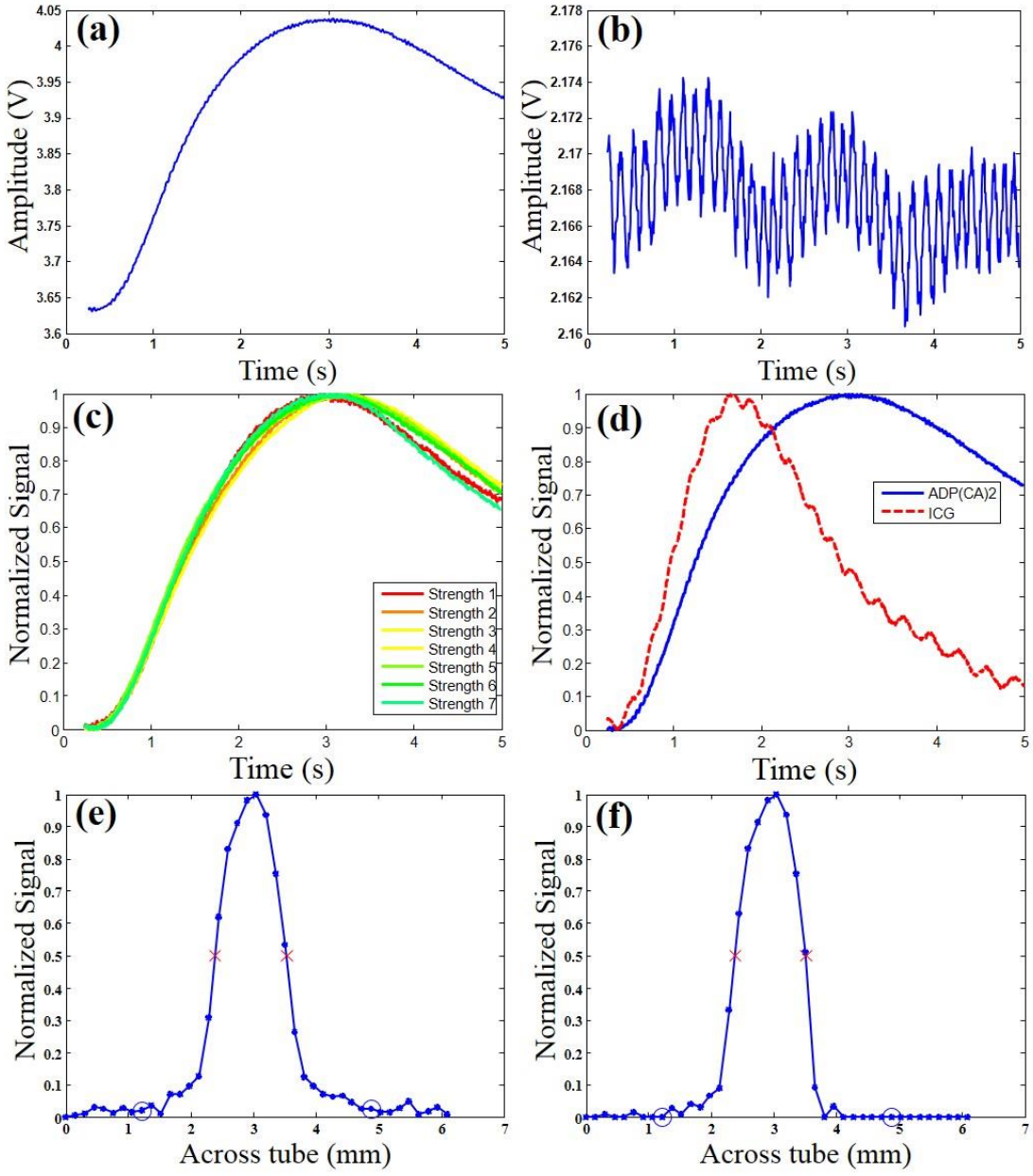

Figure 4-4 Typical USF signals and the correlation method. (a) and (b) show the typical USF signal and background noise acquired from ADP(CA)$_2$-encapsulated Pluronic-F127 nanocapsules in the 8-mm thick tissue USF experiment, respectively. (c) The normalized USF signals (from ADP(CA)$_2$-based agents) with different signal strengths (strength 1-7: 171, 239, 290, 310, 325, 306, and 270 mV, respectively) to show that the shape is independent of the signal strength. Different signal strengths were generated by varying the HIFU driving voltage. (d) The normalized

USF signals from ADP$(CA)_2$-encapsulated Pluronic-F127 nanocapsules (blue solid line) and ICG-encapsulated PNIPAM NPs (red dashed line) agents to show that the shape is dependent on the type of the agents. (e) and (f) are the normalized USF profiles of the micro-tube (filled with the ADP$(CA)_2$-based agent) before (SNR: 88) and after (SNR: 300) correlation analysis, respectively. The experiment conditions are presented in Methods.

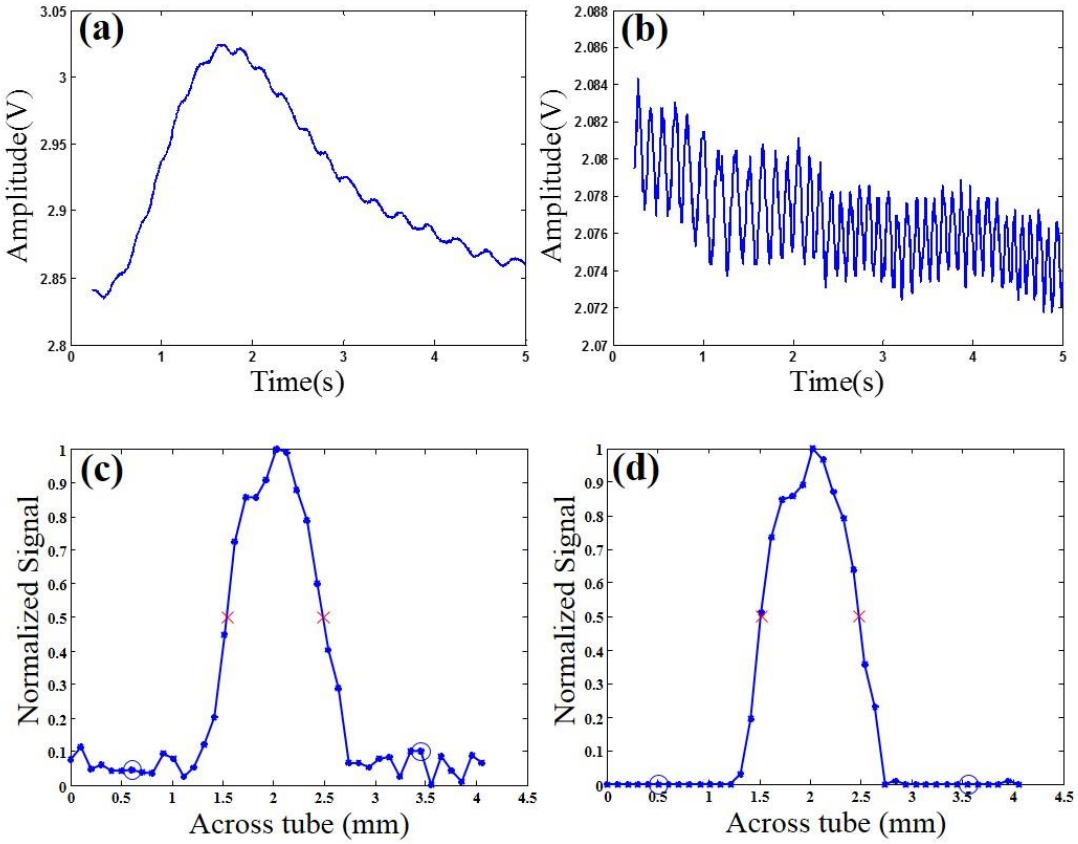

Figure 4-5 Signals related to ICG-encapsulated PNIPAM NPs in 8 mm-tissue, which shows (a) the typical USF signal, (b) the background noise signal, (c) the profile of one line in USF image before correlation (SNR: 31), and (d) the same profile after correlation (SNR: 345).

4.3.2.4 Effective signal identification algorithm

Equation 4-1 shows the correlation coefficient (CrC) between a normalized USF signal at any location ($I(t)$) and a normalized USF reference at a selected location ($R(t)$) [93]. The reference was selected from one of the strongest

USF signals at a specific location in a USF image (such as the signal in Figure 4-4(a) or Figure 4-5(a)). The total data point of *I(t)* or *R(t)* is *N*. After intense calibration experiments, we defined the algorithm as follows. If CrC<0.3, it is considered noise, and its I_{USF} is set to zero. If 0.3<CrC<0.8, its I_{USF} is multiplied with the cube of CrC to partially suppress its contribution. If CrC>0.8, no modification is applied on its I_{USF}. Other details about this algorithm can also be found in Methods.

$$CrC = \frac{\sum I(t)R(t) - \frac{\sum I(t)\sum R(t)}{N}}{\sqrt{\left(\sum I(t)^2 - \frac{(\sum I(t))^2}{N}\right)\left(\sum R(t)^2 - \frac{(\sum R(t))^2}{N}\right)}} \quad \text{[Eq. 4-1]}$$

Figures 4-4(e) and (f) display the normalized USF profiles of a micro-tube embedded in porcine muscle tissue (thickness: 0.8 cm) that was filled with ADP$(CA)_2$-based agent before and after adopting the correlation algorithm, respectively. After the correlation analysis, the signal in targeting area was retained while the signal in background area was suppressed significantly. We applied this correlation method to the experiments in the following chapters to improve the SNR and achieve multiplex USF imaging. Similarly, Figure 4-5(c) and (d) show the typical USF profiles of an ICG NPs-filled silicone micro-tube before and after correlation. The SNRs were found 31 and 345, respectively.

4.4 Conclusion

In this chapter, USF imaging systems from continuous wave to frequency domain were explored. At last, an optimized frequency-domain USF imaging system and a correlation algorithm were developed, which could efficiently differentiate USF photons from the background noise and achieve high sensitivity to USF contrast agents. Besides, unique USF temporal patterns were investigated. The shape information can be used to distinguish USF signals from background noise to increase SNR and also to differentiate different types of agents to achieve multi-color imaging.

Chapter 5

USF Microscopic Imaging in Centimeter-Deep Tissue-Mimicking Phantoms and *ex vivo* Tissue Samples

5.1 Introduction

Fluorescence imaging in deep tissue with high spatial resolution is highly desirable because it can provide details about tissue's structural, functional, and molecular information [24], [25]. Unfortunately, current fluorescence imaging techniques are limited either in penetration depth (microscopy) [24], [25] or spatial resolution (diffuse light based imaging) [19], [26]–[28] as a result of strong light scattering in deep tissue.

For many years, investigators have sought after fluorescence microscopic imaging in centimeter-deep tissue because much interesting *in vivo* micro-information—such as microcirculation, tumor angiogenesis, and metastasis—may deeply locate in tissue. As discussed in previous chapters, there are three challenges to achieve this goal which are: how to confine the fluorescence emission into a small volume to achieve high spatial resolution; how to increase fluorescence emission efficiency to compensate the signal attenuation caused by small emission volume and tissue scattering/absorption; and how to reduce background noise and exclusively differentiate signal photons from background photons to increase SNR and sensitivity. In previous chapters, three unique technologies have been developed: excellent NIR USF contrast agents, a sensitive FD-USF imaging system, and an effective signal identification algorithm. With the help of those developments, all the challenges should be conquered by now.

This chapter aims to validate and demonstrate for the first time the feasibility of USF to achieve centimeter-deep fluorescence microscopic imaging with high SNR and picomole sensitivity in tissue-mimicking phantoms, porcine muscle tissues, and *ex vivo* mouse organs (liver and spleen). The relationship between SNR and imaging depth was investigated. We also demonstrated multiplex USF imaging, which is very useful for simultaneously imaging of multiple targets and observing their interactions in the future. Multi-color USF imaging was achieved via two methods: hardware (multiple scans) and software (single scan). The results of USF were validated by traditional diffuse fluorescence imaging (DF) and ultrasound imaging (US).

5.2 Materials and Methods

5.2.1 Tissue-mimicking Silicone Phantoms

The silicone kit was purchased from Factor II Inc. (VST-50: VerSilTal Silicone Elastomer). The kit includes two major components: silicone elastomer and catalyst. We constructed the tissue-mimicking phantom using silicone (to mimic tissue's acoustic properties) doped with TiO_2 (to mimic tissue's optical scattering properties) [94]. The

estimated absorption coefficient μ_a = 0.03 cm^{-1} and reduced scattering coefficient μ_s' = 3.5 cm^{-1}. The mixture solution was poured into a plastic container and a silicone micro-tube or five silicone micro-tubes were inserted in the middle. The container was then placed into a vacuum to remove air bubbles inside the mixture for 20 minutes. After 6 hours, the tissue-mimicking silicone phantom was ready to use.

5.2.2 One-color USF Microscopic Imaging in Centimeter-deep Silicone Phantoms

A micro-tube (with a mean inner diameter of 0.31 mm) was filled with the aqueous solution of the $ADP(CA)_2$-encapsulated Pluronic-F127 NCs (abbreviated as $ADP(CA)_2$ NCs in the following content) and embedded into a tissue-mimicking silicone phantom to simulate a blood vessel as a target for USF imaging. Figure 5-1 shows the configuration of the sample, the tube, the excitation light, the fluorescence collection fiber, and the high intensity focused ultrasound (HIFU) transducer. The phantom has a thickness of ~11 mm (z) and a width of 40 mm (y). The tube was inserted into the tissue along the x direction. A fiber bundle with a diameter of ~3 mm (Edmund Optics NT39-366, New Jersey) was used to deliver the excitation light from a laser to the bottom of the tissue to excite the HIFU switched-on fluorophores. The second fiber bundle (Edmund Optics NT42-345) was placed on the top of the tissue to collect USF photons. A 2.5 MHz HIFU transducer (H-108, Sonic Concepts, Washington; active diameter: 60 mm; focal length: 50 mm) was positioned at the bottom of the phantom and focused on the tube region. To efficiently transmit the acoustic energy into the tissue, the HIFU transducer, the bottom surface of the tissue sample, and the fiber bundle for delivering the excitation light were submerged into water. For imaging the tube two dimensionally, the HIFU transducer was scanned on the x-y plane.

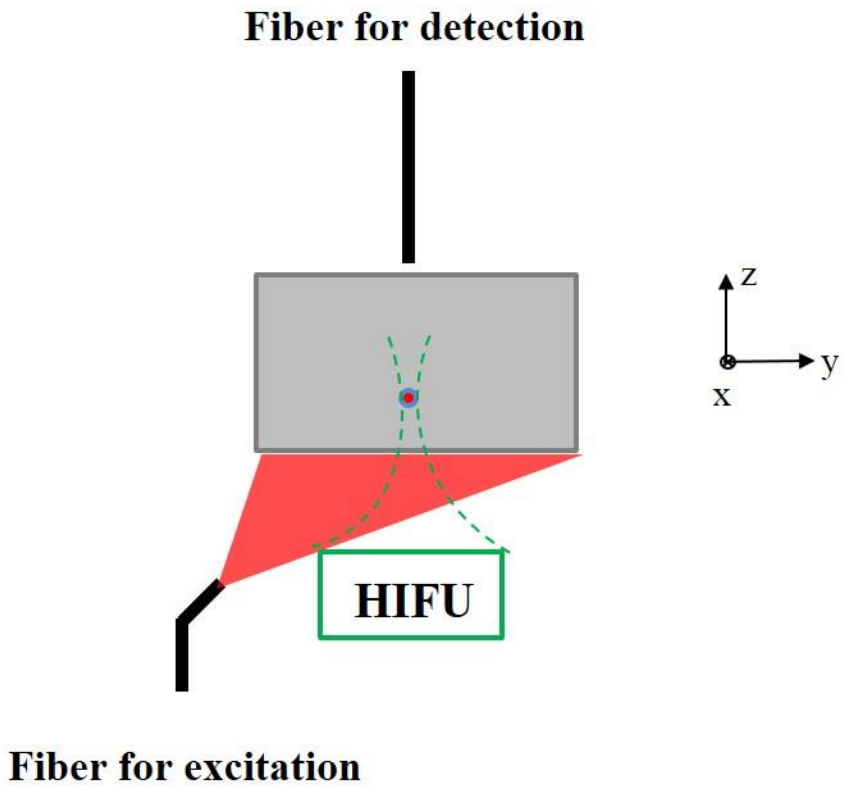

Figure 5-1 The sample configuration, including the sample, the excitation and emission fiber bundles, and the HIFU transducer.

5.2.3 Multi-color USF Microscopic Imaging in Centimeter-deep Tissue Phantoms

5.2.3.1 Multi-color USF imaging by using different instrument setups with multiple scans

System Setups. (1) ADP$(CA)_2$ channel: The excitation light source is a diode laser (MLL-FN-671). One 673/11 nm band-pass filter (central wavelength: 673 nm; bandwidth: 11 nm) was applied as the excitation filter and three 711/25 nm band-pass filters (central wavelength: 711 nm, bandwidth 25 nm) combined with two long-pass absorptive filters (edge wavelength: 695 nm) were used as the emission filters. (2) ICG channel: The excitation light source is a diode laser with the excitation wavelength of 808 nm; Emission filter setup: two long-pass interference filters (edge wavelength: 830 nm) combined with two long-pass absorptive glass filters (edge wavelength: 830 nm).

In two-color USF imaging, two micro-tubes (inner diameter: 0.31 mm; outer diameter: 0.64 mm) were embedded into a porcine muscle tissue phantom with a separation distance of 3 mm in lateral. The thickness of the tissue is ~10 mm. Figure 5-2 shows the phantom sample setup. One tube was filled with ADP$(CA)_2$-based contrast

agents and the other one was filled with ICG-based contrast agents. A high intensity focused ultrasound (HIFU) was used to externally and locally switch on and off USF contrast agents inside the tubes. The fluorescent photons were collected by a cooled and low-noise PMT. Then the signal was fed into the lock-in amplifier. The output of the LIA was collected by a DAC. After two raster HIFU scanning, two-color USF images were achieved by using different instrument setups.

Figure 5-2 The tissue phantom setup for two-color USF imaging.

5.2.3.2 Multi-color USF imaging by using same instrument setup with single scan via correlation

System setup. The excitation light source is a diode laser with the excitation wavelength of 671 nm (MLL-FN-671). One 673/11 band-pass filter (central wavelength: 673 nm; bandwidth: 11 nm) was applied as the excitation filter and three long-pass interference filters (edge wavelength: 715 nm) combined with two long-pass absorptive filters (edge wavelength: 695 nm) were used as the emission filters.

The five-tube embedded tissue-mimicking silicone phantom was made for this study. Figure 5-3 show the photos of the phantom. The thickness was ~13 mm. Five tubes with the I.D./O.D. of ~0.31/0.64 mm and a separation distance of 3 mm were inserted and located at a depth of ~6 mm. The two edged tubes were used for localization when comparing the results of different imaging modalities and were noted as two edges. We filled them with the

corresponding contrast agent of each modality: air for US imaging, ICG-based agents for color-1 USF imaging, $ADP(CA)_2$-based agents for color-2 USF imaging, and $ADP(CA)_2$-based agents for DF imaging. The multi-color USF imaging can be achieved in single scan. After scanning, the two-color contrast agents were distinguished by using the correlation algorithm based on their unique USF temporal patterns.

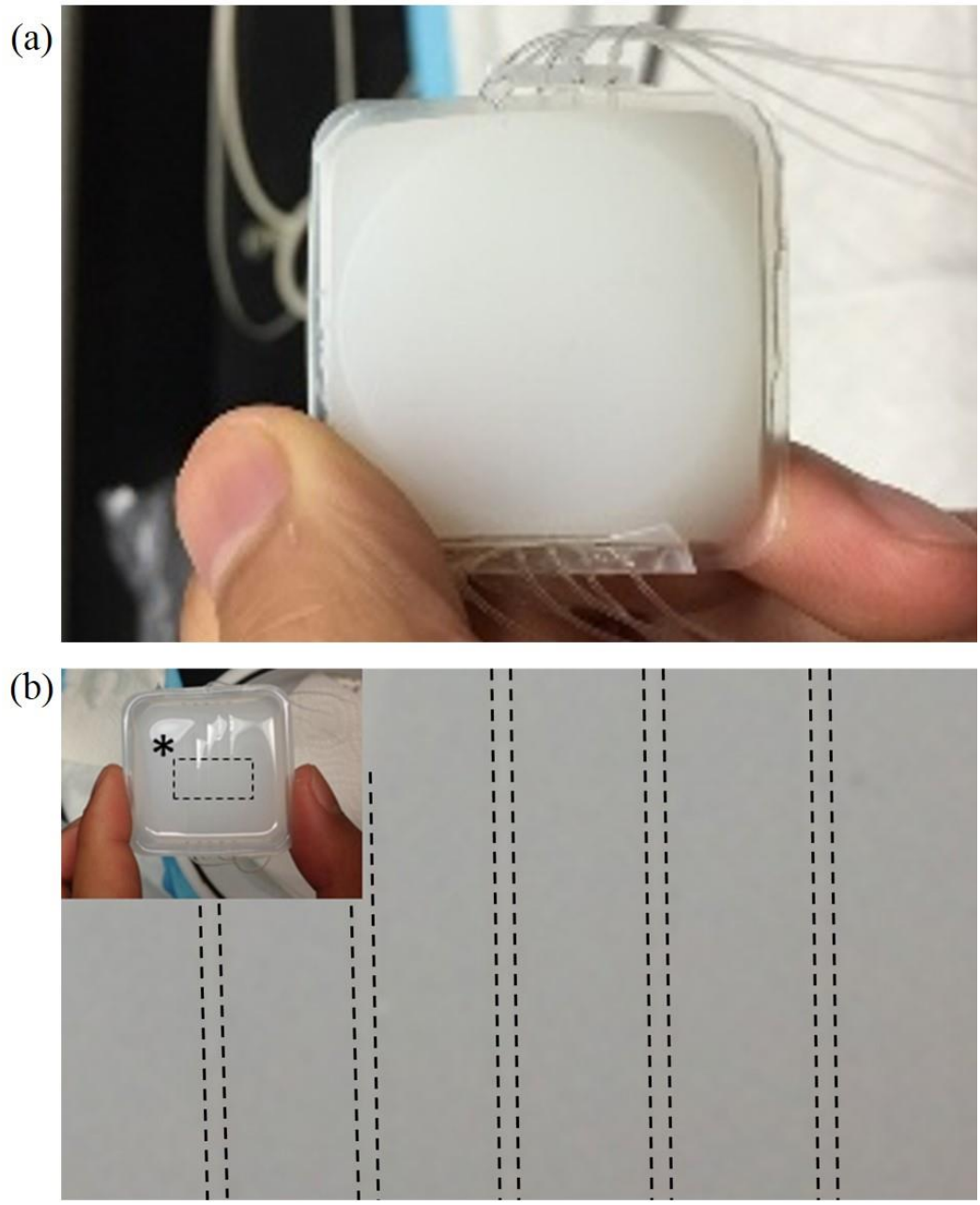

Figure 5-3 The tissue-mimicking silicone phantom with 5 micro-tubes embedded for multi-color USF imaging, diffuse fluorescence imaging and ultrasound imaging. (a) The photograph of the phantom. (b) Cross-section photo showing the position of the tubes.

5.2.4 Validation via Traditional Diffuse Fluorescence Imaging

The phantom was the same as the one in Section 5.2.3.2. In diffuse fluorescence imaging, the sample was scanned in the same way of USF imaging. The only difference is HIFU remained off during the whole scanning.

5.2.5 Validation via Ultrasound Imaging

The phantom was the same as the one in Section 5.2.3.2. The same HIFU transducer was used to ultrasonically image the same tubes in the sample. A pulser/receiver (5073 PR, Olympus NDT, USA) was used for both exciting the transducer and receiving the reflected acoustic echoes. The MNW was used for the impedance matching between the transducer and the pulser/receiver. The reflected acoustic signal was amplified by the pulser/receiver and acquired by a digitizer (NIUSB 5133) interfaced to a computer. This received signal is usually called an A-line in the ultrasound imaging field and represents the tissue acoustic impendence distribution along the depth (z) direction. The A-line was acquired at each location on the x-y plane. By scanning the HIFU transducer on the x-y plane, a set of three-dimensional (x, y, and z) data was acquired. The envelope of each A-line was calculated for forming the C-mode images at different depths. To compare with the USF image, a set of two-dimensional data on the x-y plane (one of the C-mode images) was extracted by fixing the depth of z at the tube location.

5.2.6 USF Microscopic Imaging in Porcine Muscle Tissues with Different Thicknesses

We purchased the tissues from a local grocery store and cut them into different thicknesses. The experimental parameters for the four thicknesses (0.8, 1.2, 2.2, and 3.1 cm) were as follows: laser power: 2.5, 2.5, 2.5, and 38.64 mW; corresponding laser intensity right before entering the tissue: 0.21, 0.21, 0.21, and 3.19 mW/cm^2; LIA sensitivity: 500, 500, 200, and 200 mV nA; HIFU driving voltage: 80, 80, 80, and 100 mV (the estimated mechanical index is 1.7, 1.7, 1.7 and 2.19). For all experiments, the LIA time constant was set as 300 ms.

5.2.7 USF Microscopic Imaging in ex vivo Mouse Organs

BALB/c mice (female, 20–25 gram) were purchased from Taconic Farms Inc. (Germantown, NY, USA). The animal protocols were approved by the University of Texas at Arlington's Animal Care and Use Committee. Animals were intravenously administered 100 μL final solution of the $ADP(CA)_2$-based contrast agents. Twenty-four hours later, the animals were sacrificed and their organs were rapidly dissected. The isolated organs were then placed on the USF system for imaging. Figure 5-4(a) and (b) show the sample setup of mouse liver and spleen, respectively. In this *ex vivo* USF study, all the USF-related parameters were identical to those in the 12-mm thick tissue sample USF imaging.

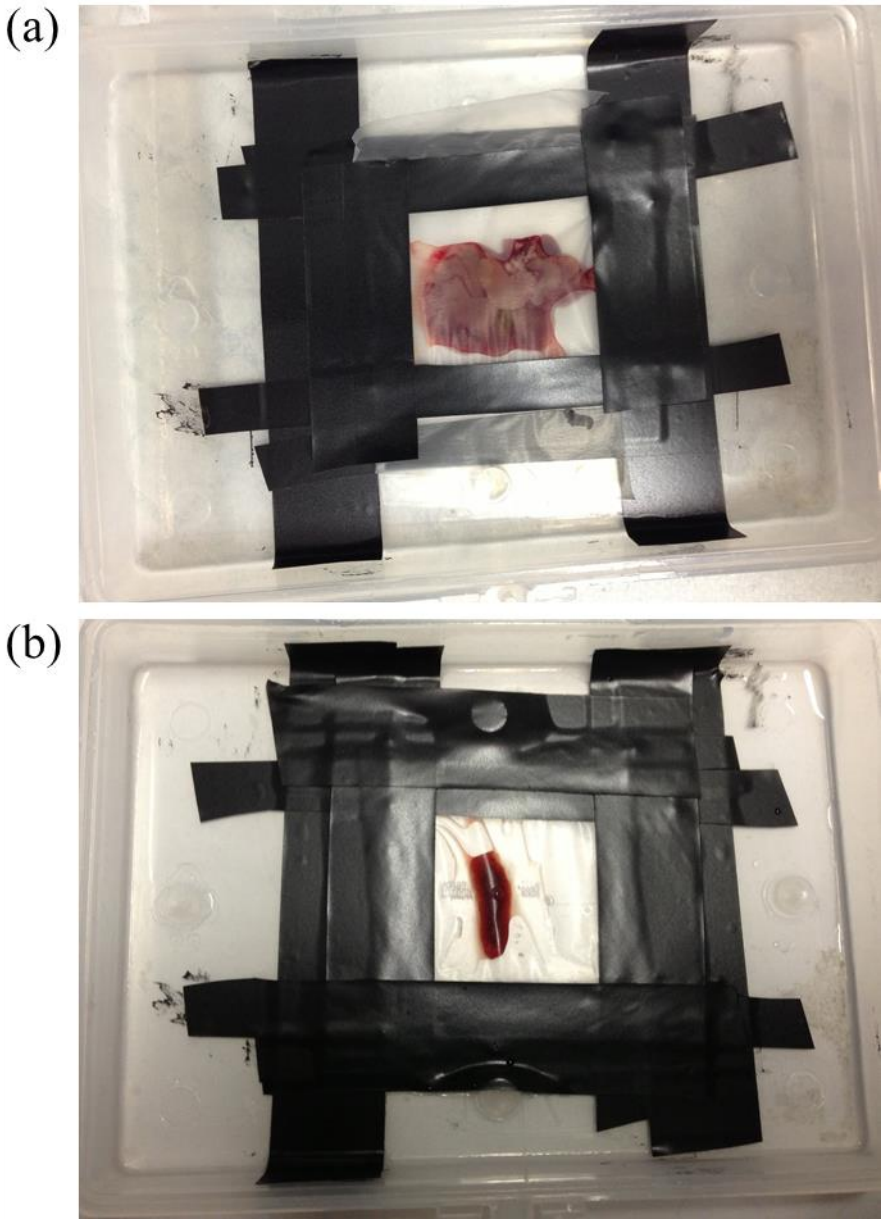

Figure 5-4 The mouse organ sample setup (a) liver and (b) spleen for *ex vivo* USF imaging.

5.3 Results and Discussion

5.3.1 One-color USF Microscopic Imaging in Centimeter-deep Silicone Phantoms

Figure 5-5 shows the USF image of a micro-tube embedded in a tissue-mimicking silicone phantom. The thickness of the phantom is 1.1 cm and the tube size is 310 μm of I.D. and 640 μm of O.D.. In this study, the tube was filled with aqueous solution of $ADP(CA)_2$ NCs. The FWHM of the USF image profile along the x direction at each y

location were calculated. The result indicates FD-USF imaging was successfully accomplished in centimeter-deep tissue-mimicking phantoms. The averaged FWHM at different y locations were 0.93 ± 0.07 mm. This image also shows an unprecedented SNR. Even without applying the correlation algorithm, the SNR is as high as 79.3, which is overwhelming than that of the CW USF image.

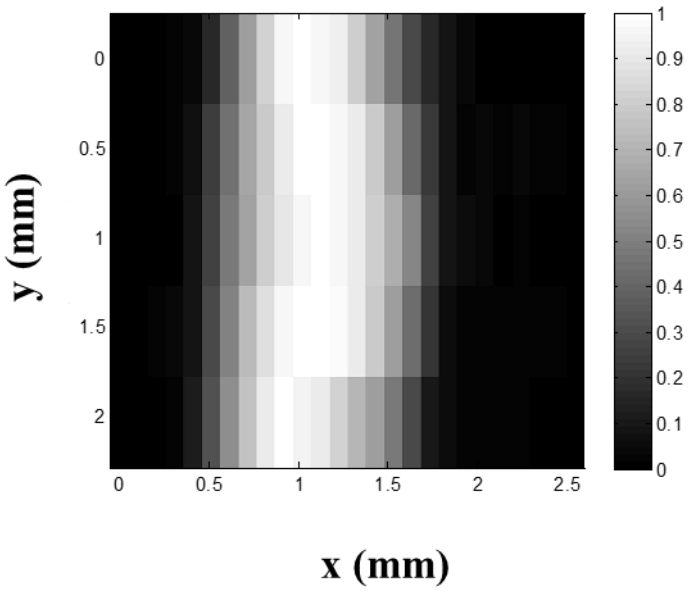

Figure 5-5 The USF image of the tube with inner diameter of 310 μm embedded into the phantom.

5.3.2 Multi-color USF Microscopic Imaging in Centimeter-deep Tissue Phantoms

5.3.2.1 Multi-color USF imaging by using different instrument setups with multiple scans

Two-color USF imaging was successfully performed. Figure 5-6 shows the two-color USF images obtained by two scans. Two different contrast agents were distinguished by using two channels, separately. By using $ADP(CA)_2$ setup, both tubes were imaged, as shown in Figure 5-6(a). In $ADP(CA)_2$ channel, the laser could excite both $ADP(CA)_2$ and ICG since ICG has a broad excitation/emission spectrum. When using ICG channel, the light source can only excite ICG. Thus in this case only the tube filled with ICG-based contrast agents was imaged (see Figure 5-6(b)). In the two-color USF images, the FWHM of the tubes are ~ 1 mm. However, the SNR is relatively poor. This is due to the experimental limitation (long time in scanning and changing setups) in the early stage of the USF exploration. The tissue was soaked in water for too long. Later on, I figured out a new method to achieve two-color USF imaging with less time and higher SNR.

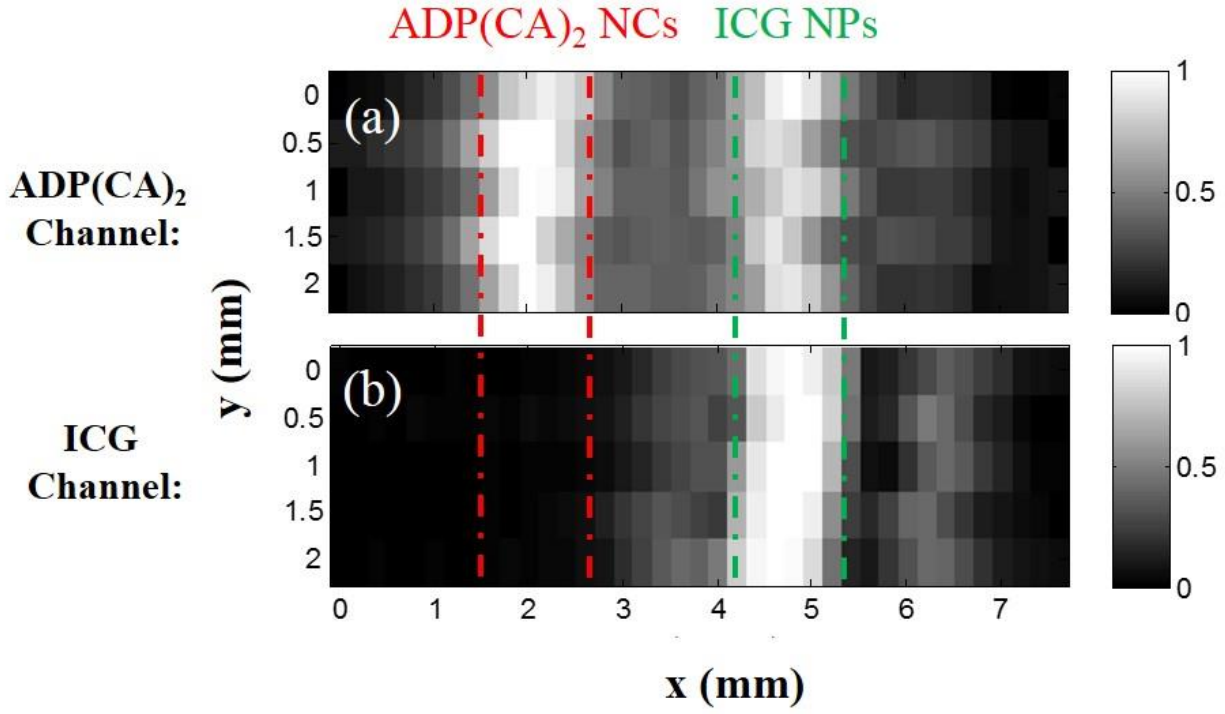

Figure 5-6 Two-color USF images. (a) The USF image when using $ADP(CA)_2$ channel setup; (b) shows the USF image when applying ICG channel setup.

5.3.2.2 Multi-color USF imaging by using same instrument setup with single scan via correlation

Five silicone micro-tubes (inner diameter: I.D.=0.31 mm; outer diameter: O.D.=0.64 mm) were inserted through the middle plane (x-y; z=6.5 mm) of a tissue-mimicking silicone phantom (μ_a=0.03; μ_s'=3.5 cm^{-1}; thickness=13 mm) (see details in Methods). Figure 5-7(a) shows two photographs (the front and back) of this phantom and the cross section of micro-tube structure on the x–y plane. These micro-tubes were filled with different contrast agents (see the caption of Figure 5-7(g)) and imaged using three modalities: diffuse fluorescence imaging (DF), USF, and ultrasound (US) (see details in Methods).

Figures 5-7(c) and 5-7(d) show the multi-color USF images of ICG NPs (color-1) and $ADP(CA)_2$ NCs (color-2), respectively, which can be acquired from a single scan using the same system (Ex:671 nm; Em:715 nm long-pass), but are differentiated using the correlation method (the spectrum crosstalk is eliminated). Figures 5-7(e) and 5-7(f) show the same USF images overlapped with the DF image. Compared with the DF image, the sizes of the tubes in

USF images are significantly reduced (FWHM=0.95 mm for the color-1 tubes and 0.88 mm for color-2 tubes) and much closer to the true size of the micro-tubes. All the individual micro-tubes can be clearly and correctly resolved.

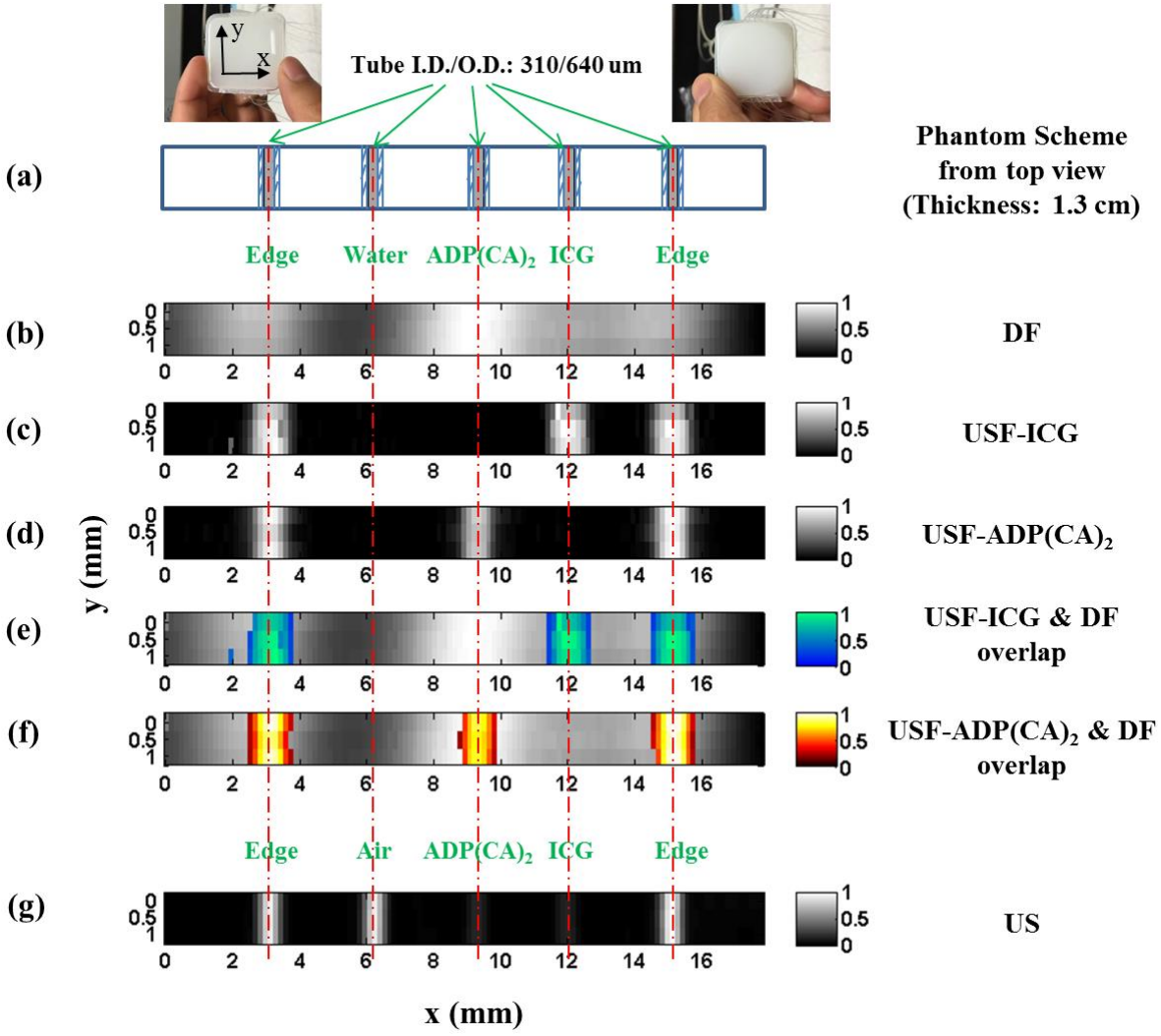

Figure 5-7 Images of micro-tubes in a tissue-mimic phantom. (a) The photographs and schematic diagram of the tissue-mimic silicone phantom (on x-y plane): front view (left photo), back view (right photo) and the cross section of the micro-tube structure on the x-y plane (the bottom figure in (a)). (b) The image acquired by directly detecting fluorescence (DF) without ultrasound. (c) and (d) show the USF images acquired from ICG-encapsulated PNIPAM NPs (color-1) and ADP(CA)$_2$-encapsulated Pluronic-F127 nanocapsules (color-2), respectively. (e) and (f) are the overlapped images between USF images ((c) and (d)) and direct fluorescence image (b). (g) Ultrasound image of the micro-tubes acquired from the same ultrasound transducer (i.e. a C-mode ultrasound image). The three non-edge

tubes were filled with water (as background control), ICG-based agent (color-1) and ADP$(CA)_2$-based agent (color-2). The two edged micro-tubes were used for image co-registration and were filled with the corresponding contrast agent of each modality (see Methods).

Current USF technology can sensitively and specifically detect USF fluorophores (ADP$(CA)_2$) with a concentration of ~50 μM at a depth of several centimeters (see Section 5.3.5.2), using a laser and a HIFU below the safety thresholds (laser intensity: 0.21–3.19 mW/cm^2; HIFU's mechanical index: 1.7 when imaging depth <30 mm, and 2.19 when imaging depth >30 mm). Because of the high spatial resolution and the adoption of micro-tubes, the ADP$(CA)_2$-occupied volume in a single voxel in this study is as small as ~68 nanoliters (assuming the volume is a cylinder with a diameter of 0.31 mm (I.D.) and a length of 0.9 mm (the FWHM of the USF image)). Thus, the corresponding number of ADP$(CA)_2$ molecules in this volume is as low as ~3.4 picomoles. By comparison, conventional fluorescence molecular tomography (DF-based imaging) detects with difficulty <10 picomole molecules of a commercially available dye (AF680) in a mouse phantom at a depth of 11 mm (i.e., a thickness of 22 mm when converting into a transmission geometry) [95]. In FD-USF imaging, further decreasing the concentration of the USF agents is possible but sacrifices intensity and SNR. For example, when the agent's concentration drops to 50%, the fluorescence intensity decreases 44% and the SNR decreases 32%.

5.3.3 Validation via Diffuse Fluorescence Imaging

Figure 5-7(b) shows the image acquired from DF. The DF images of the tubes are significantly blurred because of the phantom's strong light scattering. The estimated FWHM is ~5 mm for the ADP$(CA)_2$ NCs-filled tube (i.e., the third tube). Spatially differentiating the ADP$(CA)_2$ NCs-filled tube from the ICG NPs-filled tube (i.e., the third and fourth tube) is difficult. In addition, the spectrum overlap makes both ADP$(CA)_2$ NCs- and ICG NPs-filled tubes visible in the image, no matter which emission filters are used (e.g., 715 nm long-pass (Figure 5-7(b)) or 711/25 nm band-pass (Figure 5-6(a))).

5.3.4 Validation via Ultrasound Imaging

Figure 5-7(g) shows the ultrasound image acquired using the same US transducer. The tube size (FWHM=0.5 mm) represents the spatial convolution of the transducer's acoustic focus (lateral FWHM=0.42 mm) with the top inner boundary between the silicon and the liquid (the specific size of the boundary is unknown but should be <I.D.=0.31 mm). As expected, the ADP$(CA)_2$ NCs- and ICG NPs-filled tubes show much lower acoustic contrast than the air-

filled tubes and they cannot be differentiated from each other because the acoustic wave is insensitive to fluorophore molecules.

For better comparison, Figure 5-8 displays the normalized profiles along the x-axis acquired from different imaging modalities (i.e., the cross section of the five micro-tubes in the silicone phantom). The images acquired with US and DF verified the feasibility of USF imaging regarding of target location, size, and shape. Meanwhile, compared with the traditional DF imaging (at centimeters depth), USF improves the spatial resolution >5 times using current setup (2.5 MHz ultrasound). The current system's resolution is limited mainly by thermal diffusion, but in the future, microscopically heating the contrast agents to achieve thermal confinement can further increase it. Once thermal confinement is achieved, adopting an ultrasound transducer with a higher frequency and a smaller f-number can further significantly increase the resolution.

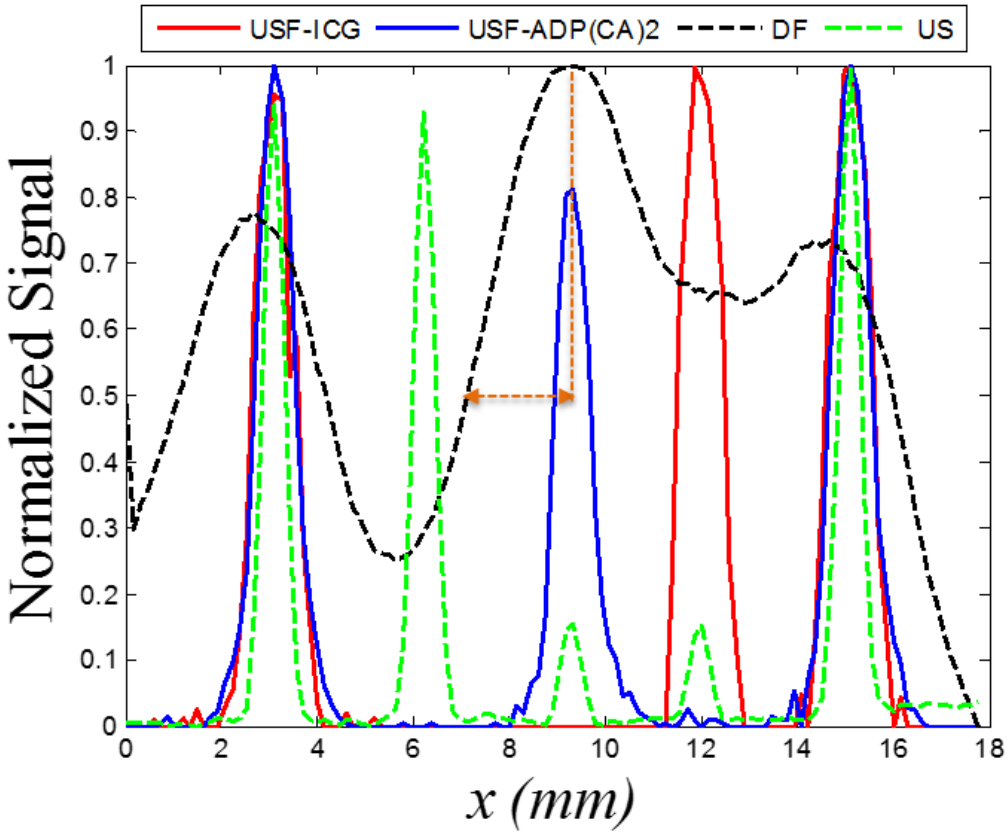

Figure 5-8 The normalized profiles of Figure 5-7 along x-axis acquired from different imaging modalities (i.e. the cross section of the five micro tubes in the silicone phantom). Due to the significant overlap of the tube profiles in the DF image, the two dotted brown lines are used to show how FWHM of the central tube in the DF image (the

dashed black line) is estimated. The horizontal dashed brown line with double arrows represents ½ of the FWHM that is ~2.5 mm and therefore the estimated FWHM is ~5 mm.

5.3.5 USF Microscopic Imaging in Porcine Muscle Tissues with Different Thicknesses

5.3.5.1 Reason of choosing porcine muscle tissue

Table 5-1 shows the optical properties of porcine muscle, human arm, and human breast tissue at excitation wavelength of 671 nm. The optical properties of porcine muscle used in our experiments (u_a and u_s') are nearly twice less than those of a human arm. However, because our current laser intensity (0.21-3.19 mW/cm^2) is well below the ANSI safety threshold, we can increase the laser energy to compensate for the signal attenuation caused by large tissue absorption and scattering coefficients when we perform USF on living animals or human beings. To characterize the required laser enhancement, we performed a Monte Carlo simulation, the results are shown in Figure 5-9. For instance, to gain the same fluence at different depth in arm tissue, one can increase the laser energy 1.61-fold at 1 cm, 1.32-fold at 2 cm, and 1.35-fold at 3 cm. Similarly, when imaging breast tissues, one should increase the laser energy 1.26-fold at 1 cm, 1.35-fold at 2 cm, and 1.33-fold at 3 cm.

Note that another reason that we selected porcine muscle tissue as the tissue phantom for USF imaging is due to its acoustic property. In ultrasound-related studies such as photoacoustic imaging [96], sonography [97], and intense ultrasound energy delivery [98], porcine muscle tissue was frequently used.

Table 5-1 Optical property summary of porcine muscle, human arm, and human breast

Sample	**μ_a (cm^{-1})**	**μ_s' (cm^{-1})**
Porcine muscle	0.06	2.7
Human arm	0.12	5.8
Human breast [99]	0.037-0.11	11.4-13.5

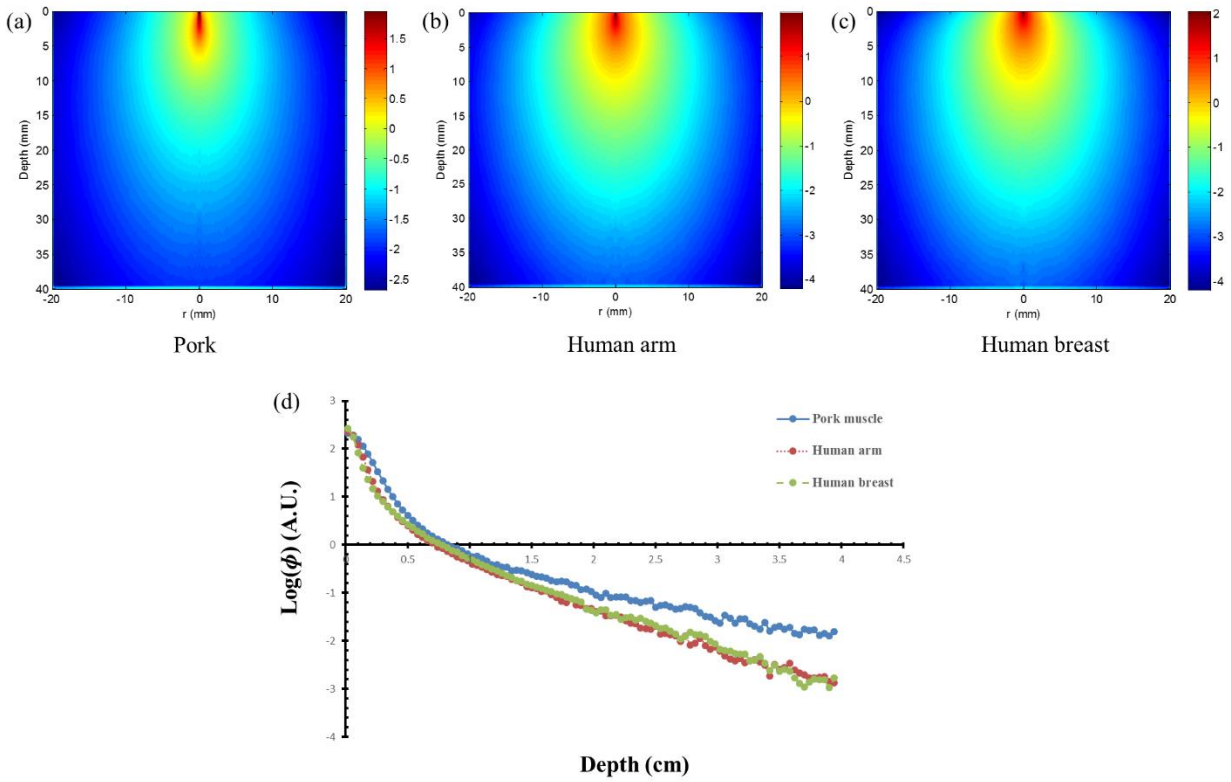

Figure 5-9 Monte Carlo simulation of (a) pork muscle, (b) human arm and (c) human breast. The parameters used in this simulation are: μ_a: 0.06, 0.12 and 0.06 cm^{-1}, μ_s': 2.7, 2.8 and 12 cm^{-1} and g: 0.9, 0.9 and 0.9 in an order of (a), (b) and (c). (d) plots the relationship between fluence and penetration depth.

5.3.5.2 USF microscopic images with imaging depth breakthrough of three centimeters

We used porcine muscle tissue (μ_a=0.06; μ_s'=2.7 cm^{-1}) in the USF experiments because of its reasonable acoustic properties and optical properties (see Section 5.3.5.1). Figures 5-10(a–d) show the USF images of micro tubes that are inserted into porcine muscle tissue with different thickness (0.8, 1.2, 2.2, and 3.1 cm). Figures 5-10(e–h) show the corresponding images processed with the correlation algorithm. All the micro-tubes can be clearly imaged with a similar FWHM (~1.1 mm) and the spatial resolution does not degrade when the thickness increases.

Figure 5-11 plots the SNR as a function of the tissue thickness. Significantly high SNRs have been achieved (17.6–242 after and 18–104 before the algorithm processing). The fitted attenuation coefficient of the SNR versus the tissue thickness (0.756 and 1.049 cm^{-1} before and after the algorithm processing) is slightly smaller or close to the average effective optical attenuation coefficient of porcine muscle tissue ($\mu_{eff} \approx 1$ cm^{-1} for 670–900 nm) [100]. This

result indicates that (1) the tissue's optical attenuation is primarily responsible for the SNR reduction as the thickness increases and, (2) increasing the illumination energy of the light and/or ultrasound in thicker tissue can compensate for the tissue's optical attenuation.

For comparison, we also measured SNRs for ICG-based contrast agents. When tissue thickness is <2 cm, SNRs of USF signals acquired from ADP$(CA)_2$-based agents are ~3–5 times higher under similar experiment conditions. This improvement is not as high as the improvement in their ON-to-OFF ratios (I_{ON}/I_{OFF}), primarily because the background noise in USF imaging originates from multiple sources, such as the laser leakage, autofluorescence, and emission from non-100%-OFF fluorophores. Beyond 2 cm, only the ADP$(CA)_2$-based agent, because of its high I_{ON}, is capable of imaging the 310μm micro-tube.

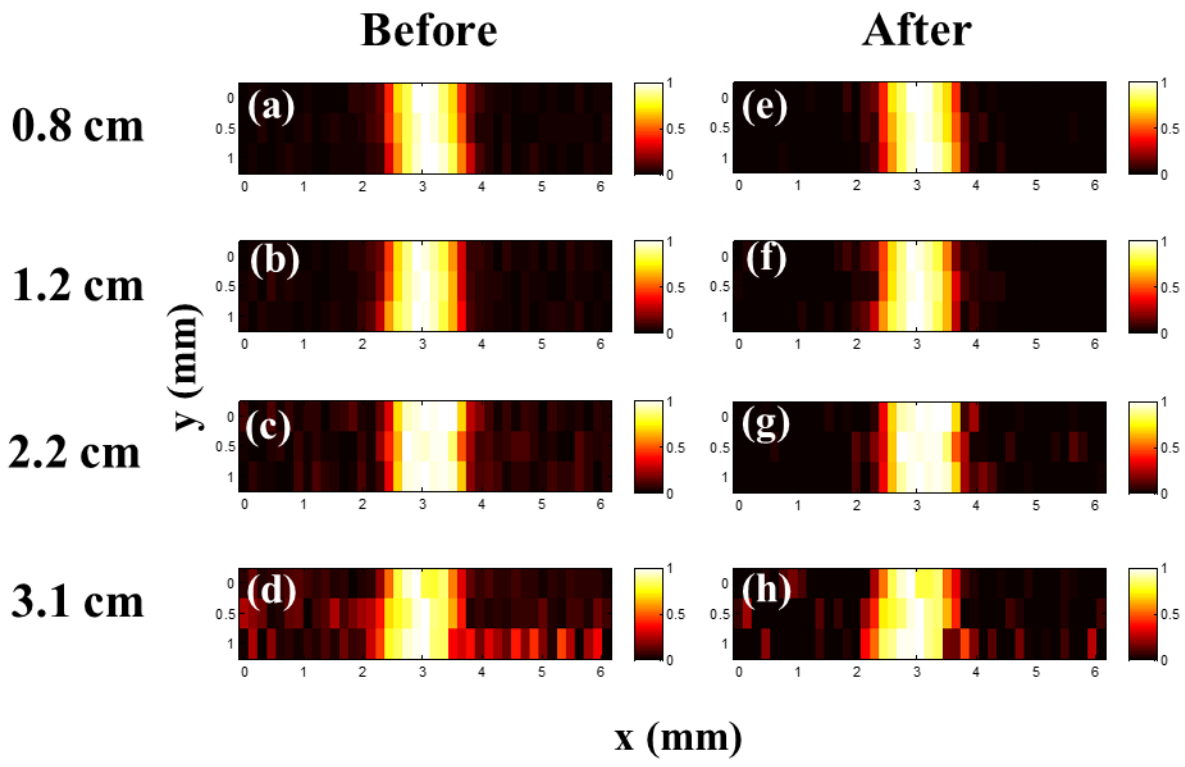

Figure 5-10 USF images of micro tubes in porcine muscle tissue samples. (a)-(d) The USF images of the micro tubes (before correlation) that were embedded into pork muscle tissue samples with thicknesses of 0.8, 1.2, 2.2 and 3.1 cm, respectively. The I.D./O.D. of the tube is 0.31/0.64 mm; (e)-(h) The corresponding USF images processed by the correlation algorithm.

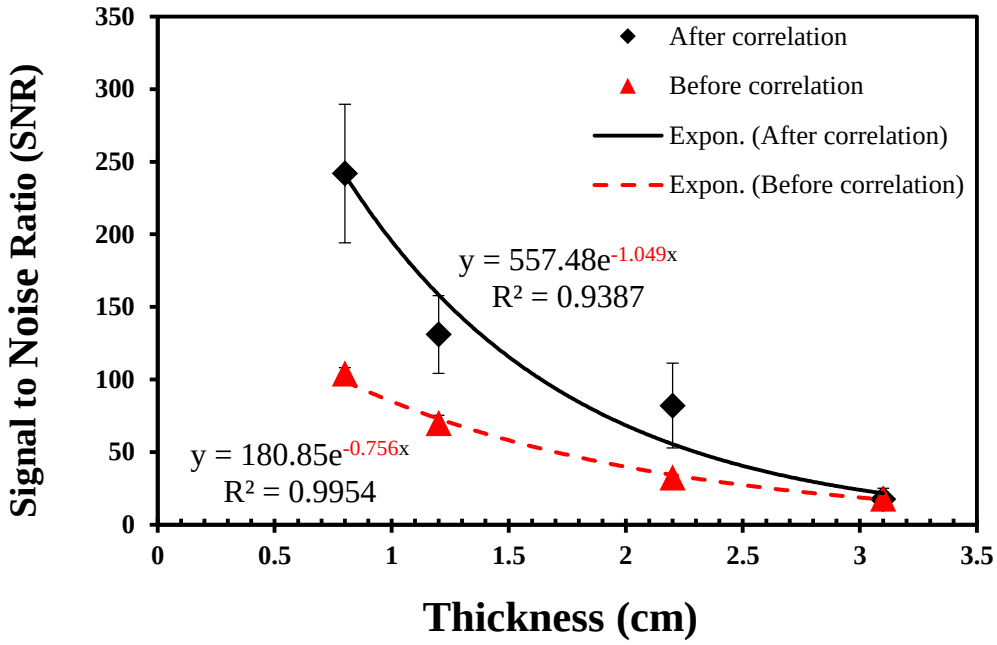

Figure 5-11 The relationship between the SNR and the thickness of the sample before (triangles) and after (diamonds) the correlation processing (error bar: mean ± standard deviation).

5.3.5.4 The effect of LIA time constant

Figure 5-12 plots the SNR as a function of the LIA's time constant (tissue thickness=12 mm). If we do not apply the correlation algorithm, the SNR increases from 29.9–87.9 when the time constant increases from 3–300 ms (See red dashed line in Figure 5-12). The correlation algorithm dramatically improves the absolute values of SNRs (between 95.4–215.6). The correlation method seems more efficient for short time constants (see black solid line in Figure 5-12). This is useful to improve USF imaging speed in the future by shortening the time constant without SNR degradation.

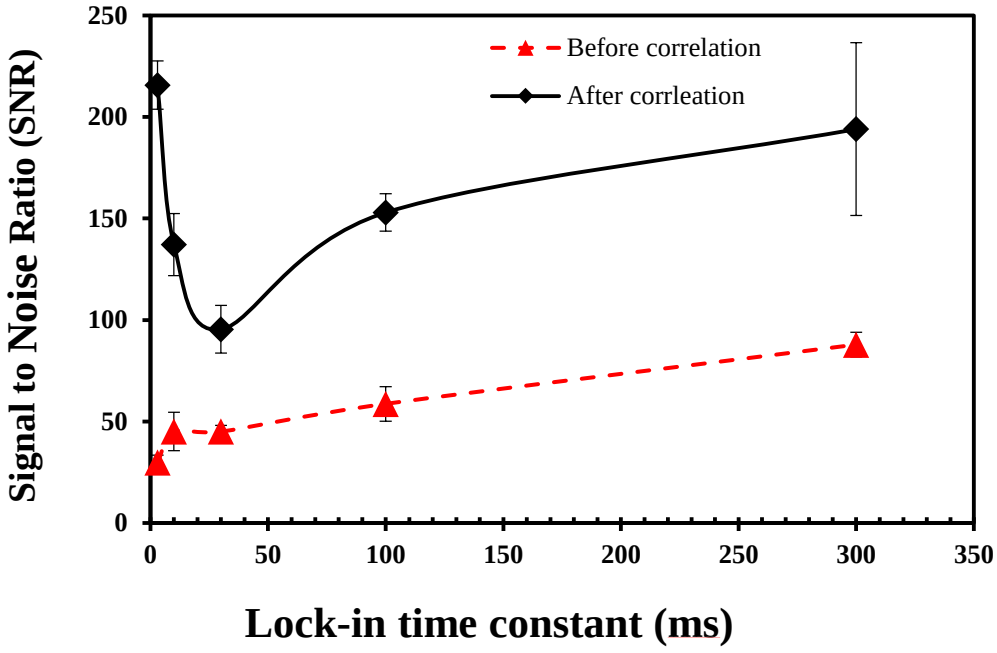

Figure 5-12 The relationship between the SNR and the LIA time constant before (triangles) and after (diamonds) the correlation processing (error bar: mean ± standard deviation).

5.3.6 USF Microscopic Imaging in ex vivo Mouse Organs

About 100 μl aqueous solution of the USF contrast agent ($ADP(CA)_2$-encapsulated NCs with a concentration of 16.3 mg/ml) was intravenously injected into a mouse via a tail vein. After 24 hours, the mouse was sacrificed and the organs were isolated. To demonstrate USF microscopic imaging, a corner of the liver and a part of the spleen were scanned. Figure 5-13 and Figure 5-14 show the USF microscopic images of liver and spleen on the x-y plane, respectively. The corresponding white-light photos are also shown on the right side of their USF images. The green square (7.62×7.62 mm^2) in Figure 5-13 and the green rectangle (1.016×15.24 mm^2) in Figure 5-14 indicate the USF scanning areas. The red and yellow areas in the USF images may represent some blood vessels or microstructures inside the organ that cannot be seen from their white-light photos. Note that the USF images represent a projection of the distribution of the USF contrast agents on the x-y plane along the z-axis (i.e., the ultrasound axis).

Typical USF signals and background signals inside mouse organs are shown in Figure 5-15. Similar to previous results, the contrast agents' dynamic curve shows a specific temporal pattern and is different from the background noise. However, unlike *in vitro* tissue phantom experiments with a tube model, the typical USF signal is

no longer the same as shown in Chapter 4, which is a positive signal. On the contrary, as shown in Figure 5-15(a) and (c), when the ultrasound pulse is applied, a negative USF signal was generated wherein the USF contrast agents exist. The mechanism of this phenomenon is unclear. But it may be caused by the interaction of the USF agents with the biological environment. More experiments and discussion will be conducted in next chapter.

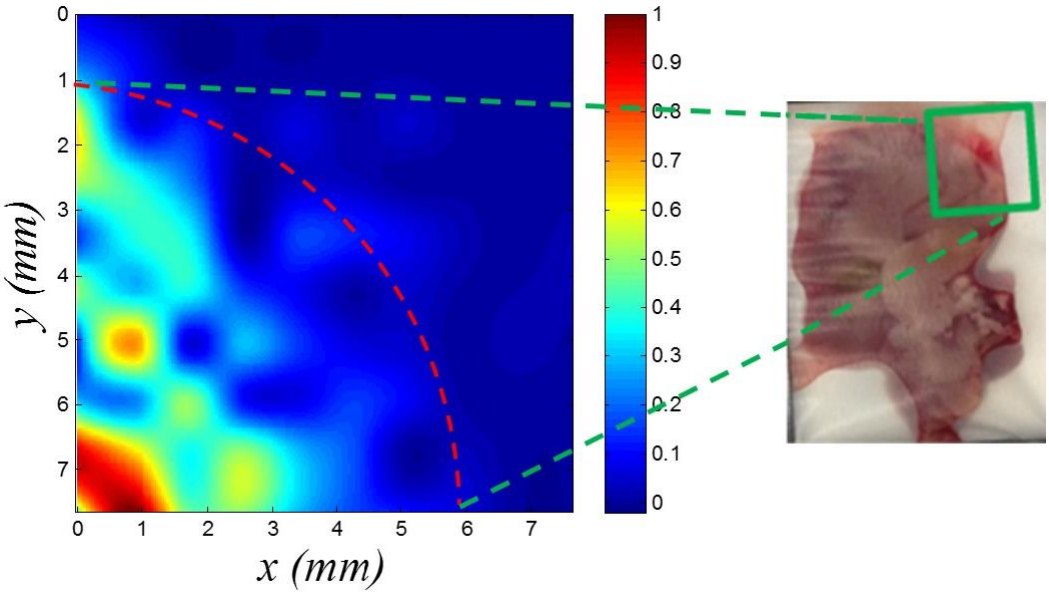

Figure 5-13 An USF image and a white-light photo of an *ex vivo* mouse liver.

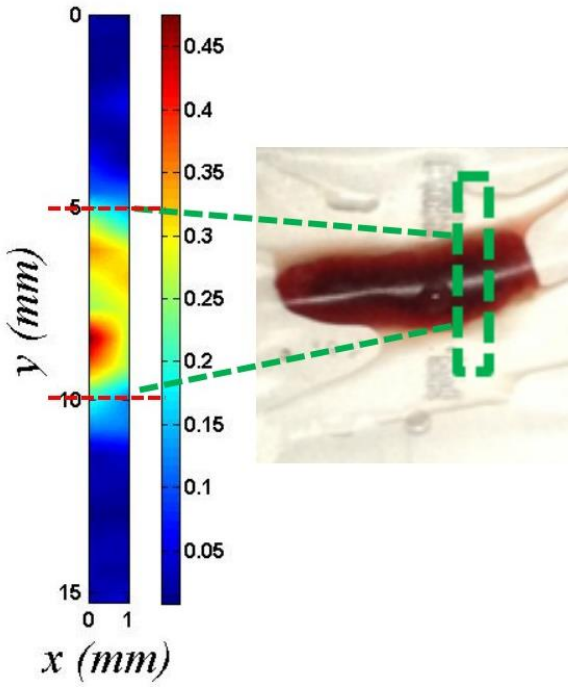

Figure 5-14 An USF image and a white-light photo of an *ex vivo* mouse spleen.

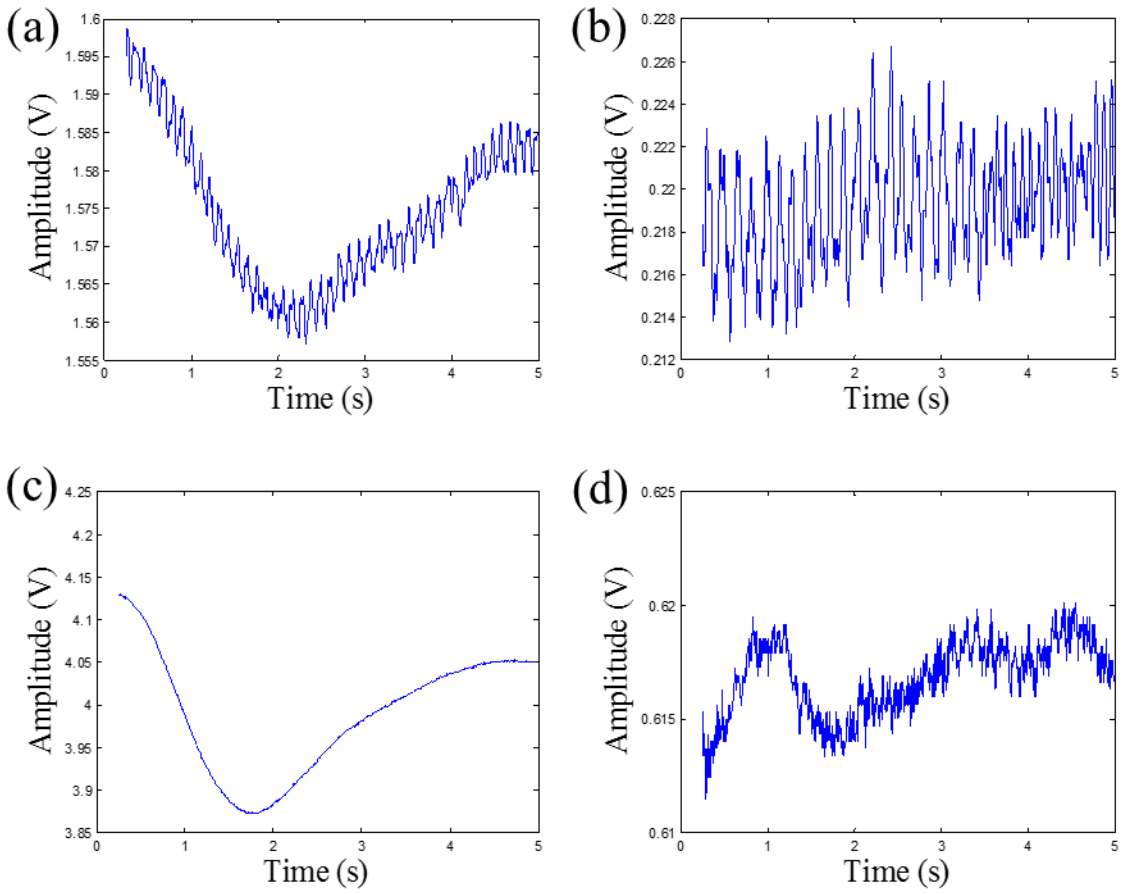

Figure 5-15 Typical USF signals and background noise in *ex vivo* mouse organs. (a) and (b) showing USF signals and background noise of ADP$(CA)_2$ NCs in mouse liver. (c) and (d) showing USF signals and background noise of ADP$(CA)_2$ NCs in mouse spleen.

5.4 Conclusion

In this chapter, we have successfully achieved fluorescence microscopic imaging in centimeter-deep tissues with high SNR and picomole sensitivity using a laser and an ultrasound pulse below the safety thresholds. The spatial resolution has been significantly improved compared with DF imaging while the imaging depth can reach several centimeters. Multiplex USF imaging is also demonstrated. This will be very useful in simultaneously imaging multiple targets and their interactions in the future, which are usually difficult for non-optical technologies. Also, this technology is demonstrated for the first time in both tissue-mimicking phantoms and real biological tissues including porcine muscle tissue and *ex vivo* mouse organs.

Chapter 6

Feasibility of USF in Animal Studies *In vivo*

6.1 Introduction

Biomedical imaging has played an important role in cancer diagnosis in the recent decades [3], [101]. Computed tomography (CT), magnetic resonance imaging (MRI), sonography, positron emission tomography (PET), and optical imaging are commonly used imaging modalities in *in vivo* tumor detection and staging. Among them, CT, MRI, and sonography have good spatial resolution and large imaging depth, however, they have drawbacks in sensitivity, specificity and capability of multiplex imaging. PET, as a nuclear imaging method, has a very high sensitivity and large imaging depth, however, it lacks both spatial resolution and temporal resolution. CT and PET are also relatively expensive and use ionizing radiation. MRI is also very expensive and data acquisition is very slow. Compared with these technologies, fluorescence imaging stands out in the following respects [16]–[19]: high sensitivity, low cost, use of non-ionizing radiation, the feasibility of multi-wavelength imaging, and the feasibility of tissue structural, functional, and molecular imaging. However, due to the strong light scattering, it is extremely difficult to achieve high spatial resolution in deep tissue *in vivo*. For instance, fluorescence microscopy can provide subcellular resolution but is limited with shallow imaging depth (hundreds of microns). Fluorescence diffuse optical tomography can reach several centimeters deep in tissue but is limited in the spatial resolution (several millimeters). Thus, *in vivo* high-resolution tumor imaging via fluorescence in centimeter-deep tissue has not been achieved.

Recently, we developed a new imaging technique named ultrasound-switchable fluorescence (USF) which takes the advantages of both ultrasound and fluorescence imaging. It is a cost-efficient imaging method. This technique has been demonstrated to achieve microscopic imaging in centimeter-deep tissue with high SNR and sensitivity in tissue-mimicking phantoms and *ex vivo* biological tissues in Chapter 5. It is necessary to evaluate its *in vivo* feasibility. In this chapter, we first built up an *in vivo* USF imaging system. Then we performed USF imaging in both heathy mouse tissues and mouse tumors to demonstrate its *in vivo* feasibility. Two different injection methods (intravenous and local injections) were adopted and two different types of contrast agents with both low and high LCSTs were tested: ADP$(CA)_2$-encapsulated Pluronic-F127 NCs (LCST: 23 °C) and ICG-encapsulated P(NIPAM-AAm 90:10) NPs (LCST: 39 °C). High-resolution *in vivo* USF images were acquired from mouse mammary tumors.

6.2 Materials and Methods

6.2.1 In vivo USF Imaging System Setup

For *in vivo* studies, first an animal subsystem was built up, including an anesthesia system and a physiological monitoring system. Figure 6-1 shows the major parts. An oxygen concentrator (Figure 6-1(B), Scivena Scientific, Clackamas, OR, USA) which can extracts medical-grade oxygen from air and up to 5 l/min flow was connected to an isoflurane vaporizer (Scivena Scientific, Clackamas, OR, USA). The vaporizer has two outlets which were connected to an animal chamber and a nose cone. The physiological monitoring system includes a pulse oximeter and heart rate monitor (Kent Scientific Corporation, Torrington, CT, USA) and temperature monitoring and hemeothermic control system (Kent Scientific Corporation, Torrington, CT, USA). The later contains two temperature sensors and one warming pad. Then the animal system was incorporated with the FD-USF imaging system described in Chapter 4, for the purpose of *in vivo* USF studies.

6.2.2 In vivo USF Signal Detection from a Mouse

FVB/N mice (female, 20–25 gram) were purchased from Jackson Lab (Bar Harbor, ME, USA). The animal protocols were approved by the University of Texas at Arlington's Animal Care and Use Committee. Animals were anesthetized with a mixture of 2%–2.5% isoflurane and 1–2 l/min of 100% oxygen. A pulse oximeter was attached to the animal's paw to monitor heart rate and oxygen saturation, and a rectal temperature probe (attached to a homeothermic control blanket) was used to record and maintain core body temperature. Hair on the back and abdomen was removed using an animal trimmer and depilatory cream (VEET sensitive formula, Reckitt Benckiser, Parsippany, NJ, USA). After preparation, the animal was transferred to the FD-USF system. In this study, 100 µL final solution of the ADP$(CA)_2$-encapsulated Pluronic-F127 NCs was injected through a tail vein. The basic experiment setup of the animal in USF signal detection was shown in Figure 6-2. A nose-cone was placed over the animal's nose to deliver inhalant anesthetic. The HIFU beam is aligned with the photon collection fiber bundle. The focus of the HIFU was positioned into the mouse. Two hours later, *in vivo* USF signal was acquired. All USF system parameters were the same as those in the 12-mm thick tissue sample USF imaging described in Chapter 5, except that the HIFU driving voltage was changed from 80 mV to 400 mV due to the significant dilution of the fluorophore concentration after injecting into a large volume (animal body) and possible thermal loss due to blood perfusion in a living animal.

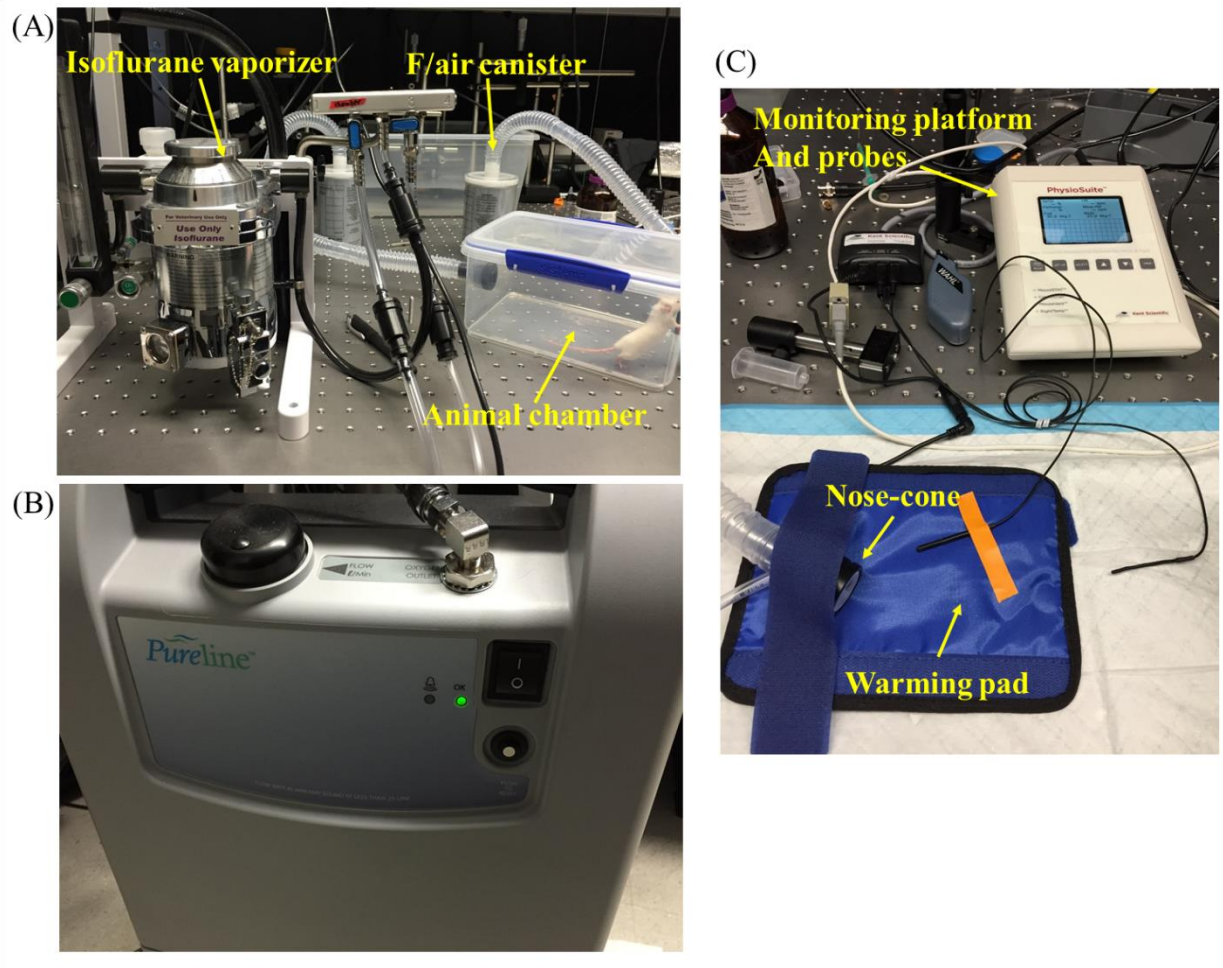

Figure 6-1 The system for animal studies. (A) Isoflurane vaporizer connected to an animal chamber. (B) Oxygen concentrator connected to the isoflurane vaporizer. (C) Physiological monitoring system including: a platform, three probes, and a warming pad.

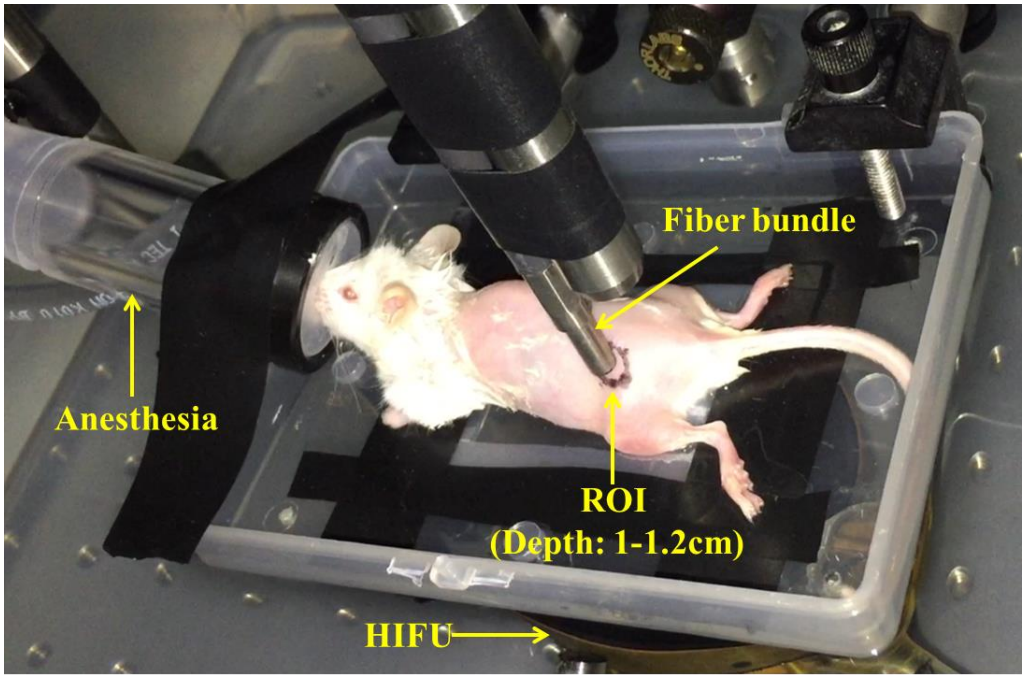

Figure 6-2 A photo to show the basic experiment setup of *in vivo* USF signal detection.

6.2.3 In vivo USF Mouse Tumor Imaging

FVB/N-Tg(MMTVneu)202Mul/J mice (female, 20–25 gram, n = 9) were purchased from Jackson Lab (Bar Harbor, ME, USA). The animal protocols were approved by the University of Texas at Arlington's Animal Care and Use Committee. Animals were anesthetized with a mixture of 2%–2.5% isoflurane and 1–2 l/min of 100% oxygen. A pulse oximeter was attached to the animal's paw to monitor heart rate and oxygen saturation, and a rectal temperature probe (attached to a homeothermic control blanket) was used to record and maintain core body temperature. Hair on the tumor was removed using an animal trimmer and depilatory cream. After preparation, the animal was transferred to the FD-USF system. The animal setup is shown in Figure 6-3. The excitation light was illuminated from the bottom of the tumor and the emission light was collected from the top of the tumor, respectively. The ultrasound transducer was placed below the tumor and focused inside the tumor at a depth of the half thickness of the tumor. In this study, 200 µL final solution of the ADP$(CA)_2$-encapsulated Pluronic-F127 NCs or ICG-encapsulated P(NIPAM-AAm 90:10) NPs were locally injected into the tumor. After one hour, USF images were acquired.

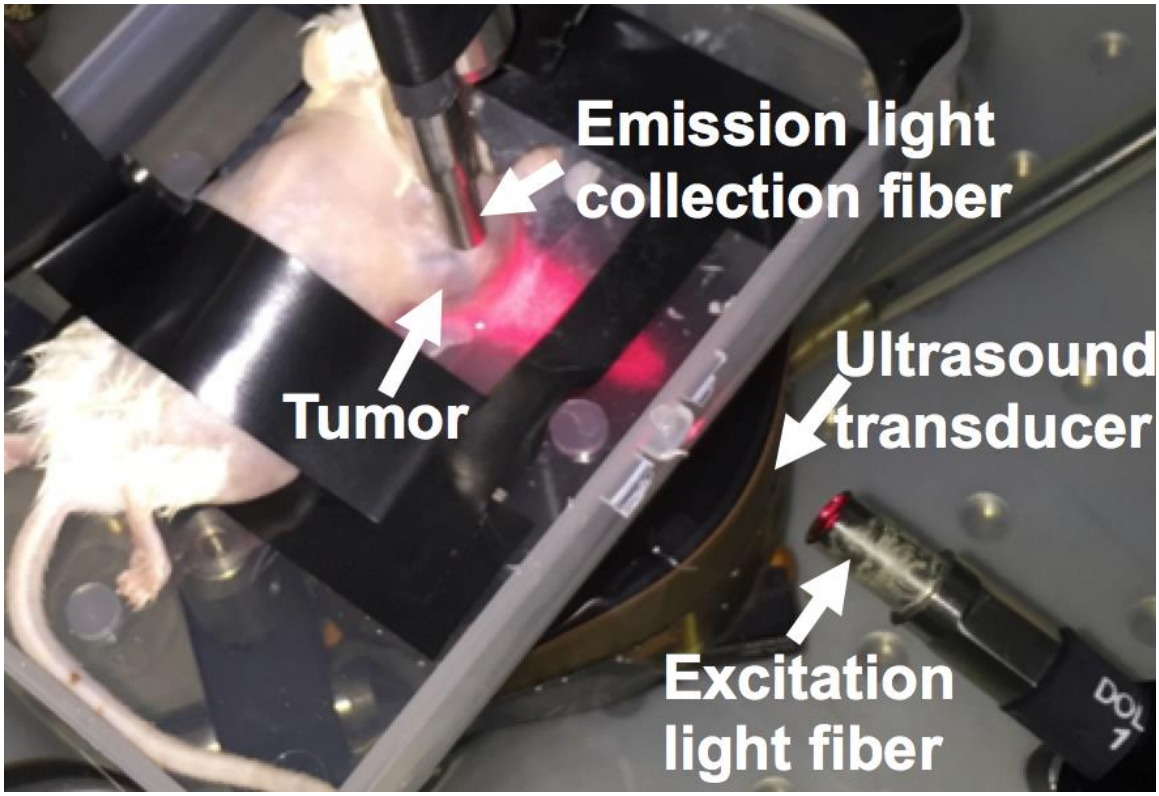

Figure 6-3 A photo to show the basic experiment setup of *in vivo* tumor USF imaging.

6.2.3.1 Tumor USF imaging setup for ADP$(CA)_2$-based contrast agents

The excitation light source is a diode laser with a wavelength of 671 nm (MLL-FN-671). A 673/11 nm band-pass filter (central wavelength: 673 nm; bandwidth: 11 nm) was applied as the excitation filter and three 715 nm long-pass interference filters (cutoff wavelength: 715 nm) and two long-pass absorptive filters (edge wavelength: 695 nm) were used as the emission filters.

6.2.3.2 Tumor USF imaging setup for ICG-based contrast agents

The excitation light source is a diode laser with the excitation wavelength of 808 nm; Two long-pass interference filters (edge wavelength: 830 nm) and two long-pass absorptive glass filters (edge wavelength: 830 nm) were used as the emission filters.

6.3 Results and Discussion

6.3.1 Detection of the in vivo USF Signal

As shown in Figure 6-2, the HIFU beam is aligned with the photon collection fiber bundle. The focus of the HIFU is positioned inside the mouse body (~5 mm higher from the bottom of the mouse). The mouse thickness at that location is 10-12 mm. The *in vivo* USF signal was observed and is plotted in Figure 6-4. The open vertical (red) line represents that ultrasound is off, and the three solid vertical (red) lines indicate that three ultrasound pulses are delivered to the animal. Clearly, once an ultrasound pulse is applied, a USF pulse is generated (the blue line). Similar to the USF signal in *ex vivo* mouse organs, the *in vivo* USF signal is also a negative signal. This negative USF pulse relative to the baseline may be caused by the interaction of the USF agents with the *in vivo* biological environment.

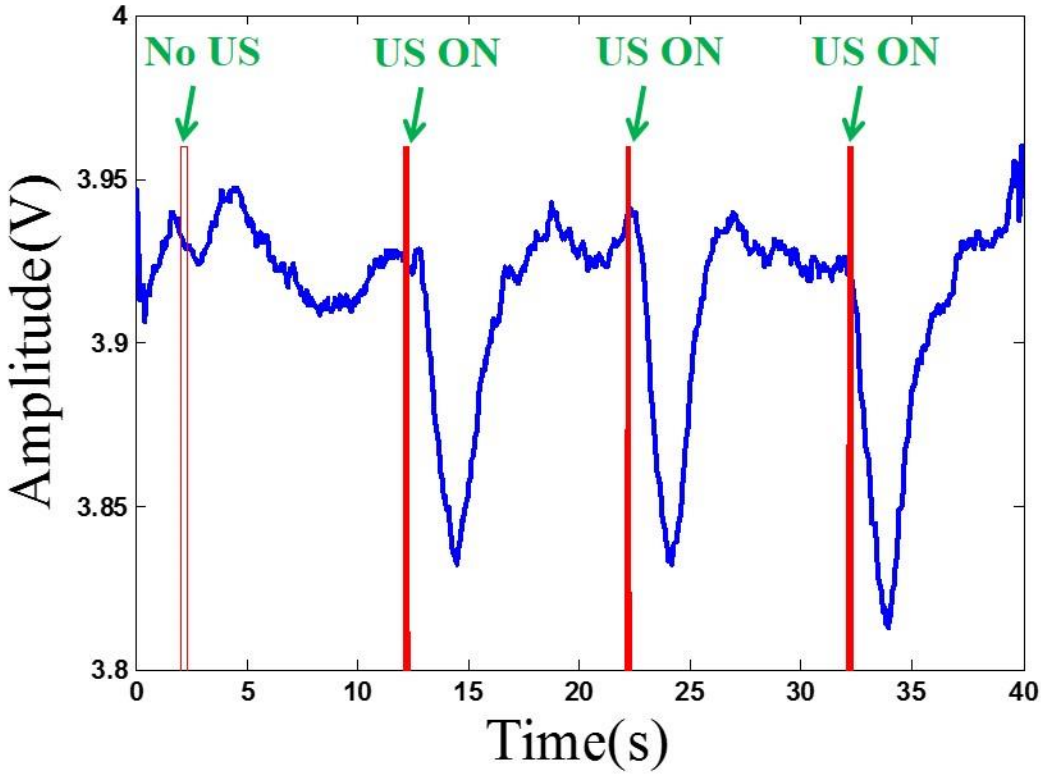

Figure 6-4 The acquired *in vivo* USF signal (the blue line) and the corresponding ultrasound exposure (the three sold red lines). The open red line represents no ultrasound pulse is applied.

The mechanism of generating negative USF signal from the adopted low-threshold agents may be due to the interaction of $ADP(CA)_2$ molecules with biomolecules (such as proteins) either inside or outside the nanocapsules. Two hypotheses are discussed here. (1) When USF contrast agents were intravenously injected into the mouse body, some biomolecules or proteins may bind to the fluorophores ($ADP(CA)_2$) inside the nanocapsules, changing the

microenvironment of the fluorophores and significantly increasing the fluorescence intensity. This increase may be even stronger than the fluorescence increase caused by the shrinkage of the nanocapsules when they are exposed to temperatures above the threshold. After firing an ultrasound pulse, the nanocapsules shrink and expel the biomolecules. As a consequence, the fluorescence intensity drops. (2) After several hours of intravenous injection of the agents, because the mouse body temperature (~37 ˚C) is higher than the agent's threshold (~23 ˚C), some $ADP(CA)_2$ molecules may be gradually released from the nanocapsules while others may remain inside. If $ADP(CA)_2$ molecules have a chance to attach to a protein, they emit strong fluorescence because of the decrease of the local polarity. The emitted signal will decrease if the ultrasound-induced temperature or ultrasound-induced mechanical effect is somehow unfavorable for the fluorophore-protein interaction, which forms the observed negative USF signal in a biological environment. More detailed studies will be conducted in the future.

6.3.2 High-resolution in vivo USF Imaging of a Large Mouse Tumor

In this study, different types of USF contrast agents with low (< 37°C) and high (> 37 °C) temperature thresholds were used in this study, including: $ADP(CA)_2$-encapsulated Pluronic-F127 NCs and ICG-encapsulated P(NIPAM-AAm 90:10) NPs. In the experiment, 200 µL final solution of the contrast agent was injected locally into the tumors. To make sure the contrast agents were injected into the tumor successfully and the emission light collection fiber is at the right position (i.e., cover the injection area), the fluorescence signals before and after the injection were recorded. Then the USF imaging was performed.

6.3.2.1 *In vivo* tumor USF imaging using $ADP(CA)_2$ NCs

Figure 6-5 shows the background fluorescence signal in the tumor region before and after injecting the contrast agents. The blue line is the PMT output which indicates the fluorescence signal acquired by the collection fiber. From this signal, we can verify that the excitation laser was modulated at 1 KHz. The yellow line represents the phase-locked reference signal for the lock-in amplifier with the same frequency. Before injection, shown in Figure 6-5, the peak-to-peak signal strength of the PMT output is 26 mV, which is mainly contributed from autofluorescence and laser leakage. It increased to 352 mV (13.5-fold) after injecting $ADP(CA)_2$ NCs, which means the contrast agents were injected successfully.

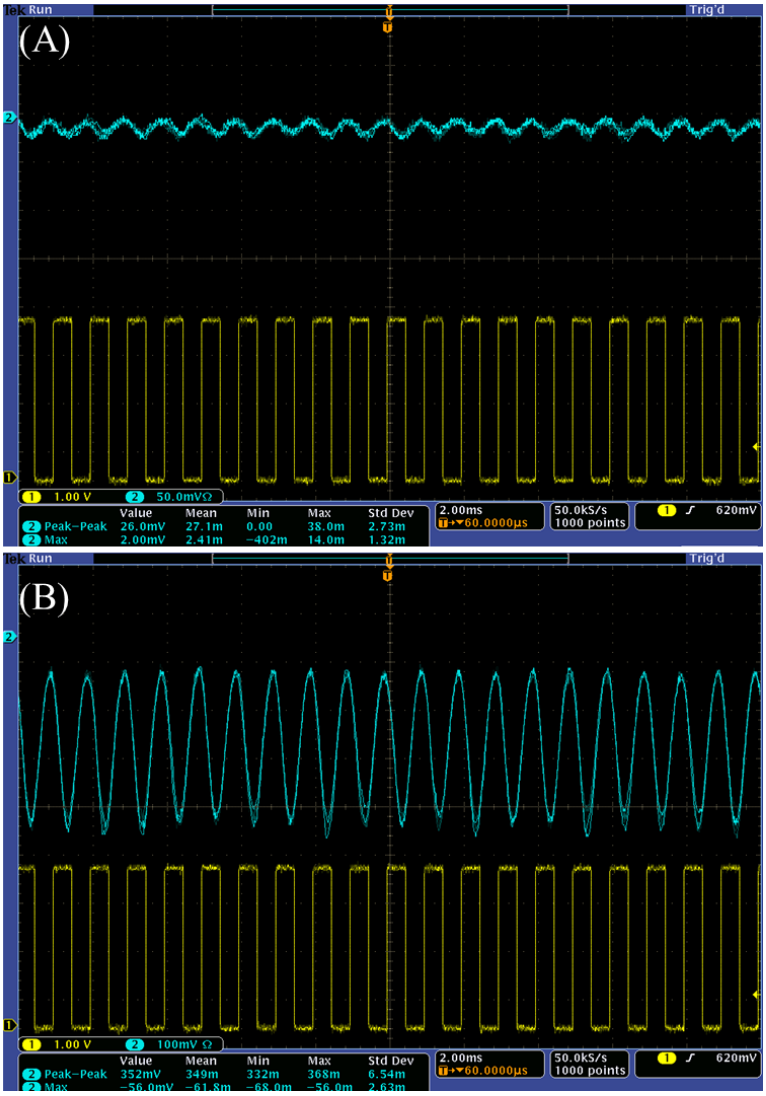

Figure 6-5 (A) The background fluorescence signal without injecting $ADP(CA)_2$-based agents. (B) The fluorescence signal after injecting 200 µL $ADP(CA)_2$-based agents.

After one and half hours, the *in vivo* high-resolution USF image was acquired in a mammary tumor and shown in Figure 6-6(B). The corresponding white-light photo of the tumor is shown in Figure 6-6(A). The ultrasound transducer was located below the tumor and focused inside the tumor around the half of the thickness of the tumor. The red square shown on the white-light photo schematically indicates the USF scanning area (x-y: 2.54×2.54 mm^2). Note that the red square cannot be used as the scale bar. Therefore, the acquired USF image presents an image on the x-y plane in the middle of the tumor. After processing the raw data, signals with specific USF temporal pattern were identified. This indicates the USF image is representing the distribution of USF contrast agents rather than some

random noise. Clearly, this USF image provides some *in vivo* micro-information with high spatial resolution that cannot be seen from the white-light photo.

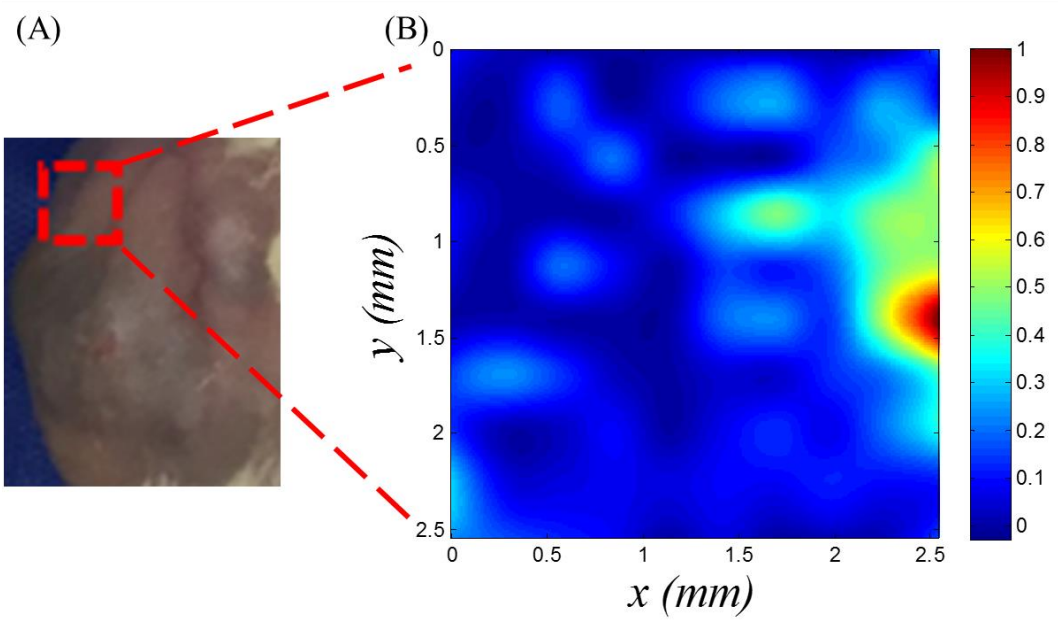

Figure 6-6 (A) and (B) show the photo of the mouse tumor and the corresponding *in vivo* USF tumor image.

After 20 mins, another USF tumor image was acquired in its adjacent area. The depth remained at the same location and the scanning area (2.54×2.54 mm^2) inside the tumor in x-y plane was moved a distance of 1.27 mm towards the body. The white-light photo and its corresponding USF image were shown in Figure 6-7(A) and (B). Comparing Figure 6-6(B) with Figure 6-7(B), we can see the difference of the contrast agent's distribution. It is reasonable because the second scanning area is closer to the injecting site so that there were more contrast agents distributed there.

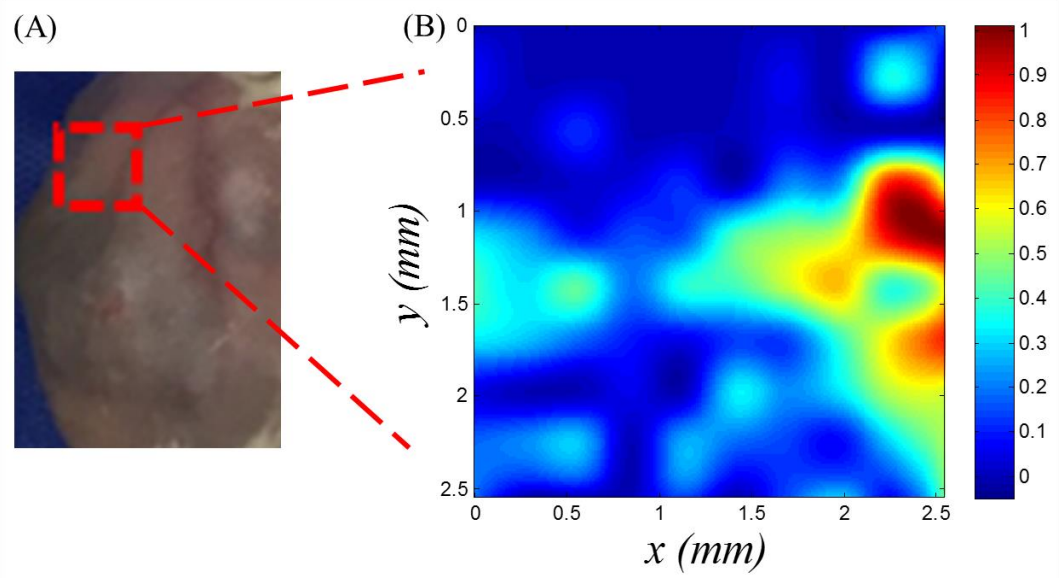

Figure 6-7 (A) The white-light photo of the mouse tumor. (B) The corresponding *in vivo* USF tumor image.

Similar experiments were conducted on other tumors in mice. Another example is shown in Figure 6-8(B). This tumor USF image was acquired after injecting the contrast agents for 40 mins. The HIFU focus was placed inside the tumor with the depth of ~0.55 cm and the scanning area is still 2.54×2.54 mm^2 in x-y plane. Some micro-information such as microstructures (different tumor lobes) can be revealed.

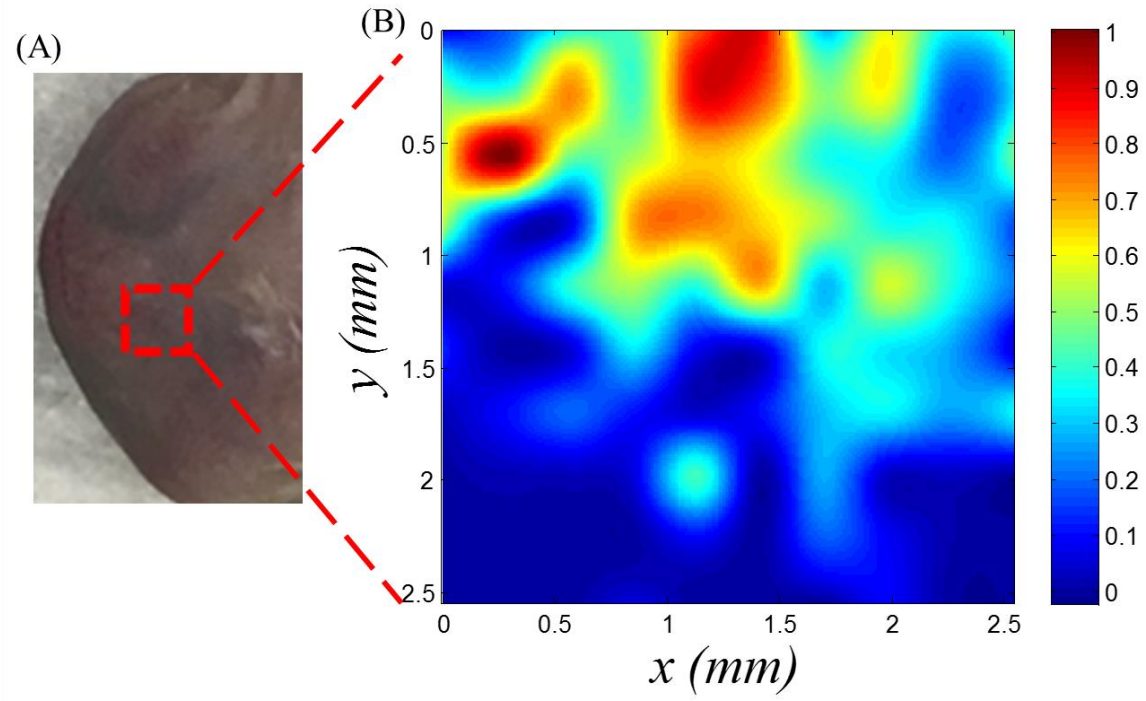

Figure 6-8 (A) shows the photo of the mouse tumor (thickness: 1.1 cm). (B) shows the corresponding *in vivo* USF tumor image.

6.3.2.2 *In vivo* tumor USF imaging by using ICG NPs

To demonstrate the feasibility of *in vivo* USF imaging using different types of contrast agents and to investigate the LCST effect on the negative USF signal, further experiments based on ICG-encapsulated P(NIPAM-AAm 90:10) NPs (LCST: 39 °C) were conducted. In order to best excite the ICG fluorophore and achieve better USF signal strength, the laser and corresponding filter setup were changed into an 808 nm diode laser and two 830 nm long-pass interference filters combined with two 830 nm long-pass absorptive glass filters.

In a similar procedure, the background fluorescence signal before and after contrast agents injection were acquired. Figure 6-9 shows that the fluorescence signal increased 16.6 folds after the ICG NPs were injected into the tumor which is similar to the result of $ADP(CA)_2$ NCs and indicates ICG NPs were successfully injected.

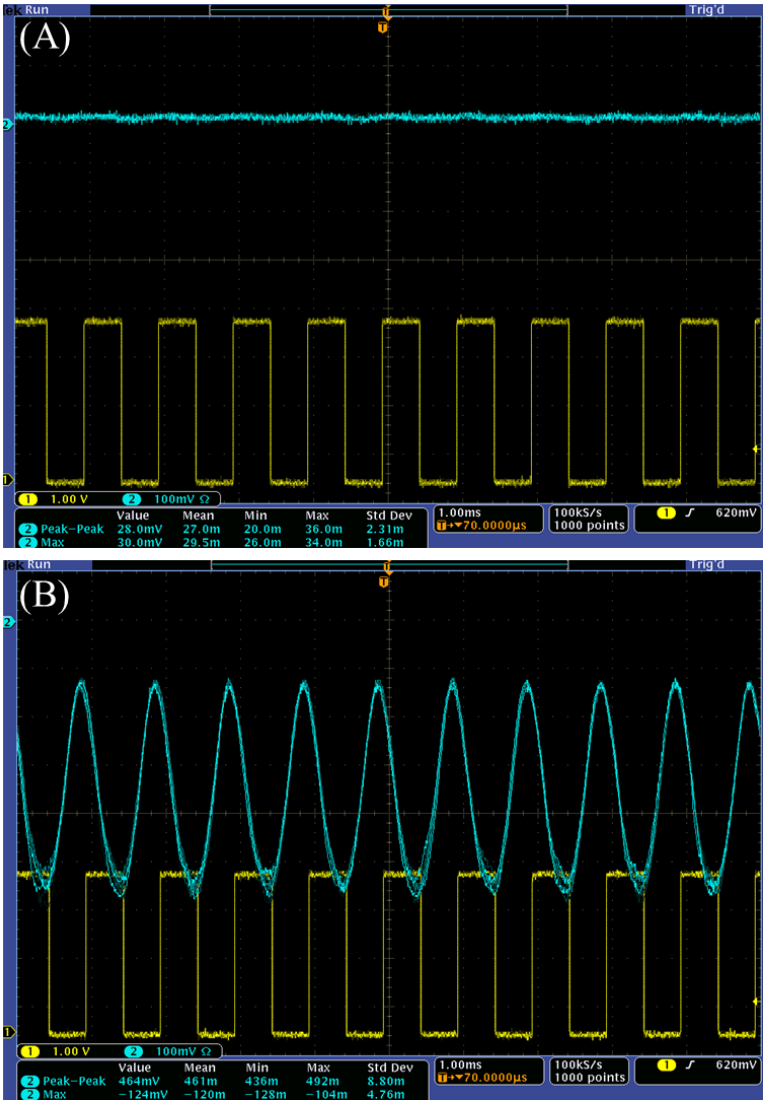

Figure 6-9 (A) The background fluorescence signal without injecting ICG-based agents. (B) The fluorescence signal after injecting 200 µL ICG-based agents.

In this study, the tumor thickness is 1 cm. The scanned x-y plane was in a depth of ~0.5 cm. The *in vivo* USF image shown in Figure 6-10 was acquired half an hour after the injection. Signals with specific USF temporal pattern were identified, which suggests that ICG NPs also work for the *in vivo* USF imaging. During the injection in this experiment, the needle was placed into the tumor with an angle. The distribution of the contrast agents presented in the USF image is matched with the injection direction very well. It's worth pointing out that the *in vivo* USF signal of ICG NPs is still negative even though the LCST is higher than the body temperature. This further confirms that the

negative USF signal is mainly caused by the interaction between the USF agents and the *in vivo* biological environment rather than the low LCST effect of $ADP(CA)_2$ NCs.

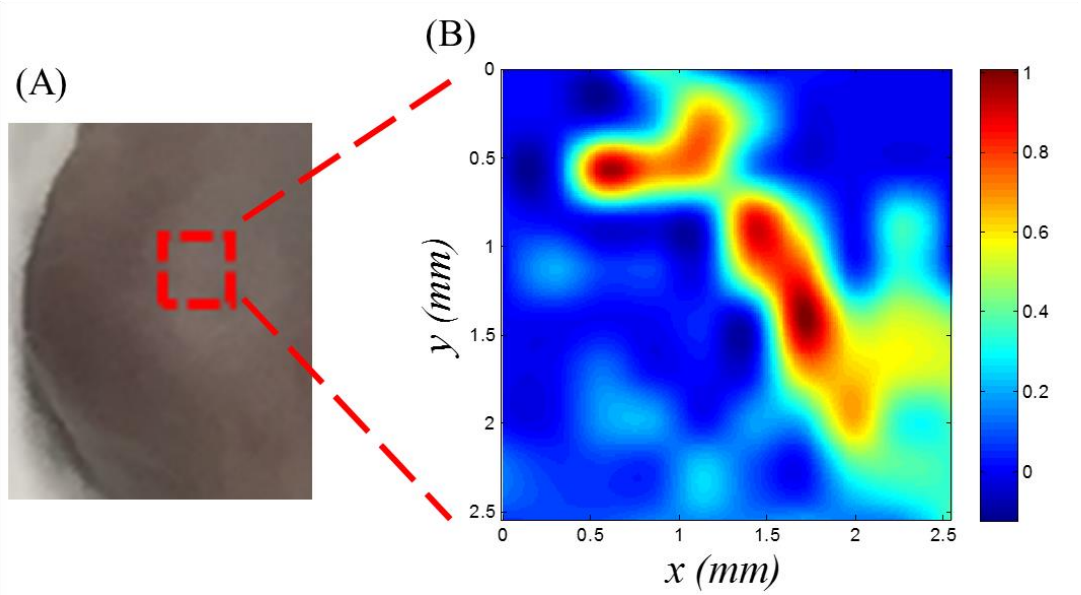

Figure 6-10 (A) The while-light photo of mouse tumor. (B) The *in vivo* USF tumor image with contrast agents of ICG NPs.

6.4 Conclusion

The feasibility of *in vivo* USF imaging was evaluated in the preliminary studies in this chapter. We achieved high-resolution and noninvasive *in vivo* USF imaging for the first time on mouse tumors. In addition, two types of contrast agents which have both low and high LCSTs have been tested in this study for *in vivo* USF imaging and both of them worked well. The results indicate the negative *in vivo* USF signal is probably due to the interaction between the USF agents and the biological environment. This work further demonstrated the capability of USF in centimeter-deep tissue high-resolution imaging and the great potential of USF for *in vivo* applications.

Chapter 7

Conclusions and Future Work

7.1 Conclusions

The significant barrier which prevents optical imaging techniques from revealing micro-information embedded in deep tissue is the light diffusion limit. Because of the strong tissue light scattering, it is extremely difficult to focus light into a tiny spot in centimeter-deep within the body. This dissertation explores the strategies and develops a fundamentally different imaging technique (USF: ultrasound-switchable fluorescence) to achieve fluorescence microscopic imaging in centimeter-deep tissue. This new imaging technique combines the advantage of ultrasound including the small tissue ultrasonic scattering and the heating effect within the ultrasound focal volume and the advantage of diffused photons which can penetrate deep with NIR wavelengths via scattering. The specific objectives were: (1) Develop basic USF contrast agents; (2) Develop excellent NIR USF contrast agents; (3) Develop a sensitive USF imaging system and an effective signal processing algorithm; (4) Validate this new imaging modality and demonstrate its capability in phantoms and *ex vivo* biological tissues; and (5) Demonstrate its *in vivo* feasibility in centimeter-deep microscopic imaging, especially for tumor. Those objectives have been accomplished in the studies presented in Chapters 2-6.

In Chapter 2, USF contrast agents were synthesized based on environment-sensitive fluorophores and thermosensitive polymers. Four commercially available polarity-sensitive fluorophores were adopted including: DBD-ED, St633, Sq660, and St700. Among several thermosensitive polymers, PNIPAM and its copolymers were selected because of its good thermal response and its adjustable LCST. We developed and tested two different structures including linear polymer chain form and nanoparticle form. To compare different contrast agents, five parameters were defined: (1) λ_{ex} and λ_{em}; (2) I_{On}/I_{Off}; (3) τ_{On}/τ_{Off}; (4) T_{th}; and (5) T_{BW}. A fluorescence intensity and lifetime measurement system was built up for characterization. The results show that the contrast agents developed in this study have blue or red wavelengths, high lifetime on-to-off ratio (1.1-7.2), acceptable intensity on-to-off ratio (1.1-4.2), narrow temperature transition bandwidth (~ 5 °C), and adjustable temperature switching threshold (26-42 °C). However, contrast agents with longer wavelength (NIR or Far red) and higher intensity on-to-off ratio are highly desired to penetrate deeper and to obtain better SNR.

In Chapter 3, excellent NIR USF contrast agents were developed by using the same principle investigated in Chapter 2, but with different fluorophores and thermosensitive polymers. Two environment-sensitive fluorophores

whose wavelengths are located in NIR range were adopted, including: $ADP(CA)_2$ (synthesized by our collaborator in University of North Texas) and ICG (commercial available). First, we tested their environment-sensitivity by varying different microenvironments and explored their switching mechanism, especially for $ADP(CA)_2$. Then we synthesized and characterized a family of contrast agents based on those fluorophores. Herein, another thermosensitive polymer (Pluronic) was taken into consideration since it is difficult to encapsulate $ADP(CA)_2$ into PNIPAM NPs because of the fluorophore's strong hydrophobicity. The results indicate $ADP(CA)_2$ is extremely sensitive to its micro-environment, including: polarity, viscosity, biological macromolecules, surfactant, and intracellular environment. The contrast agents $ADP(CA)_2$ NCs and ICG NPs have excellent switching properties, including high fluorescence on-and-off ratios (maximum: 362), narrow transition bandwidth (5-10 °C), adjustable switching threshold (23-45 °C), and excellent switching repeatability (> 6 times). With the help of those contrast agents, the fluorescence emission efficiency has been significantly improved and centimeter-deep tissue fluorescence high-resolution imaging with good SNR and sensitivity becomes achievable.

In Chapter 4, we developed a sensitive frequency-domain USF imaging system and the corresponding signal identification algorithm. We started with investigating a continuous wave imaging system which utilized a continuous laser and PMT detection. Principles and high-resolution USF images were discussed. Its resolution is unprecedented in 8-mm deep tissue (290 μm), however, its SNR and imaging depth are limited. In order to significantly increase detection sensitivity, imaging depth, and SNR, we developed a frequency-domain imaging system in which the laser was modulated at a frequency of 1 KHz and a lock-in amplifier detection method was adopted. By using this system, unique USF temporal patterns of the contrast agents were observed and investigated. The results indicate those typical USF dynamic curves are different from the background noise and are independent of signal strength. They only depend on the type of the contrast agent. Based on these findings, an effective signal processing algorithm (i.e. a correlation method) was developed and found it increased the SNR significantly and helped achieve multiplex imaging by efficiently differentiating the USF photons from background photons and differentiating one type of USF agent from another.

Chapter 5 evaluated the feasibility of FD-USF in centimeter-deep tissue microscopic imaging in tissue-mimicking phantoms and *ex vivo* biological tissues, including porcine muscle tissues and *ex vivo* mouse organs (liver and spleen). The results show that it can achieve high spatial resolution (900 μm) in three centimeter-deep tissue with high SNR (18-242) and picomole sensitivity (~3.4 picomoles). The laser and ultrasound pulse are well below the

ANSI safety thresholds. Traditional diffuse fluorescence imaging (DF) and ultrasound imaging were used to compare and validate the USF technique. The images acquired from those three imaging modalities based on the same target were compared in aspects of target shape, size, and position. The images acquired from different modalities matched well. Besides, the spatial resolution of USF was significantly improved compared with DF (~5 times). Multi-color USF imaging was also performed using different system setups (via multiple scans) or the algorithm-based differentiation method (via a single scan). The first way utilizes different excitation and emission setups so that it makes the procedure more complicated and time consuming. The second way is much easier and time efficient, in which the multi-color USF image is achieved from a single scan and different colors are differentiated by the correlation algorithm. This shows a great potential for imaging multiple targets simultaneously in the future. To demonstrate USF's capability further, it was tested in *ex vivo* mouse organs to see whether we can obtain USF signals when the contrast agents are inside the animal organs and reveal some micro-information that cannot be seen from the conventional fluorescence imaging technologies. The results demonstrated the feasibility of USF imaging in *ex vivo* mouse organs. Some blood vessels or microstructures of liver and spleen were revealed in USF images.

Chapter 6 evaluated the *in vivo* feasibility of USF. As a goal of developing a new imaging technology, it is important to test it *in vivo*. We first developed an *in vivo* USF imaging system by incorporating the previous FD-USF system with an animal sub-system, including: an anesthesia system and a physiological monitoring system. Two injection methods were adopted for *in vivo* USF imaging in living mice, including intravenous injection and local injection. Meanwhile, two different types of USF agents with low and high LCSTs were tested, including $ADP(CA)_2$-encapsulated Pluronic F-127 NCs (LCST: 23 °C) and ICG-encapsulated P(NIPAM-AAm 90:10) NPs (LCST: 39 °C). The results showed that *in vivo* USF signals was acquired in healthy mouse tissue after intravenously injecting the contrast agents of $ADP(CA)_2$ NCs. *In vivo* mammary tumor USF images were acquired using either $ADP(CA)_2$ NCs or ICG NPs via local injections. These preliminary *in vivo* studies further demonstrated the capability of USF imaging in centimeter-deep tissue with high spatial resolution and its potential for *in vivo* applications.

7.2 Limitations and Future Directions

7.2.1 Improving USF Imaging Speed

Currently, it takes ~20 minutes to acquire one high-resolution USF image. The low speed is mainly caused by the time required for heating and cooling the tissue. The imaging speed should be significantly improved.

7.2.2 Further Improving FD-USF Spatial Resolution

First, current FD-USF resolution is ~2 times worse than the lateral acoustic focal size of the HIFU transducer and ~3 times worse than the resolution of the CW USF system. The gain is the improved sensitivity, SNR, imaging depth, and low concentration of the contrast agent. The reason of this resolution loss has been discussed in Chapter 4. More studies should be conducted to investigate the possible ways to further improve the spatial resolution.

Second, if using a single-element HIFU transducer, the axial size is always a few times larger than the lateral size, which will degrade the quality of 3-D images. Adopting two 90°-crossed transducers with overlapped foci may partially solve this issue. This strategy is being investigated in our laboratory. In addition, adopting a transducer with a small f-number <1 is also helpful, because the axial focal size is proportional to the square of the f-number.

7.2.3 Exploring More USF Fluorophores for Deeper Tissue Imaging

It is highly desired to explore more USF fluorophores to cover the NIR spectrum of 750-900 nm. This will be useful for achieving even deeper tissue imaging because tissue has relatively lower absorption coefficient in this range (compared with 670-700 nm). Also, it is useful for multi-color USF imaging if more NIR USF fluorophores can be synthesized.

7.2.4 Investigation of the Mechanism of the Negative in vivo USF Signal

When injected into animal body, the contrast agents show the negative USF signal when HIFU is applied. The studies discussed in Chapter 6 indicate that the interaction between the agents and biological environment may be the main cause. Further *in vitro* and *in vivo* experiments should be done to reveal the mechanism.

7.2.5 Specific Targeting of the USF Contrast Agents

The feasibility of *in vivo* USF imaging in mice tumor has been demonstrated in Chapter 6. However, it is very preliminary and the exact structure or information the USF image represented is still unclear. If the USF agents can specifically target to either a known biological structure, one type of cells or some biomolecules, it will make USF a more powerful tool for *in vivo* applications.

Appendix A

Linear Format of USF Contrast Agent based on $ADP(CA)_2$

Besides encapsulating ADP(CA)$_2$ into a Plurnoric nanocapsule as the USF contrast agent, ADP(CA)$_2$-conjugated linear polymers were also developed as the contrast agent for USF. Based on our previous work, thermosensitive polymers were found that they could efficiently change the microenvironment for the environment-sensitive fluorophores when responding to the surrounding temperature. When the temperature is beyond LCST of the thermosensitive polymers, these polymers experience a reversible phase transition. This phase transition leads to a significant change in polarity and viscosity microenvironment. Since ADP(CA)$_2$ was found extremely sensitive to its microenvironment (especially polarity and viscosity), three different ADP(CA)$_2$-conjugated thermosensitive linear polymers were synthesized: P(NIPAM-AH 200:1)~ADP(CA)$_2$, P(NIPAM-TBAm-AH 185:15:1)~ADP(CA)$_2$, and P(NIPAM-AAm-AH 172:28:1))~ADP(CA)$_2$. The detailed protocol is similar to the one discussed in Chapter 2. The characterization of their response to temperature has been shown in Figure A-1. The results indicate these contrast agents have three different LCSTs, 28.3 ˚C, 34 ˚C and 42 ˚C. The fluorescence of these agents was in "OFF" state when the temperature is below LCST. Once the temperature is across the LCST, the fluorescence was significantly turned on. The temperature transition bandwidths were found to be 28.3~32.8 ˚C, 34~38 ˚C and 42~46 ˚C. Within these ranges the fluorescence intensity on-to-off ratios (I_{ON}/I_{OFF}) were found to be 304-fold, 318-fold and 284-fold. A summary of those contrast agents with linear format was provided in Table A-1.

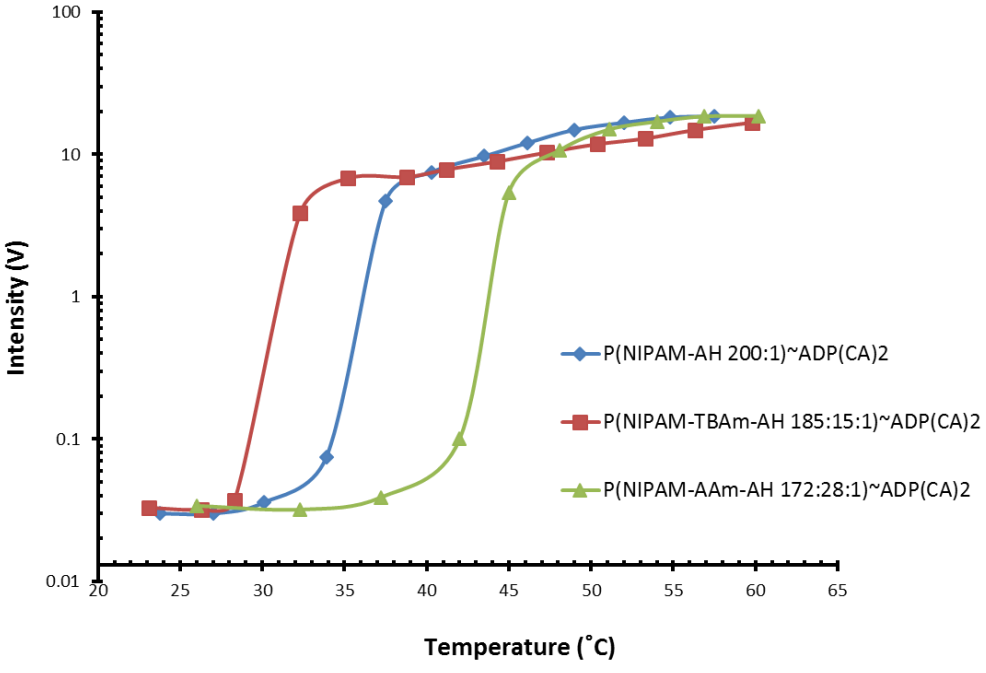

Figure A-1 Fluorescence intensity changes of $ADP(CA)_2$-conjugated linear polymers as a function of temperature. The contrast agents are P(NIPAM-AH 200:1)~$ADP(CA)_2$, P(NIPAM-TBAm-AH 185:15:1)~$ADP(CA)_2$ and P(NIPAM-AAm-AH 172:28:1))~$ADP(CA)_2$. Excitation wavelength: 655 nm. Emission filter: 711/25 band-pass filter and a neutral density filter with OD 0.9. Laser energy: 700pJ.

Table A-1 Overview of $ADP(CA)_2$-based agents with linear format

	λ_{ex}, λ_{em} (nm)	I_{On}/I_{off}	T_{th} (°C)	T_{BW} (°C)
P(NIPAM-AH 200:1)~$ADP(CA)_2$	655&711	304	34	4
P(NIPAM-TBAm-AH 185:15:1)~$ADP(CA)_2$	655&711	318	28.3	4.5
P(NIPAM-AAm-AH 172:28:1)~$ADP(CA)_2$	655&711	284	42	4

T_{th}: Temperature threshold (LCST); **T_{BW}**: transition bandwidth

Appendix B

Frequency-Domain USF Imaging System via Two Lock-in Amplifiers

The system was shown in Figure B-1. A diode laser (MDL-III-808R) was used as the excitation light source. The laser was modulated by a function generator (FG, 33220A, Agilent, Santa Clara, CA, USA) at the frequency of 1 KHz. At the same time, the same FG generated a phase-locked signal and sent it to the first LIA (SR830, Stanford Research Systems, Sunnyvale, CA, USA) as its reference signal. A band-pass filter F1 (FF01-785/62-25, Semrock, New York, USA; central wavelength: 785 nm; bandwidth: 62 nm) was used as an excitation filter to clean up any undesirable sideband components of the diode laser, which was located in the pass band of the emission filters. To maximally block the leakage of the excitation light and maintain a high fluorescence signal, two long-pass interference filters (F2 and F3; BLP01-830R-25. Semrock, New York, USA; edge wavelength: 830 nm) and two long-pass absorptive glass filters (F4 and F5; FSR-RG830, Newport, Irvine, California, USA; cut-off wavelength: 830 nm) were adopted and positioned as shown in the figure. The excitation laser and corresponding emission filter sets are changeable to best match different contrast agents' excitation and emission spectrum. Two NIR achromatic doublet lenses (AC-254-035-B, Thorlabs, New Jersey, USA) were used to collimate the fluorescence photons for best rejecting the excitation photons by the interference filters and to focus the filtered photons onto a cooled and low-noise PMT (H7422-20 driven by a high-voltage source C8137-02, Hamamatsu, Japan). The signal was further amplified by a low-noise current preamplifier (SR570, Stanford Research Systems, California, USA) and sent to the first lock-in amplifier. Then the output of the first LIA was sent into the second LIA. The output of the second lock-in amplifier was acquired by a multichannel oscilloscope (DPO4102b-l, Tektronix, Oregon, USA) and by a DAC card which was interfaced to a computer. A gated sinusoidal wave signal with a central frequency of 2.5 MHz was generated by the FG (33220A, Agilent, California, USA) and was further amplified by the RF power amplifier (325LA, E&I, New York, USA). The amplified signal was input into the MNW to drive the HIFU transducer. The HIFU transducer was focused on the target. Two PDGs (P400, Highland, California) were used to synchronize the entire system. The gating signal for HIFU which was generated from the first PDG was taken as the reference signal of the second lock-in amplifier. Both the HIFU transducer and the sample were mounted on a three-dimensional translation stage for both initial HIFU positioning and subsequent scanning. In the initial positioning, the sample was stationary and the HIFU transducer was moved to the position where the acoustic echo from the tube reached the maximum (indicating that the tube was located on the HIFU focus). This position was considered as the center of the image. A rectangular area surrounding the center was raster scanned.

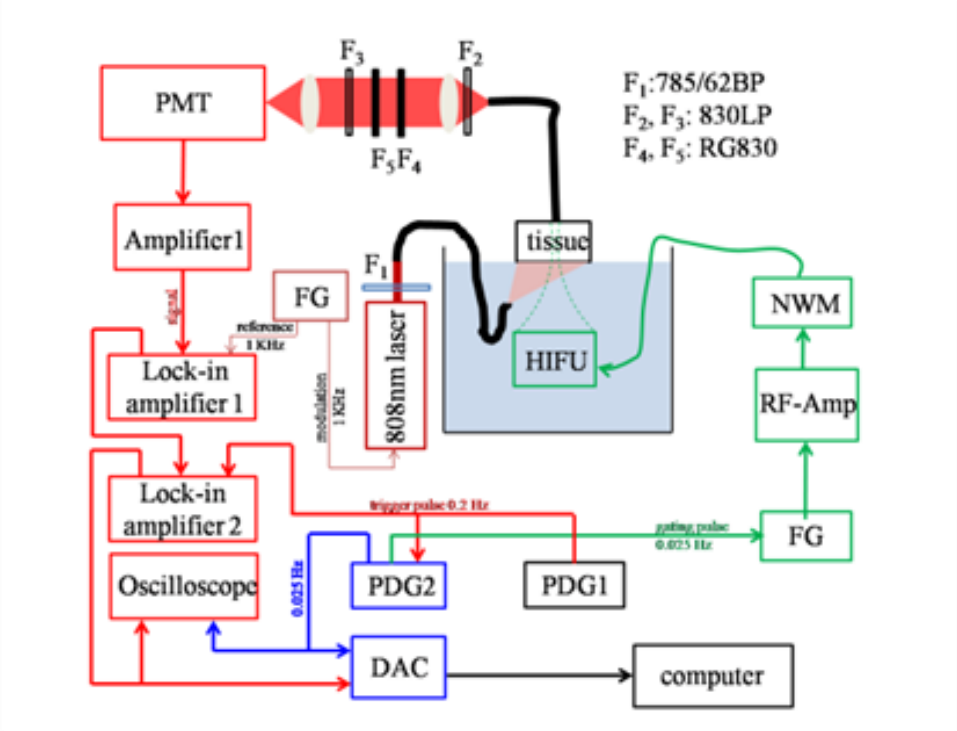

Figure B-1 A schematic diagram of the USF imaging system.

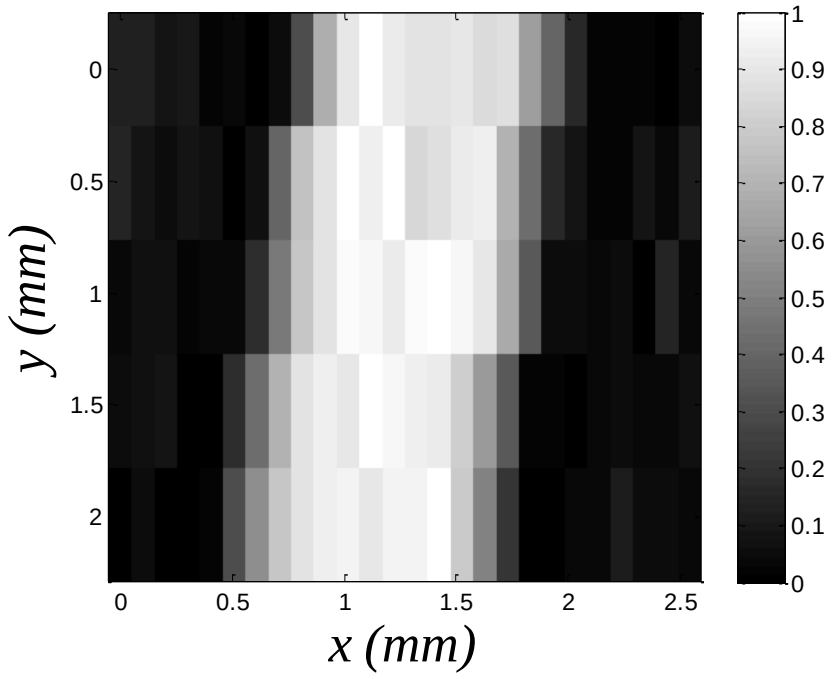

Figure B-2 The USF image of a micro-tube embedded into the porcine muscle tissue.

Figure B-2 shows the USF image of the tube embedded in tissue-mimicking silicone phantom. The thickness of the phantom is 0.8 cm and the tube size is 310 μm of I.D. and 640 μm of O.D.. In this study, the tube was filled with aqueous solution of ADP$(CA)_2$ NCs. The excitation laser and filters were adjusted accordingly to a 671 nm diode laser and three 715 nm long-pass interference filters along with two 695 nm long-pass absorptive filters. The FWHM of the USF profiles along the x direction at each y location were calculated. The averaged FWHM at different y locations were 0.93 ± 0.07 mm. The spatial resolution is similar to the frequency-domain USF imaging system by adopting one lock-in amplifier which has been described in Chapter 4. However, the temporal resolution of this system is much lower because of the imaging principle.

References

[1] R. L. Siegel, K. D. Miller, and A. Jemal, "Cancer statistics, 2016," *CA. Cancer J. Clin.*, vol. 66, no. 1, p. n/a–n/a, Dec. 2015.

[2] D. Hanahan and R. A. Weinberg, "The Hallmarks of Cancer," *Cell*, vol. 100, no. 1, pp. 57–70, Jan. 2000.

[3] L. Fass, "Imaging and cancer: A review," *Mol. Oncol.*, vol. 2, no. 2, pp. 115–152, Aug. 2008.

[4] D. Marrinucci, K. Bethel, M. Luttgen, R. H. Bruce, J. Nieva, and P. Kuhn, "Circulating tumor cells from well-differentiated lung adenocarcinoma retain cytomorphologic features of primary tumor type.," *Arch. Pathol. Lab. Med.*, vol. 133, no. 9, pp. 1468–71, Sep. 2009.

[5] G. T. Herman, "Fundamentals of Computerized Tomography: Image Reconstruction from Projections," Nov. 2009.

[6] D. J. Brenner and E. J. Hall, "Computed tomography--an increasing source of radiation exposure.," *N. Engl. J. Med.*, vol. 357, no. 22, pp. 2277–2284, 2007.

[7] K. S. Caldemeyer and K. A. Buckwalter, "The basic principles of computed tomography and magnetic resonance imaging," *J. Am. Acad. Dermatol.*, vol. 41, no. 5, pp. 768–771, 1999.

[8] D. G. Nishimura, *Principles of magnetic resonance imaging*. Stanford University, 1996.

[9] S. N. Narouze, "Atlas of ultrasound-guided procedures in interventional pain management," *Atlas Ultrasound-Guided Proced. Interv. Pain Manag.*, pp. 1–372, 2011.

[10] T. L. Szabo, *Diagnostic Ultrasound Imaging: Inside Out*. Academic Press, 2004.

[11] K. Raum and W. D. O'Brien, "Pulse-echo field distribution measurement technique for high-frequency ultrasound sources," *IEEE Trans. Ultrason. Ferroelectr. Freq. Control*, vol. 44, no. 4, pp. 810–815, Jul. 1997.

[12] W. R. Hendee and E. R. Ritenour, *Medical Imaging Physics*. John Wiley & Sons, 2003.

[13] S. I. Ziegler, "Positron emission tomography: Principles, technology, and recent developments," *Nucl. Phys. A*, vol. 752, no. 1–4 SPEC. ISS., pp. 679–687, 2005.

[14] A. Paans and A. van Waarde, "Positron emission tomography," *Methods*, vol. 27, pp. 193–194, 2002.

[15] S. Servaes, "MOLECULAR IMAGING OF PHARMACOLOGICAL MODULATION IN THE PREFRONTAL CORTEX AS A REFERENCE FOR rTMS Master in Biomedical Sciences : Neurosciences," 2013.

[16] G. D. Luker and K. E. Luker, "Optical imaging: current applications and future directions.," *J. Nucl. Med.*,

vol. 49, no. 1, pp. 1–4, Jan. 2008.

[17] W. Cai and X. Chen, “Multimodality molecular imaging of tumor angiogenesis.,” *J. Nucl. Med.*, vol. 49 Suppl 2, p. 113S–28S, Jun. 2008.

[18] J. R. Lakowicz, *Principles of Fluorescence Spectroscopy*. Springer Science & Business Media, 2007.

[19] L. V Wang, “Multiscale photoacoustic microscopy and computed tomography.,” *Nat. Photonics*, vol. 3, no. 9, pp. 503–509, Aug. 2009.

[20] R. M. Stephen and R. J. Gillies, “Promise and progress for functional and molecular imaging of response to targeted therapies.,” *Pharm. Res.*, vol. 24, no. 6, pp. 1172–85, Jun. 2007.

[21] B. M. Seddon and P. Workman, “The role of functional and molecular imaging in cancer drug discovery and development.,” *Br. J. Radiol.*, vol. 76 Spec No, pp. S128–38, Jan. 2003.

[22] M. Rudin and R. Weissleder, “Molecular imaging in drug discovery and development.,” *Nat. Rev. Drug Discov.*, vol. 2, no. 2, pp. 123–31, Feb. 2003.

[23] D. M. McDonald and P. L. Choyke, “Imaging of angiogenesis: from microscope to clinic.,” *Nat. Med.*, vol. 9, no. 6, pp. 713–25, Jun. 2003.

[24] F. Helmchen and W. Denk, “Deep tissue two-photon microscopy.,” *Nat. Methods*, vol. 2, no. 12, pp. 932–40, Dec. 2005.

[25] V. Andresen, S. Alexander, W.-M. Heupel, M. Hirschberg, R. M. Hoffman, and P. Friedl, “Infrared multiphoton microscopy: subcellular-resolved deep tissue imaging.,” *Curr. Opin. Biotechnol.*, vol. 20, no. 1, pp. 54–62, Feb. 2009.

[26] A. Corlu, R. Choe, T. Durduran, M. A. Rosen, M. Schweiger, S. R. Arridge, M. D. Schnall, and A. G. Yodh, “Three-dimensional in vivo fluorescence diffuse optical tomography of breast cancer in humans.,” *Opt. Express*, vol. 15, no. 11, pp. 6696–716, May 2007.

[27] B. Yuan and Q. Zhu, “Separately reconstructing the structural and functional parameters of a fluorescent inclusion embedded in a turbid medium.,” *Opt. Express*, vol. 14, no. 16, pp. 7172–87, Aug. 2006.

[28] J. Culver, W. Akers, and S. Achilefu, “Multimodality molecular imaging with combined optical and SPECT/PET modalities.,” *J. Nucl. Med.*, vol. 49, no. 2, pp. 169–72, Feb. 2008.

[29] K. Ferrara, R. Pollard, and M. Borden, “Ultrasound microbubble contrast agents: fundamentals and application to gene and drug delivery.,” *Annu. Rev. Biomed. Eng.*, vol. 9, pp. 415–47, Jan. 2007.

[30] L. V Wang and S. Hu, “Photoacoustic tomography: in vivo imaging from organelles to organs.,” *Science*, vol. 335, no. 6075, pp. 1458–62, Mar. 2012.

[31] B. Yuan and J. Rychak, “Tumor functional and molecular imaging utilizing ultrasound and ultrasound-mediated optical techniques.,” *Am. J. Pathol.*, vol. 182, no. 2, pp. 305–11, Feb. 2013.

[32] C. Passmann and H. Ermert, “A 100-MHz ultrasound imaging system for dermatologic and ophthalmologic diagnostics,” *IEEE Trans. Ultrason. Ferroelectr. Freq. Control*, vol. 43, no. 4, pp. 545–552, Jul. 1996.

[33] R. Gessner and P. A. Dayton, “Advances in molecular imaging with ultrasound.,” *Mol. Imaging*, vol. 9, no. 3, pp. 117–27, Jun. 2010.

[34] Q. Zhu, P. U. Hegde, A. Ricci, M. Kane, E. B. Cronin, Y. Ardeshirpour, C. Xu, A. Aguirre, S. H. Kurtzman, P. J. Deckers, and S. H. Tannenbaum, “Early-stage invasive breast cancers: potential role of optical tomography with US localization in assisting diagnosis.,” *Radiology*, vol. 256, no. 2, pp. 367–78, Aug. 2010.

[35] H. C. Ishikawa-Ankerhold, R. Ankerhold, and G. P. C. Drummen, “Advanced fluorescence microscopy techniques--FRAP, FLIP, FLAP, FRET and FLIM.,” *Molecules*, vol. 17, no. 4, pp. 4047–132, Jan. 2012.

[36] B. Yuan, S. A. Burgess, A. Iranmahboob, M. B. Bouchard, N. Lehrer, C. Bordier, and E. M. C. Hillman, “A system for high-resolution depth-resolved optical imaging of fluorescence and absorption contrast.,” *Rev. Sci. Instrum.*, vol. 80, no. 4, p. 043706, Apr. 2009.

[37] V. J. Srinivasan, H. Radhakrishnan, J. Y. Jiang, S. Barry, and A. E. Cable, “Optical coherence microscopy for deep tissue imaging of the cerebral cortex with intrinsic contrast.,” *Opt. Express*, vol. 20, no. 3, pp. 2220–39, Jan. 2012.

[38] P. Theer, M. T. Hasan, and W. Denk, “Two-photon imaging to a depth of 1000 μm in living brains by use of a Ti:Al_2O_3 regenerative amplifier,” *Opt. Lett.*, vol. 28, no. 12, p. 1022, Jun. 2003.

[39] B. Yuan, S. Uchiyama, Y. Liu, K. T. Nguyen, and G. Alexandrakis, “High-resolution imaging in a deep turbid medium based on an ultrasound-switchable fluorescence technique.,” *Appl. Phys. Lett.*, vol. 101, no. 3, p. 33703, Jul. 2012.

[40] B. Yuan, Y. Pei, and J. Kandukuri, “Breaking the acoustic diffraction limit via nonlinear effect and thermal confinement for potential deep-tissue high-resolution imaging.,” *Appl. Phys. Lett.*, vol. 102, no. 6, p. 63703, Feb. 2013.

[41] B. Yuan, “Ultrasound-modulated fluorescence based on a fluorophore-quencher-labeled microbubble

system.," *J. Biomed. Opt.*, vol. 14, no. 2, p. 024043, Jan. .

[42] K. R. Chi, "Super-resolution microscopy: breaking the limits," *Nat. Methods*, vol. 6, no. 1, pp. 15–18, Jan. 2009.

[43] S. W. Hell, "Toward fluorescence nanoscopy.," *Nat. Biotechnol.*, vol. 21, no. 11, pp. 1347–55, Nov. 2003.

[44] K. T. Takasaki, J. B. Ding, and B. L. Sabatini, "Live-cell superresolution imaging by pulsed STED two-photon excitation microscopy.," *Biophys. J.*, vol. 104, no. 4, pp. 770–7, Feb. 2013.

[45] Y. Pei, M.-Y. Wei, B. Cheng, Y. Liu, Z. Xie, K. Nguyen, and B. Yuan, "High resolution imaging beyond the acoustic diffraction limit in deep tissue via ultrasound-switchable NIR fluorescence.," *Sci. Rep.*, vol. 4, no. 1, p. 4690, 2014.

[46] B. Cheng, V. Bandi, M.-Y. Wei, Y. Pei, F. DSouza, K. T. Nguyen, Y. Hong, L. Tang, and B. Yuan, "Centimeter-deep tissue fluorescence microscopic imaging with high signal-to-noise ratio and picomole sensitivity," Oct. 2015.

[47] C. E. Schutt, M. J. Benchimol, M. J. Hsu, and S. C. Esener, "Ultrasound-modulated fluorescent contrast agent for optical imaging through turbid media," in *SPIE Optical Engineering + Applications*, 2011, p. 81650B.

[48] M. J. Benchimol, M. J. Hsu, C. E. Schutt, D. J. Hall, R. F. Mattrey, and S. C. Esener, "Phospholipid/Carbocyanine Dye-Shelled Microbubbles as Ultrasound-Modulated Fluorescent Contrast Agents.," *Soft Matter*, vol. 9, no. 8, pp. 2384–2388, Jan. 2013.

[49] Y. Liu, J. A. Feshitan, M.-Y. Wei, M. A. Borden, and B. Yuan, "Ultrasound-modulated fluorescence based on fluorescent microbubbles.," *J. Biomed. Opt.*, vol. 19, no. 8, p. 085005, Aug. 2014.

[50] B. Cheng, M. Y. Wei, Y. Liu, H. Pitta, Z. Xie, Y. Hong, K. T. Nguyen, and B. Yuan, "Development of ultrasound-switchable fluorescence imaging contrast agents based on thermosensitive polymers and nanoparticles," *IEEE J. Sel. Top. Quantum Electron.*, vol. 20, no. 3, 2014.

[51] N. Deshpande, A. Needles, and J. K. Willmann, "Molecular ultrasound imaging: current status and future directions.," *Clin. Radiol.*, vol. 65, no. 7, pp. 567–81, Jul. 2010.

[52] C. Gota, S. Uchiyama, T. Yoshihara, S. Tobita, and T. Ohwada, "Temperature-dependent fluorescence lifetime of a fluorescent polymeric thermometer, poly(N-isopropylacrylamide), labeled by polarity and hydrogen bonding sensitive 4-sulfamoyl-7-aminobenzofurazan.," *J. Phys. Chem. B*, vol. 112, no. 10, pp. 2829–36, Mar. 2008.

[53] R. M. K. Ramanan, P. Chellamuthu, L. Tang, and K. T. Nguyen, “Development of a temperature-sensitive composite hydrogel for drug delivery applications.,” *Biotechnol. Prog.*, vol. 22, no. 1, pp. 118–25, Jan. .

[54] M. Rahimi, S. Kilaru, G. E. H. Sleiman, A. Saleh, D. Rudkevich, and K. Nguyen, “Synthesis and Characterization of Thermo-Sensitive Nanoparticles for Drug Delivery Applications.,” *J. Biomed. Nanotechnol.*, vol. 4, no. 4, pp. 482–490, Dec. 2008.

[55] L. V Wang, “Ultrasound-mediated biophotonic imaging: a review of acousto-optical tomography and photo-acoustic tomography.,” *Dis. Markers*, vol. 19, no. 2–3, pp. 123–38, Jan. .

[56] *Photoacoustic Imaging and Spectroscopy*. CRC Press, 2009.

[57] D. Razansky, M. Distel, C. Vinegoni, R. Ma, N. Perrimon, R. W. Köster, and V. Ntziachristos, “Multispectral opto-acoustic tomography of deep-seated fluorescent proteins in vivo,” *Nat. Photonics*, vol. 3, no. 7, pp. 412–417, Jun. 2009.

[58] B. Yuan, Y. Liu, P. M. Mehl, and J. Vignola, “Microbubble-enhanced ultrasound-modulated fluorescence in a turbid medium,” *Appl. Phys. Lett.*, vol. 95, no. 18, p. 181113, Nov. 2009.

[59] M. Kobayashi, T. Mizumoto, Y. Shibuya, M. Enomoto, and M. Takeda, “Fluorescence tomography in turbid media based on acousto-optic modulation imaging,” *Appl. Phys. Lett.*, vol. 89, no. 18, p. 181102, Oct. 2006.

[60] Y. Lin, L. Bolisay, M. Ghijsen, T. C. Kwong, and G. Gulsen, “Temperature-modulated fluorescence tomography in a turbid media.,” *Appl. Phys. Lett.*, vol. 100, no. 7, pp. 73702–737024, Feb. 2012.

[61] Y. Lin, T. C. Kwong, L. Bolisay, and G. Gulsen, “Temperature-modulated fluorescence tomography based on both concentration and lifetime contrast.,” *J. Biomed. Opt.*, vol. 17, no. 5, p. 056007, May 2012.

[62] V. K. Garripelli, J.-K. Kim, R. Namgung, W. J. Kim, M. A. Repka, and S. Jo, “A novel thermosensitive polymer with pH-dependent degradation for drug delivery.,” *Acta Biomater.*, vol. 6, no. 2, pp. 477–85, Feb. 2010.

[63] Y. . Kirsh, N. . Yanul, and K. . Kalninsh, “Structural transformations and water associate interactions in poly-N-vinylcaprolactam–water system,” *Eur. Polym. J.*, vol. 35, no. 2, pp. 305–316, Feb. 1999.

[64] S. Uchiyama, Y. Matsumura, A. P. de Silva, and K. Iwai, “Modulation of the sensitive temperature range of fluorescent molecular thermometers based on thermoresponsive polymers.,” *Anal. Chem.*, vol. 76, no. 6, pp. 1793–8, Mar. 2004.

[65] Y. Okada and F. Tanaka, “Cooperative Hydration, Chain Collapse, and Flat LCST Behavior in Aqueous Poly(

N -isopropylacrylamide) Solutions," *Macromolecules*, vol. 38, no. 10, pp. 4465–4471, May 2005.

[66] T. Terai and T. Nagano, "Fluorescent probes for bioimaging applications.," *Curr. Opin. Chem. Biol.*, vol. 12, no. 5, pp. 515–21, Oct. 2008.

[67] H. Kobayashi, M. Ogawa, R. Alford, P. L. Choyke, and Y. Urano, "New strategies for fluorescent probe design in medical diagnostic imaging.," *Chem. Rev.*, vol. 110, no. 5, pp. 2620–40, May 2010.

[68] M. A. Haidekker and E. A. Theodorakis, "Environment-sensitive behavior of fluorescent molecular rotors.," *J. Biol. Eng.*, vol. 4, p. 11, Jan. 2010.

[69] R. Weissleder and V. Ntziachristos, "Shedding light onto live molecular targets.," *Nat. Med.*, vol. 9, no. 1, pp. 123–8, Jan. 2003.

[70] C. Reichardt, "Solvatochromic Dyes as Solvent Polarity Indicators," *Chem. Rev.*, vol. 94, no. 8, pp. 2319–2358, Dec. 1994.

[71] M. Y. Berezin, H. Lee, W. Akers, and S. Achilefu, "Near infrared dyes as lifetime solvatochromic probes for micropolarity measurements of biological systems.," *Biophys. J.*, vol. 93, no. 8, pp. 2892–9, Oct. 2007.

[72] G. S. Loving, M. Sainlos, and B. Imperiali, "Monitoring protein interactions and dynamics with solvatochromic fluorophores.," *Trends Biotechnol.*, vol. 28, no. 2, pp. 73–83, Feb. 2010.

[73] M. Baruah, W. Qin, C. Flors, J. Hofkens, R. A. L. Vallée, D. Beljonne, M. Van der Auweraer, W. M. De Borggraeve, and N. Boens, "Solvent and pH dependent fluorescent properties of a dimethylaminostyryl borondipyrromethene dye in solution.," *J. Phys. Chem. A*, vol. 110, no. 18, pp. 5998–6009, May 2006.

[74] A. Loudet and K. Burgess, "BODIPY dyes and their derivatives: syntheses and spectroscopic properties.," *Chem. Rev.*, vol. 107, no. 11, pp. 4891–932, Nov. 2007.

[75] H. Sunahara, Y. Urano, H. Kojima, and T. Nagano, "Design and Synthesis of a Library of BODIPY-Based Environmental Polarity Sensors Utilizing Photoinduced Electron-Transfer-Controlled Fluorescence ON/OFF Switching," *J. Am. Chem. Soc.*, vol. 129, no. 17, pp. 5597–5604, May 2007.

[76] D. Wang, R. Miyamoto, Y. Shiraishi, and T. Hirai, "BODIPY-conjugated thermoresponsive copolymer as a fluorescent thermometer based on polymer microviscosity.," *Langmuir*, vol. 25, no. 22, pp. 13176–82, Nov. 2009.

[77] J. B. Segur and H. E. Oberstar, "Viscosity of Glycerol and Its Aqueous Solutions," *Ind. Eng. Chem.*, vol. 43, no. 9, pp. 2117–2120, Sep. 1951.

[78] X.-X. Zhang, Z. Wang, X. Yue, Y. Ma, D. O. Kiesewetter, and X. Chen, “pH-sensitive fluorescent dyes: are they really pH-sensitive in cells?,” *Mol. Pharm.*, vol. 10, no. 5, pp. 1910–7, May 2013.

[79] A. Rodríguez, M. Muñoz, M. del Mar Graciani, S. Fernández Chacón, and M. L. Moyá, “Kinetic study in water-ethylene glycol cationic, zwitterionic, nonionic, and anionic micellar solutions.,” *Langmuir*, vol. 20, no. 23, pp. 9945–52, Nov. 2004.

[80] M. K. Kuimova, S. W. Botchway, A. W. Parker, M. Balaz, H. A. Collins, H. L. Anderson, K. Suhling, and P. R. Ogilby, “Imaging intracellular viscosity of a single cell during photoinduced cell death.,” *Nat. Chem.*, vol. 1, no. 1, pp. 69–73, Apr. 2009.

[81] R. D. Moriarty, A. Martin, K. Adamson, E. O’Reilly, P. Mollard, R. J. Forster, and T. E. Keyes, “The application of water soluble, mega-Stokes-shifted BODIPY fluorophores to cell and tissue imaging.,” *J. Microsc.*, vol. 253, no. 3, pp. 204–18, Mar. 2014.

[82] A. J. Gomes, L. O. Lunardi, J. M. Marchetti, C. N. Lunardi, and A. C. Tedesco, “Indocyanine green nanoparticles useful for photomedicine.,” *Photomed. Laser Surg.*, vol. 24, no. 4, pp. 514–21, Aug. 2006.

[83] Y. Chen and X. Li, “Near-infrared fluorescent nanocapsules with reversible response to thermal/pH modulation for optical imaging.,” *Biomacromolecules*, vol. 12, no. 12, pp. 4367–72, Dec. 2011.

[84] G. Hong, S. Diao, J. Chang, A. L. Antaris, C. Chen, B. Zhang, S. Zhao, D. N. Atochin, P. L. Huang, K. I. Andreasson, C. J. Kuo, and H. Dai, “Through-skull fluorescence imaging of the brain in a new near-infrared window,” *Nat. Photonics*, vol. 8, no. 9, pp. 723–730, Aug. 2014.

[85] K. Si, R. Fiolka, and M. Cui, “Fluorescence imaging beyond the ballistic regime by ultrasound pulse guided digital phase conjugation.,” *Nat. Photonics*, vol. 6, no. 10, pp. 657–661, Oct. 2012.

[86] K. Si, R. Fiolka, and M. Cui, “Breaking the spatial resolution barrier via iterative sound-light interaction in deep tissue microscopy.,” *Sci. Rep.*, vol. 2, p. 748, Jan. 2012.

[87] Y. M. Wang, B. Judkewitz, C. A. Dimarzio, and C. Yang, “Deep-tissue focal fluorescence imaging with digitally time-reversed ultrasound-encoded light.,” *Nat. Commun.*, vol. 3, p. 928, Jan. 2012.

[88] P. Lai, Y. Suzuki, X. Xu, and L. V Wang, “Focused fluorescence excitation with time-reversed ultrasonically encoded light and imaging in thick scattering media.,” *Laser Phys. Lett.*, vol. 10, no. 7, p. 75604, Jan. 2013.

[89] B. Judkewitz, Y. M. Wang, R. Horstmeyer, A. Mathy, and C. Yang, “Speckle-scale focusing in the diffusive regime with time-reversal of variance-encoded light (TROVE).,” *Nat. Photonics*, vol. 7, no. 4, pp. 300–305,

Apr. 2013.

[90] R. Horstmeyer, H. Ruan, and C. Yang, “Guidestar-assisted wavefront-shaping methods for focusing light into biological tissue,” *Nat. Photonics*, vol. 9, no. 9, pp. 563–571, Aug. 2015.

[91] N. T. Huynh, B. R. Hayes-Gill, F. Zhang, and S. P. Morgan, “Ultrasound modulated imaging of luminescence generated within a scattering medium.,” *J. Biomed. Opt.*, vol. 18, no. 2, p. 20505, Feb. 2013.

[92] X. Xu, H. Liu, and L. V. Wang, “Time-reversed ultrasonically encoded optical focusing into scattering media,” *Nat. Photonics*, vol. 5, no. 3, pp. 154–157, Jan. 2011.

[93] G. Marriott, S. Mao, T. Sakata, J. Ran, D. K. Jackson, C. Petchprayoon, T. J. Gomez, E. Warp, O. Tulyathan, H. L. Aaron, E. Y. Isacoff, and Y. Yan, “Optical lock-in detection imaging microscopy for contrast-enhanced imaging in living cells.,” *Proc. Natl. Acad. Sci. U. S. A.*, vol. 105, no. 46, pp. 17789–94, Nov. 2008.

[94] F. Ayers, A. Grant, D. Kuo, D. J. Cuccia, and A. J. Durkin, “Fabrication and characterization of silicone-based tissue phantoms with tunable optical properties in the visible and near infrared domain,” in *Biomedical Optics (BiOS) 2008*, 2008, pp. 687007–687007–9.

[95] H. Xu and B. W. Rice, “In-vivo fluorescence imaging with a multivariate curve resolution spectral unmixing technique.,” *J. Biomed. Opt.*, vol. 14, no. 6, p. 064011, Jan. .

[96] J. Shah, S. Park, S. Aglyamov, T. Larson, L. Ma, K. Sokolov, K. Johnston, T. Milner, and S. Y. Emelianov, “Photoacoustic imaging and temperature measurement for photothermal cancer therapy.,” *J. Biomed. Opt.*, vol. 13, no. 3, p. 034024, Jan. .

[97] A. C. Dupont, E. E. Sauerbrei, P. V Fenton, P. C. Shragge, G. E. Loeb, and F. J. Richmond, “Real-time sonography to estimate muscle thickness: comparison with MRI and CT.,” *J. Clin. Ultrasound*, vol. 29, no. 4, pp. 230–6, May 2001.

[98] W. M. White, I. R. S. Makin, M. H. Slayton, P. G. Barthe, and R. Gliklich, “Selective transcutaneous delivery of energy to porcine soft tissues using Intense Ultrasound (IUS).,” *Lasers Surg. Med.*, vol. 40, no. 2, pp. 67–75, Feb. 2008.

[99] J. L. Sandell and T. C. Zhu, “A review of in-vivo optical properties of human tissues and its impact on PDT.,” *J. Biophotonics*, vol. 4, no. 11–12, pp. 773–87, Nov. 2011.

[100] S. Grabtchak, L. G. Montgomery, and W. M. Whelan, “Optical absorption and scattering properties of bulk porcine muscle phantoms from interstitial radiance measurements in 650-900 nm range.,” *Phys. Med. Biol.*,

vol. 59, no. 10, pp. 2431–44, May 2014.

[101] C. M. C. Tempany, “Advances in Biomedical Imaging,” *JAMA*, vol. 285, no. 5, p. 562, Feb. 2001.

Biographical Information

Bingbing Cheng received his Bachelor of Science degree in Biomedical Engineering from Beijing Jiaotong Univerity, Beijing, China, in 2011. He worked as a research assistant in Ubiquitous Network and Digital Media Processing Lab with Prof. Weibin Zhu, Beijing Jiaotong University, from 2008 to 2009, where he focused on speech recognition and natural language processing. In 2010, he joined Prof. Xiaoming Ding's group in Modern Signal Processing and Information Authentication Lab, Beijing Jiaotong University, and worked on digital image processing, embedded system, and biometric identification technology. His major project "Passenger Real-time Train Ticket Check-in System and its Realization based on Biometrics of Palm Vein" won the first prize in National Undergraduate Electronic Design Contest, China, in 2010. From 2010 to 2012, he worked as a research assistant in Prof. Yao Zhao's Computer Vision and Digital Media Lab, Beijing Jiaotong University, and focused on 3D video encoding and sparse representation.

After that, he continued his graduate studies in U.S. and received his Ph.D. degree in Biomedical Engineering at the Joint Program of University of Texas at Arlington and University of Texas Southwestern Medical Center in 2016. His research interest is to explore and develop new imaging techniques, including contrast agents and instruments, for the purpose of understanding cancer mechanisms, early detecting and diagnosing cancers, and monitoring cancer treatment efficiency. During his Ph.D. career, he worked with Prof. Baohong Yuan and developed a fundamentally different imaging modality: ultrasound-switchable fluorescence (USF), including contrast agents and imaging systems, which opens the door for future studies of centimeter-deep tissue fluorescence microscopic imaging. The experience in developing USF contrast agents makes him an expert in biomaterials, especially in nanoparticles. His expertise also includes medical imaging instrumentation, ultrasound and optical imaging, and signal processing. He has co-authored 10 journal papers, presented more than 15 conference papers, and filed one US patent. Based on his achievements in scientific research, he was awarded Alfred and Janet Potvin Award in 2015 and Carrizo Dissertation Research Scholarship in 2016. In the future, he is willing to keep contributing in this field to develop more innovative medical technologies to push the current healthcare modalities to the next stage and further bring the human's quality of life into a higher level.